Carbon Materials Upcycling and Applications for Energy Storage and Decarbonization

---

A Dissertation

Presented to the Faculty

of the School of Engineering and Applied Science

University of Virginia

---

in Partial Fulfillment

of the Requirements for the Degree

of Doctor of Philosophy in **Mechanical & Aerospace Engineering**

By

Yucheng Zhou

December 2023

APPROVAL SHEET

The dissertation is submitted in partial fulfillment of the
requirements for the degree of
Doctor of Philosophy

Yucheng Zhou, Author

This dissertation has been read and approved by the examining Committee:

Xiaodong (Chris) Li, Advisor

Baoxing Xu, Committee Chair

Sarah Sun, Committee Member

David L. Green, Committee Member

Sen Zhang, Committee Member

Accepted for the School of Engineering and Applied Science:

Jennifer L. West, Dean

School of Engineering and Applied Science
December 2023

Abstract

Expanding energy crises and environmental issues are attracting attention. Efficient and effective energy storage systems and decarbonization strategies are urgently demanded. For energy storage, Li-ion batteries are dominating the market, however, they are reaching their theoretical limits and are usually not considered green energy storage systems. On the other hand, traditional decarbonization strategies are struggling to address the current challenge of more severe carbon emissions. Studying and developing green, sustainable next-generation energy storage and decarbonization technologies are necessary. Upcycling waste from human activity into advanced materials for energy storage and decarbonization is able to not only ease the energy issues but also help with carbon neutrality, which is considered a promising route to overcoming the challenges. Among all recyclable materials, carbon materials have attracted intensive attention as they are abundant and readily upcycled into high value-added carbon materials. Although the high-end materials, especially biomass carbon polymer and carbon nanomaterials, are not yet commercially viable in the market, it is predicted that they may hold the key to a new era of high-capacity energy storage and high-efficiency decarbonization. This dissertation aims to convert carbon-based waste into high value-added carbon materials via green, sustainable methods, find applications in energy storage and decarbonization, and study the conversion and function mechanisms. In this dissertation, paper waste and end-of-life Li-ion battery anodes were chosen to be the waste feedstocks to prepare advanced carbon materials for energy storage and decarbonization.

Specifically, in Chapter 2, cellulose fibers were extracted from paper waste through a simple process and coated onto commercial separators in Li-S batteries to improve their performance. The performance of the batteries with or without cellulose fibers was tested and the working mechanisms of the cellulose fibers were experimentally explored. The Li-S batteries with cellulose fibers exhibited a longer lifespan and better stability than the batteries without cellulose fibers. In Chapter 3, a more thorough mechanism study of the cellulose fibers was conducted using computational tools. Battery working conditions were set up in molecular dynamics simulations, which showed that the cellulose fiber was capable of blocking more polysulfides and randomizing more Li-ions. Functional groups

on the cellulose fibers were built in density functional theory models, which revealed that the groups could repel polysulfides and attract and redirect Li-ions. In Chapter 4, the possibility of employing the cellulose fibers as an adsorber of CO_2 was explored using computational methods. Compared with one of the most commonly seen CO_2 adsorbers, activated carbon, cellulose fibers were predicted to possess much better CO_2/N_2 selectivity while remaining comparable capacity. In Chapter 5, Li-ion battery anodes were recycled by an innovative approach to maximizing the capability of being exfoliated into graphene afterward. In sequence, carbon nanotubes (CNTs) were greenly and seamlessly grown on the upcycled graphene, and the obtained hybrid carbon material was exploited as a sulfur substrate to assemble Li-S batteries. Thanks to the large space for sulfur loading and volume expansion as well as excellent electrical conductivity, the battery with the graphene/CNT hybrid achieved much better longevity and stability compared with the battery using commercial graphite.

The findings bring new insights into deriving valuable and sustainable carbon materials from low-cost and environmentally friendly sources to enrich energy storage and decarbonization, paving the way towards a waste-to-wealth, circular society.

Table of Contents

Abstract i

Table of Contents iii

Acknowledgements v

List of Figures vi

List of Tables xiii

Chapter 1. Introduction 1

1.1 Background and Motivation 1

1.2 Sustainable Carbon Materials 3

1.3 Current Recycling and Upcycling Methods of Carbon Materials 4

1.3.1 Upcycling Carbon Materials from Biomass Waste 4

1.3.2 Upcycling Carbon Materials from Spent Batteries 6

1.4 Applications of Upcycled Carbon Materials 6

1.4.1 Energy Storage 6

1.4.2 Decarbonization 8

1.5 Specific Research Objectives 9

Reference 11

Chapter 2. Recycled Cellulose Fibers from Paper Waste for Energy Storage 18

2.1 Introduction 18

2.2 Methods 20

2.3 Results and Discussion 22

2.3.1 Characterization of CF-coated separator 22

2.3.2 Electrochemical performance of CF-enabled batteries 25

2.3.3 Analyses of impedance and polarization 31

2.3.4 Sulfur distribution in batteries 34

2.3.5 Post-failure analysis of cycled batteries 35

2.4 Conclusions 39

Reference 39

Chapter 3. Mechanism Study of Recycled Cellulose Fibers in Li-S Batteries 47

3.1 Introduction 47

3.2 Methods 48

3.3 Results and Discussion 50
3.3.1 Li-ion redistribution simulation 50
3.3.2 Polysulfide MD simulation 53
3.3.3 Mechanism discussion 57
3.4 Conclusions 63
Reference 64
Chapter 4. Use of Recycled Cellulose Fibers for Carbon Dioxide Adsorption 68
4.1 Introduction 68
4.2 Methods 70
4.3 Results and Discussion 71
4.3.1 CO_2 adsorption performance under different conditions 71
4.3.2 Gas selectivity performance 76
4.4 Conclusions 77
Reference 78
Chapter 5. Upcycled CNT/graphene Hybrid from End-of-life Batteries for Energy Storage 81
5.1 Introduction 81
5.2 Methods 83
5.3 Results and Discussion 86
5.3.1 Upcycling anode graphite into graphene 86
5.3.2 Greenly growing CNTs on graphene 88
5.3.3 Electrochemical characterization and discussion 94
5.4 Conclusions 103
Reference 104
Chapter 6. Summary and Future Work 111
6.1 Summary of Contribution and Significance 111
6.2 Recommendations for Future Research 113

Acknowledgements

Firstly, I would like to express my sincere gratitude to my advisor, Professor Xiaodong (Chris) Li, for patiently advising me through the years of my Ph.D. study, for always supporting me in pursuing all the scientific ideas, and for encouraging me to overcome all the obstacles in front of me. His enthusiasm for work and wisdom in life always push me to aim high and achieve more, which will benefit my career and life in the future. Without his constant supervision and guidance, I would not be able to finish this dissertation.

Secondly, I would like to thank my committee members, Prof. Baoxing Xu, Prof. David L. Green, Prof. Sen Zhang, and Prof. Sarah Sun, for their insightful opinions and guidance in my dissertation. I also want to thank them for always being patient with me, willing to adjust their schedules for my dissertation, and for their valuable time helping me.

Thirdly, I would like to thank all my colleagues, Jiajun, Ruoxi, Tyler, Zhijing, *et al.*, and former colleagues, Zan, Ningning, Yunya, Jiadeng, Clifton, Victor, *et al.*, for the welcoming and supportive atmosphere and their help through my Ph.D. study. I would also like to thank all my friends at UVa, Yuan, Tianhui, Chaobo, *et al.*, for their company and help, which makes my Ph.D. life so colorful.

Fourthly, I would like to acknowledge the financial support from the National Science Foundation and the department to make this dissertation possible.

Lastly, I would like to thank my parents for raising me, caring for me, and supporting me so I can always give my hundred percent to pursue my dream.

List of Figures

Figure 1.1. (a) Energy consumption in the U.S. from different resources [1]. (b) Battery distribution in current battery market [2].

Figure 1.2. Strategies for using biomass to produce graphene.

Figure 1.3. Strategies of CNT synthesis from biomass-based carbon sources.

Figure 2.1. Schematic of the CF-coated separator repelling polysulfide-ions and redistributing Li-ions.

Figure 2.2. Experimental details of preparing CF-coated separators.

Figure 2.3. (a) SEM image of a paper hardboard. The inset shows the optical image of the hardboard. (b) CF suspension in ethanol. (c) SEM image of the CF-coated separator. The inset shows the optical image of the CF-coated separator. (d) SEM image of the CF coating cross section. (e) EDS map of carbon. (f) EDS map of oxygen. (g) XRD spectra of the hardboard and CF coating. (h) C1s spectrum on the CF coating. (i) O1s spectrum on the CF coating. (j) Surface overall XPS spectrum of the CF coating. (k) N1s spectrum on the CF coating.

Figure 2.4. (a) Typical charge/discharge cycle of the CF-enabled battery. (b) Typical charge/discharge cycle of the non-CF battery. (c) CV curve of the CF-enabled battery. (d) CV curve of the non-CF battery. (e) EIS curve of the CF-enabled battery. The insets show the EIS curve of the battery before cycling and equivalent circuit of the EIS data. (f) EIS curve of the non-CF battery. The insets show the EIS curve of the battery before cycling and equivalent circuit of the EIS data. (g) Rate performance of the CF-enabled battery and non-CF battery. (h) EIS regression lines of the batteries with only electrolyte and a CF-coated separator or an uncoated separator.

Figure 2.5. (a) Overall cyclic performance of the CF-enabled battery with the areal cathode mass of 5.15 mg cm^{-2} and non-CF battery with the areal cathode mass of 5.38 mg cm^{-2}. (b) Polarization voltage of the CF-enabled battery and non-CF battery.

Figure 2.6. EIS curve fitting data for the non-CF battery at the (a) 0^{th} cycle, (b) 5^{th} cycle,

(c) 50th cycle, (d) 200th cycle, and the CF-enabled battery at the (e) 0th cycle, (f) 5th cycle, (g) 50th cycle, (h) 200th cycle.

Figure 2.7. (a) Graphical constitute of a Li-S battery. (b) Sulfur contents on different surfaces after cycling 10 times. (c) SEM image of the APC/S cathode surface in the CF-enabled battery after cycling 10 times. (d) SEM image of the APC/S cathode surface in the non-CF battery after cycling 10 times. (e) SEM image of the Li anode surface in the CF-enabled battery after cycling 10 times. (f) SEM image of the Li anode surface in the non-CF battery after cycling 10 times.

Figure 2.8. (a) SEM image of the Li anode cross section in the end-of-life CF-enabled battery. (b) SEM image of the Li anode cross section in the end-of-life non-CF battery. (c) SEM image of the Li anode surface in the end-of-life CF-enabled battery. The inset shows the optical image of the Li anode surface in the end-of-life CF-enabled battery. (d) SEM image of the Li anode surface in the end-of-life non-CF battery. The inset shows the optical image of the Li anode surface in the end-of-life non-CF battery.

Figure 2.9. (a) SEM image of the separator surface facing the anode in the end-of-life CF-enabled battery. (b) SEM image of the separator facing the anode in the end-of-life non-CF battery. (c) SEM image of the separator surface facing the cathode in the CF-enabled battery. (d) SEM image of the separator surface facing the cathode in the non-CF battery.

Figure 2.10. EDS maps of Li metal anode in (a) CF-enabled battery and (b) non-CF battery.

Figure 3.1. (a) SEM image of the Li anode edge in CF-enabled battery after 100 cycles. (b) SEM image of the Li anode edge in non-CF battery after 100 cycles. (c) MD model for Li-ion traveling simulation using cellulose chains. (d) MD result of Li-ion traveling simulation using cellulose chains. (e) MD result of Li-ion traveling simulation using PP chains. (f) DFT result of interactions between a cellulose chain and a Li ion.

Figure 3.2. (a) MD model for Li-ion traveling simulation using PP chains. (b) Neighbor map for the MD result of the PP model. (c) Neighbor map for the MD result of the CF model. (d) MD model for Li-ion traveling simulation using both CF and PP chains. (e) MD

result of Li-ion traveling simulation using both CF and PP chains. (f) DFT result of interactions between a PP chain and a Li ion.

Figure 3.3. (a) EDS image of the Li anode in the CF-enabled battery. (b) MD model for CF chains with polysulfides. (c) EDS image of the Li anode in the non-CF battery. (d) MD model for PP chains with polysulfides. (e) Velocity changes of different polysulfide species before arriving the CF or PP chains. (f) MD net models of the CF and PP with pores in the middle. (g) Initial status of the MD simulation for polysulfides traveling through the CF net fence. (h) Final status of the MD simulation for polysulfides traveling through the CF net fence. (i) Initial status of the MD simulation for polysulfides traveling through the PP net fence. (j) Final status of the MD simulation for polysulfides traveling through the PP net fence. (k) Normalized calculation result for the effectiveness of CF and PP.

Figure 3.4. (a) Initial status of the MD simulation for twelve polysulfides traveling through the CF net fence. (b) Final status of the MD simulation for twelve polysulfides traveling through the CF net fence. (c) Initial status of the MD simulation for twelve polysulfides traveling through the PP net fence. (d) Final status of the MD simulation for twelve polysulfides traveling through the PP net fence.

Figure 3.5. (a) DFT simulation of the carboxylic group on S_8^{2-} polysulfides. (b) DFT simulation of the phenolic group on S_8^{2-} polysulfides. (c) DFT simulation of the carboxylic group on S_6^{2-} polysulfides. (d) DFT simulation of the phenolic group on S_6^{2-} polysulfides. (e) Permeation experiment between the uncoated separator and CF-coated separator after 5 minutes, 10 minutes, 15 minutes, 20 minutes, 30 minutes, 40 minutes, 50 minutes, and 60 minutes.

Figure 3.6. Charge map of the CF after the electric field.

Figure 3.7. (a) MD simulation result for CF losing H^+ under electric field. (b) DFT simulation results of the interactions between HCFs and $Li2S_n$ ($n \leq 2$). (c) DFT simulation results of the interactions between OCFs and $Li2S_n$ ($n \leq 2$). (d) DFT simulation results of the interactions between HCFs and S_n^{2-} ($n \geq 4$). (e) DFT simulation results of the

interactions between OCFs and S_n^{2-} ($n \geq 4$). (f) Energy difference from DFT simulations of CFs (or PP) and polysulfides (or Li).

Figure 3.8. (a) MD simulation result for PP under electric field. (b) DFT simulation results of the interactions between PP and $Li2S_n$ ($n \leq 2$). (c) DFT simulation results of the interactions between PP and S_n^{2-} ($n \geq 4$).

Figure 4.1. Schematic of cellulose fibers from paper waste achieving CO_2 adsorption with high CO_2/N_2 selectivity.

Figure 4.2. (a) CF and AC tube models for all the computational studies. (b) MD simulation box setup for CFs' velocity and temperature simulations, and the result with the CO_2 velocity of 0.015 Ang/fs and at 300 K. (c) MD simulation box setup for AC's velocity and temperature simulations, and the result with the CO2 velocity of 0.015 Ang/fs and at 300 K. (d) CO_2 adsorption ratios of CFs and AC with the CO_2 velocities ranging from 0.009 Ang/fs to 0.023 Ang/fs at 300 K. (e) CO_2 adsorption behavior of CFs with a velocity of CO_2 flow from 0.009 Ang/fs to 0.023 Ang/fs. (f) CO_2 adsorption behavior of AC with a velocity of CO_2 flow from 0.009 Ang/fs to 0.023 Ang/fs.

Figure 4.3. (a) CO_2 adsorption behavior of CFs with system temperatures from 240 K to 340 K. (b) CO_2 adsorption behavior of AC with system temperatures from 240 K to 340 K. (c) CO_2 adsorption ratios of CFs and AC with the CO_2 velocity of 0.015 Ang/fs at temperatures ranging from 240 K to 340 K. (d) Interaction distances for each CO_2 approaching CF and AC.

Figure 4.4. (a) MD simulation box setup for CFs' CO_2 selectivity in a gas mixture of N_2 (two-atom molecules in yellow), O_2 (two-atom molecules in red), and CO_2 (three-atom molecules). (b) Result of CF gas adsorption in the gas mixture. (c) MD simulation box setup for AC's CO_2 selectivity in the gas mixture. (d) Result of AC gas adsorption in the gas mixture. (e) Adsorption ratios of N_2, O_2, and CO_2 in CFs. (f) Adsorption ratios of N_2, O_2, and CO_2 in AC. (g) Concentration changes of N_2, O_2, and CO_2 before and after the adsorption simulation using CFs and AC.

Figure 5.1. Schematic for upcycling end-of-life Li-ion battery anode graphite into graphene and growing CNTs on graphene to construct Li-S batteries.

Figure 5.2. TEM image of upcycled graphene. (a) Low-resolution TEM image of a graphene sheet. (b) High-resolution TEM image of the circled area in (a). (c) Low-resolution TEM image of another graphene sheet.

Figure 5.3. Characterization and modeling of upcycling graphite into graphene. (a) SEM image of recycled graphite (inset: optical image of recycled graphite) before purification. (b) SEM image of recycled graphite (inset: optical image of recycled graphite) after purification. (c) Low-resolution TEM image of an upcycled graphene sheet (inset: corresponding graphene dispersed in DI water). (d) XRD spectra of recycled graphite and upcycled graphene. (e) Carbon EDS map of recycled graphite after purification. (f) High-resolution TEM image of an upcycled graphene sheet (inset: corresponding FFT image). (g) DFT calculated H^+-induced spacing expansion. (h) DFT calculated OH^--induced spacing expansion.

Figure 5.4. XRD pattern of the CNT/graphene material.

Figure 5.5. EDS maps of CNT buds on yeast/graphene. (a) SEM image of the CNT buds. (b) Carbon map of the CNT buds. (c) Potassium map of the CNT buds. (d) Oxygen map of the CNT buds. (e) Phosphorus map of the CNT buds.

Figure 5.6. Characterization and modeling of growing CNTs on graphene. (a) SEM image of the CNT/graphene hybrid nanostructures (inset: CNT/graphene hybrid powders). (b) High-resolution SEM image of the CNT/graphene hybrid nanostructures. (c) TEM image of the as-obtained CNTs. (d) TEM image of the CNTs on graphene sheets. (e) High-resolution TEM image of the CNTs on graphene sheets (inset: high-resolution TEM image of the joint between the CNT and graphene). (f) Point elemental detections of a CNT. (g) MD simulations showing CNT growth on graphene with P as the catalyst. (h) Number of different carbon rings of the simulated outer CNT wall layer from the MD simulations and experimentally measured carbon rings from a randomly chosen area of a CNT wall.

Figure 5.7. MD simulations of CNT growth with double-layer graphene as substrate and phosphorus as catalyst (Green: phosphorus, red: original carbon, blue: inserted carbon). (a) Initial model. (b) Model with 200 carbon atoms inserted. (c) Model with 400 carbon atoms inserted. (d) Model with 600 carbon atoms inserted. (e) Model with 800 carbon atoms inserted. (f) Model with 1000 carbon atoms inserted. (g) Model with 1200 carbon atoms inserted. (h) Model with 1400 carbon atoms inserted.

Figure 5.8. Different types of carbon rings on a randomly chosen area of a CNT wall. (a) Inverse FFT image of a defective CNT wall (inset: FFT image). (b) Highlighted inverse FFT image of different carbon rings (Blue: C-pentagon, red: C-hexagon, green: C-heptagon).

Figure 5.9. CV and EIS curves of reference batteries. (a) CV curves of the commercial graphite battery at the 0^{th}, 5^{th}, 50^{th}, and 200^{th} cycles. (b) CV curves of the recycled graphite battery at the 0^{th}, 5^{th}, 50^{th}, and 200^{th} cycles. (c) CV curves of the upcycled graphene battery at the 0^{th}, 5^{th}, 50^{th}, and 200^{th} cycles. (d) EIS plot of the commercial graphite battery at the 0^{th}, 5^{th}, 50^{th}, and 200^{th} cycles. (e) EIS plot of the recycled graphite battery at the 0^{th}, 5^{th}, 50^{th}, and 200^{th} cycles. (f) EIS plot of the upcycled graphene battery at the 0^{th}, 5^{th}, 50^{th}, and 200^{th} cycles.

Figure 5.10. Curve fitting patterns of the EIS data of the batteries at the 5^{th}, 50^{th}, and 200^{th} cycles. Red: the commercial graphite battery; Green: the recycled graphite battery; Yellow: the upcycled graphene battery; Blue: the CNT/graphene battery.

Figure 5.11. EDS maps of all cathodes. (a) EDS map of the sulfur-infiltrated commercial graphite cathode. (b) EDS map of the sulfur-infiltrated recycled graphite cathode. (c) EDS map of the sulfur-infiltrated upcycled graphene cathode. (d) EDS map of the sulfur-infiltrated CNT/graphene cathode.

Figure 5.12. Characterization of battery performance. (a) Charge/discharge cycle of the CNT/graphene battery. (b) CV curves of the CNT/graphene battery. (c) EIS patterns of the CNT/graphene battery (inset: equivalent circuit of the patterns). (d) Rate performances of

the CNT/graphene battery and the reference batteries. (e) Cycling performance of the CNT/graphene battery.

Figure 5.13. (a) Discharge cycling performances and Coulombic efficiencies of the batteries studied. (b) Polarization potential of the CNT/graphene battery and the commercial graphite battery.

List of Tables

Table 2.1. Comparison among recent work with polymer-based coatings on pp separators.

Table 2.2. Curve fitting data of the EIS test.

Table 5.1. Element contents after each purification step.

Table 5.2. Direct carbon emission estimation of synthesizing CNT/graphene with different techniques.

Table 5.3. Curve fit data of EIS tests.

Table 5.4. Battery performance of CNT/graphene batteries using different methods and graphene types.

Chapter 1. Introduction

1.1 Background and Motivation

Energy crises and environmental issues have been considered two of the most crucial topics nowadays. As of now, fossil fuels are still the most common power supplies worldwide, which, as non-renewable resources, not only intensify the ongoing shortage of energy resources but also severely pollute the environment, releasing a large amount of greenhouse gas (GHG). **Figure 1.1**a shows the energy consumption in the U.S. from different resources until 2021 [1]. Using renewable resources, such as wind and biofuels, to replace fossil fuels is necessary for a sustainable future. However, one of the limits of using renewable resources to generate power is their unstable power output, which requires efficient and effective energy storage systems to be viable.

Meanwhile, the rapid development of electric vehicles (EVs) and portable electronics is also pushing the energy storage market to the next generation. Among all energy storage devices, Li-ion battery is dominating the market, as shown in **Figure 1.1**b [2]. With the expanding market and maturing research, the Li-ion battery is reaching its limit of energy density. In addition, the non-eco-friendly nature of Li-ion batteries also cannot meet the sustainable goal of current society. Discovering and studying more advanced, environmentally friendly, high-energy batteries have become an unstoppable trend in energy storage development.

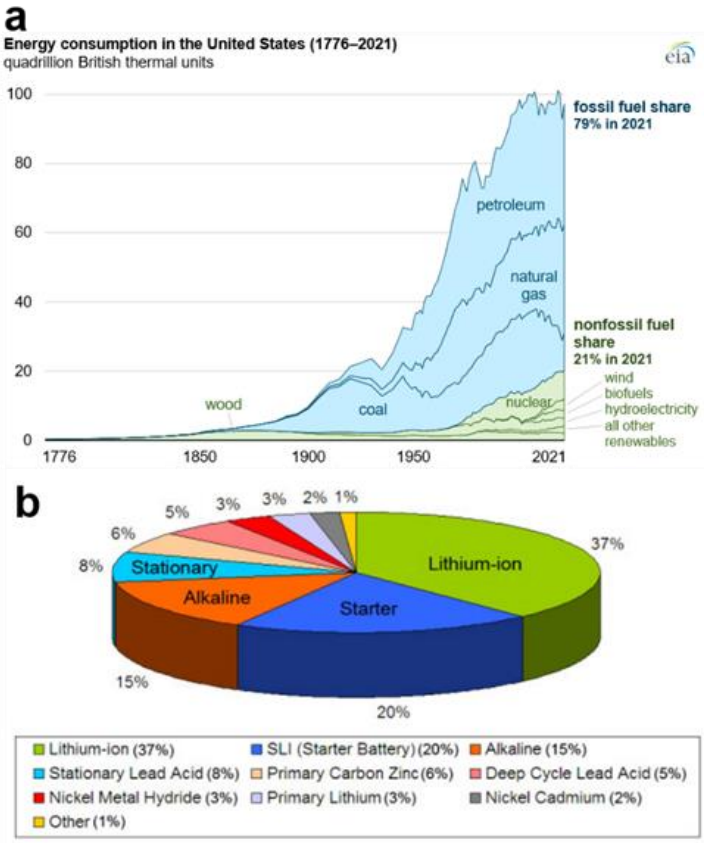

Figure 1.1. (a) Energy consumption in the U.S. from different resources [1]. (b) Battery distribution in current battery market [2].

Another challenge that comes with the flourishing energy storage market is the limited supply of raw materials. Carbon materials, such as graphite and biomass carbon, as one of the most commonly used raw materials in batteries are usually derived from nonrenewable and high-cost resources under relatively harsh conditions [3,4]. Besides, high value-added carbon materials with large potential to improve current batteries, such as graphene and carbon nanotubes (CNTs), have yet been commercially viable completely [4]. Despite being used in energy storage, carbon materials also have a large potential to be used in decarbonization. Therefore, different carbon material sources, which are cost-effective, eco-friendly, and sustainable, are urgently demanded in batteries or decarbonization. On the other hand, the increasing need for batteries leads to the challenging disposal of end-of-life batteries. Without proper management, the pollutant and toxic materials within the batteries can severely influence the environment, such as the underground water and soil. Moreover, valuable, recyclable materials and rare metals, including Co, Ni, and graphite,

will be wasted. Searching for low-cost and green recycling or even upcycling routes for batteries plays a more and more important role in achieving a waste-to-wealth, sustainable society.

To address the as-mentioned challenges, in my Ph.D. research, I focused on investigating recycling processes of used or end-of-life sources and upcycling them into high value-added carbon materials to build different components to be used in batteries or decarbonization applications. The following scientific questions were studied: (1) What carbon materials can be efficiently and cost-effectively recycled and upcycled from used sources? (2) What are the potential applications of these carbon materials in energy storage and/or decarbonization? (3) What are the fundamental mechanisms behind the carbon materials working in energy storage and/or decarbonization?

1.2 Sustainable Carbon Materials

Carbon, as one of the most abundant elements on earth, has been widely investigated in material development especially over the last several decades [5,6]. Is it well-known for its stability, versatility, and functionality and has been recognized for its importance and potential by some highest scientific awards including the 1996 Nobel Prize in Chemistry (fullerenes), the 2008 Kavli Prize in Nanoscience (CNTs), and the 2010 Nobel Prize in Physics (graphene). The interest in studying them has never dropped since then because of the discovery of carbon nanomaterials.

The most important carbon nanomaterial, graphene, has exhibited incredible performance in energy fields [7]. Graphene has found applications in energy generation and storage owing to its outstanding properties, such as high specific surface area, electrical conductivity, thermal conductivity, and mechanical strength [8-11]. For instance, graphene has been found to improve water splitting and hydrogen storage [12]. Although considerable efforts have been made to produce graphene, its production rate remains low [13,14]. Chemical vapor deposition (CVD) is often used to synthesize graphene [15]. However, this method is costly and not sustainable since it uses non-renewable fossil fuels as carbon sources. Another route for graphene fabrication is to exfoliate graphene from mined graphite [16,17]. However, mined graphite is also non-renewable, and its exploitation often causes severe environmental issues [18]. Synthetic graphite from coal tar has also been used for graphene fabrication [19]. Nevertheless, producing graphene

from synthetic graphite consumes fossil fuels with high carbon emissions. Therefore, seeking new carbon source materials is imperative in achieving sustainable manufacturing of graphene. To meet this goal, recycling and upcycling waste carbon sources into graphene are more than welcome to complete the puzzle of sustainable graphene production.

On the other hand, carbon-based polymers, especially natural polymers, always have a role to play in the carbon material family [20]. Cellulose fiber is one of the most commonly seen natural polymers, and as a gift of nature, the research of cellulose fibers (CFs) can be traced back to over 160 years ago [21]. It exists in almost all kinds of biomass such as plants and bacteria and has been successfully extracted for various applications such as energy storage and additives for composites [22,23]. However, the functions of the CFs highly depend on their microstructures, which differ in different biomass and via distinct production methods, inducing difficulties in finding uniform and stable CF sources [24]. As of now, extracting CFs from non-repeating biomass sources and identifying their functions have often been exploited. Due to unnatural processing, biomass-based artificial products, such as paper, with high-quality CFs have also been widely studied as another type of CF source. These products are usually abandoned with intact CFs still available, therefore, they are worth recycling and even upcycling.

1.3 Current Recycling and Upcycling Methods of Carbon Materials

1.3.1 Upcycling Carbon Materials from Biomass Waste

Current studies have reported many successful conversions from biomass materials into carbon nanomaterials including graphene and CNTs [25,26]. For deriving graphene, biomass materials are first dehydrated and then crystallized at a high temperature. Various methods, such as chemical activation, thermal pre-treatment, and atom doping, are employed to modify the starting biomass materials. When biomass is employed as the starting material to derive graphene, exfoliation is often required following carbonization and graphitization to produce single or few-layer graphene (**Figure 1.2**). Several methods, such as the Hummers method and shear mixing, have been explored to exfoliate graphitized biomass into graphene [27,28].

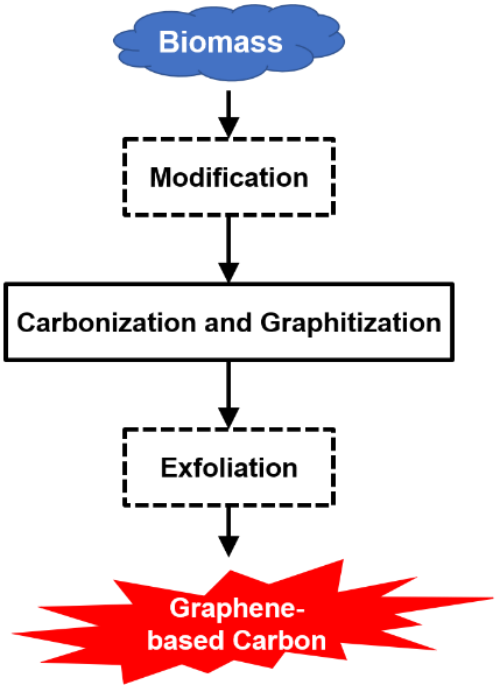

Figure 1.2. Strategies for using biomass to produce graphene.

For CNT manufacturing, methods are more systematic as listed in **Figure 1.3**. Energy consumption must be considered in deriving CNTs from biomass. Pyrolyzing biomass to CNTs recently dramatically reduced CNT processing time from more than 16 hours down to less than 3 hours, consuming much less energy [29-44]. The newly developed microwave-aided pyrolysis employs much lower temperature and shorter time, further reducing energy consumption [45]. Although pyrolysis and conventional CVD have similar synthesis temperatures and time, CVD often requires two chambers of different temperatures, which consumes much more energy. One chamber spray pyrolysis-assisted CVD can further shorten the processing time down to less than 30 minutes [46-50].70,71,97-99 Mechanochemical treatment often requires 36-hour ball-milling to achieve high CNT yields, which consumes energy. However, compared with conventional CNT growth methods (arc discharge, laser ablation, etc.), the above-mentioned biomass CNT deriving methods consume less energy since they do not demand extremely high temperatures [51].

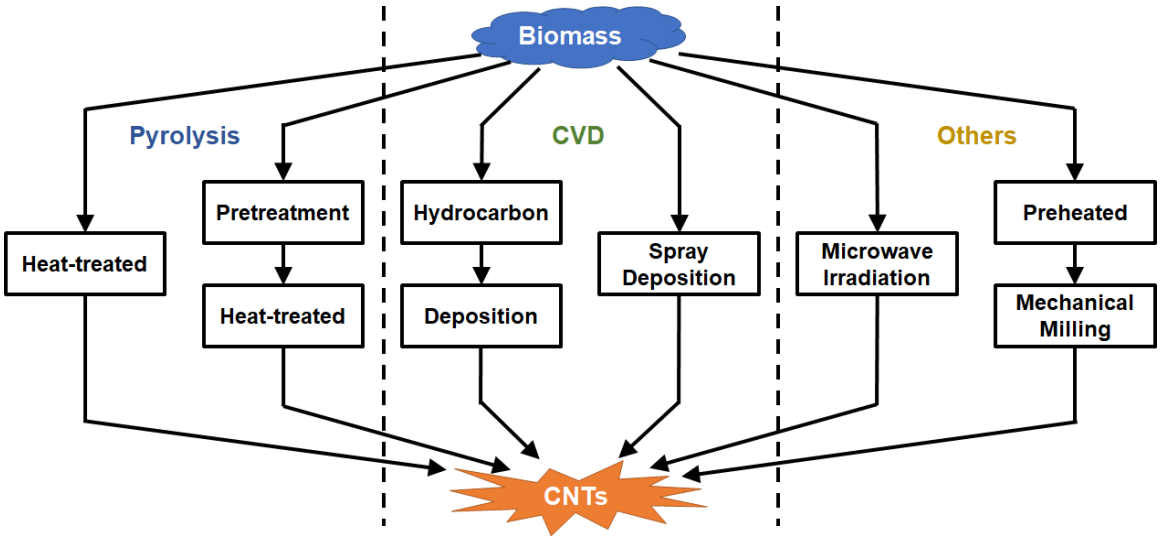

Figure 1.3. Strategies of CNT synthesis from biomass-based carbon sources.

CF extraction from biomass is much simpler as many biomasses originally possess a large number of CFs. They can be attained in nano or micro forms by chemical or mechanical methods. The three major steps in CF extraction are pre-hydrolysis, pulping, and bleaching [52]. Pre-hydrolysis treatment uses mineral acids or alkali to open up the matrix. Pulping process cooks the fiber with the help of alkali. The last step bleaching is used to extract the pure form of CFs usually with H_2O_2, sodium chlorite, or ozone.

1.3.2 Upcycling Carbon Materials from Spent Batteries

The content of carbon materials in spent batteries usually only counts graphite, therefore, how to effectively and efficiently recycle graphite and upcycle it into other high value-added materials requires thorough investigation. Based on the final products, the recycling process for graphite anode varies to a degree. Generally, for all processes, the first step is to separate the graphite anode from other components in the spent batteries [53]. This can be achieved either by a series of physical separations such as sieving, grinding, peeling, and floating, or by a chemical separation using acids and alkali. After separation, acid leaching or washing can be used to remove most impurities, however, it is often a challenge to completely eliminate impurities, such as stubborn aluminum and binders. Therefore, a thermal treatment is usually introduced following the previous step to further get rid of impurities and restore graphite structure to be reused in various applications.

1.4 Applications of Upcycled Carbon Materials

1.4.1 Energy Storage

Rapidly increased demand for electric vehicles and portable electronic devices stimulates the development of electrochemical energy storage devices [54,55]. Recently, graphene and CNTs with large specific surface area and high electrical conductivity have found applications in supercapacitors and batteries [55-57]. Electrochemistry, including energy storage and electrocatalysis, is seeing ever-increasing demand for low-cost and sustainable biomass-derived graphene and CNTs. For energy storage, specific capacity, energy density, lifespan, and mass loading of active materials are often jointly considered to evaluate the products.

Specific surface area is critical to promote ion adsorption space in supercapacitor electrodes. Biomass-derived graphene has shown its path in the energy storage field. For example, spruce bark-derived graphene possessed a specific surface area of 2385 m^2 g^{-1} [58]. The coin-type two-electrode systems constructed with such graphene nanosheet arrays exhibited an outstanding capacity of 275 F g^{-1} at 1 A g^{-1} with a 98.3% retention rate after running 10,000 times at 5 A g^{-1}, indicating exceptional electrochemical stability and reversibility of the biomass-derived graphene. The high specific surface area of the biomass-derived graphene achieved a mass loading of the active materials of ~3.64 mg cm^{-2} and a high energy density of 10.6 Wh kg^{-1} at a power density of 50 W kg^{-1}. Obviously, the mass loading of active materials in supercapacitors and Li-S batteries was far below the commercial level of 10 mg cm^{-2} and 5 mg cm^{-2}, impeding the commercialization of biomass-derived graphene and CNTs in energy storage [59,60]. As reported, biomass-derived graphene/CNT-based electrodes contained many non-conductive activated carbon byproducts from biomass decomposition. Therefore, in order to avoid exacerbating the poor conductivity of electrodes, most supercapacitors and Li-S batteries with biomass-derived graphene/CNT were constructed with low mass loading. Biomass-derived graphene/CNT electrodes have demonstrated promise in cost reduction, ascribed to the use of cost-effective biomass.

Besides biomass-derived graphene and CNT being used in energy storage, graphite from end-of-life batteries being restored to battery grade and reused in energy storage has recently attracted tremendous attention. The graphite from spent batteries usually has only a small number of defects. Heat treatment in which the temperature is sufficiently high can repair the defects by reconnecting carbon atoms, shortening the gap between layers, and

removing impurities [61]. With proper temperature, the graphite can even return to a battery grade, which can close the loop of battery recycling for its second life. The recycled graphite can also be upcycled into high-quality graphene for next-generation energy storage. Natarajan *et al.* [62] reported a graphene sheet-enabled supercapacitor that achieved a high energy density of 31.9 Wh kg^{-1} with a long cycle life.

In addition to the upcycled carbon nanomaterials, recycled CFs can also be used in energy storage. Yang *et al.* [63] synthesized a free-standing film from amorphous red phosphorous and pyrolyzed bacterial cellulose via thermal carbonization, in sequence with the vaporization-condensation process. The film exhibited a high reversible capacity of 1039.7 mA h g^{-1} after 100 cycles at 0.1C and excellent cycling stability. Zhang *et al.* [64] reported a recycled paper/graphene oxide hybrid to be activated to build Li-S batteries, rendering a superior lifespan of 620 cycles with an excellent capacity retention rate of 60.5%.

1.4.2 Decarbonization

Reducing carbon emissions and greenhouse gases has been becoming one of the most discussed topics. Carbon materials may hold the key to accomplishing this goal. Carbon materials recycling and upcycling from biomass and battery waste already meet this goal to some degree and the products can also be used in this field to further reach carbon neutrality.

Using graphite from spent batteries as CO_2 adsorbent is overlooked. As the graphite from batteries is usually enriched with impurities that can be treated as active sites for gas capturing, recycled graphite, especially raw graphite, has a large potential to be used for CO_2 absorption. Lee *et al.* [65] employed carbon residues from spent Li-ion batteries to impregnate with K_2CO_3 as a CO_2 adsorbent and achieved a 5.1-7.3 wt% CO_2 adsorption capacity, where both chemical absorption and physical adsorption behaviors were observed. Compared with graphite from spent batteries, graphene or graphene-like materials from biomass have more been investigated in the CO_2 adsorption field as graphene is easier to modify and functionalize and has a much larger specific surface area to attract CO_2. Parshetti *et al.* [66] produced porous graphene-like nanosheets from lignocellulosic fiber of oil palm empty fruit bunches by a thermal graphitization, which attained a 2.43 mmol g^{-1} maximum CO_2 uptake at 25 °C and 1 bar with an excellent CO_2/N_2 selectivity.

In addition, CFs from biomass have a long history of being used as CO_2 adsorbents due to their naturally porous structure, large surface area, and enriched surface functional groups. Recently, a cellulose nanofibril film derived from corn husks and oat hulls was reported to show good CO_2 adsorption potential [67]. The amine group on the surface tends to chemically react with CO_2 to provide better CO_2 uptake, which was measured to be up to 2.11 mmol g^{-1}.

1.5. Specific Research Objectives

In this dissertation, carbon-based wastes, paper hardboard and end-of-life Li-ion battery anodes, were recycled and upcycled to prepare different advanced carbon materials and used in energy storage systems or decarbonization applications. Based on the different recycled sources and applications, the research thrusts are centered at the following four aspects: (1) recycled cellulose fibers (CFs) from paper waste for energy storage; (2) mechanism study of recycled CFs in Li-S batteries; (3) use of recycled CFs for carbon dioxide adsorption; (4) upcycled CNT/graphene hybrid from end-of-life batteries for energy storage.

Objective 1: Recycled cellulose fibers from paper waste for energy storage

CF as a type of natural polymer has received extensive attention due to its abundance and wide applications in daily supplies, such as newspapers and paper containers. However, it has rarely been recycled for advanced applications. The abundant functional groups on the CF render it the potential to overcome the current challenges of Li-S batteries. In this thrust, purified CFs were upcycled from paper waste to be coated on commercial separators within Li-S batteries. Specifically, paper waste was first soaked in diluted NaOH solution and stirred at a temperature of 80 °C to remove binders and other impurities. The purified CFs were isolated and washed by centrifugation using DI water and isopropyl alcohol. The CF suspension was eventually kept in the isopropyl alcohol before being coated on commercial separators using simple vacuum filtration. After drying, the CF-coated separators were used to assemble Li-S batteries. The batteries used typical Li metal anodes and sulfur-loaded APC cathodes with either CF-coated separators or ordinary commercial separators in order to observe the functions of CFs.

Objective 2: Mechanism study of recycled cellulose fibers in Li-S batteries

The commercial viability of the current Li-S battery is hindered by two major

challenges, polysulfide shuttle effect and dendritic/mossy Li growth. After experimentally proving the effectiveness of CFs in diminishing both challenges of the Li-S battery, it is critical to learn the mechanism behind the phenomenon. Since the entire operation happens within assembled batteries, simulations play a more efficient role in thoroughly investigating the functions of CFs. In this thrust, multiple simulation techniques were applied including the density functional theory (DFT) calculation and the molecular dynamic (MD) simulation. The model of CFs was designed using the DFT calculation and afterwards, the model was applied to MD simulation boxes. In addition, DFT calculations were used to unveil the behaviors and energy differences of various polysulfide species and Li-ions when encountering CF-coated separators. Meanwhile, MD simulations were used to mimic realistic battery conditions during operation and separately study the functions of CFs towards polysulfides and Li-ions.

Objective 3: Use of recycled cellulose fibers for carbon dioxide adsorption

With the development of technologies and the explosive consumption of fossil fuels, GHGs have inevitably become one of the central topics of environmental science. Thanks to the functional groups on CFs, they may hold the key to suppressing the expansion of GHG concerns, especially CO_2. Purified CFs can be derived from the previous proposed research. It is worth studying the potential of CFs towards CO_2 adsorptions. In this thrust, MD simulation tools were applied to explore the possibility of CO_2 adsorption using CF models compared with activated carbon (AC) models. Multiple factors that influence the effectiveness were investigated, such as temperature and pressure. The cause and the mechanism of CF and AC adsorbing CO_2 were also studied with the goal to provide guidelines for future experimental research.

Objective 4: Upcycled CNT/graphene hybrid from end-of-life batteries for energy storage

The disposal of end-of-life Li-ion batteries not only causes severe pollution to the environment but also throws away critical materials. Therefore, it is vital to recycle end-of-life batteries to meet decarbonization goals and to ensure good stewardship of critical materials. Graphite is commonly used as the anode material in Li-ion batteries and can be upcycled into graphene. However, graphene alone in Li-S batteries cannot encapsulate sulfur to increase sulfur loading and buffer volume expansion. In this thrust, a novel, cost-

effective, and efficient route to recycling graphite from end-of-life battery and upcycling it into graphene was designed. Thereafter, an all-green strategy for growing CNTs on graphene was established and the product was loaded with sulfur for constructing Li-S batteries. The anode graphite was collected from disassembled end-of-life batteries and purified using acid and alkaline solutions with different diluted levels before shear-mixed into graphene. The graphene was fully mixed with yeast followed by a simple heat treatment to grow CNTs seamlessly. The CNT/graphene hybrid material was loaded with sulfur and assembled as the cathode for the use in the Li-S battery.

Reference

[1] O. Comstock, Fossil fuel sources accounted for 79% of U.S. consumption of primary energy in 2021, U.S. Energy Information Administration, *Monthly Energy Review*, 2022. Link: https://www.eia.gov/todayinenergy/detail.php?id=52959

[2] Bobby, The Global Battery Market – an Industry Report Review, *BATTERY BASICS*, 2014. Link: https://www.upsbatterycenter.com/blog/global-battery-market-industry-report-review/

[3] Y. Zhang, Z. Gao, N. Song, and X. Li, High-performance supercapacitors and batteries derived from activated banana-peel with porous structures, *Electrochimica Acta* 222 (2016) 1257-1266.

[4] Y. Zhou, J. He, R. Chen, and X. Li, Recent advances in biomass-derived graphene and carbon nanotubes, *Materials Today Sustainability* 18 (2022) 100138.

[5] M.M. Titirici, R.J. White, N. Brun, V.L. Budarin, D.S. Su, F.D. Monte, J.H. Clark, and M.J. MacLachlan, Sustainable carbon materials, *Chemical Society Reviews* 44 (2015) 250-290.

[6] J. Lee, J. Kim, and T. Hyeon, Recent Progress in the Synthesis of Porous Carbon Materials, *Advanced Materials* 18 (2006) 2073-2094.

[7] X. Wu, F. Mu, and H. Zhao, Recent progress in the synthesis of graphene/CNT composites and the energy-related applications, *Journal of Materials Science & Technology* 55 (2020) 16-34.

[8] A.C. Neto, F. Guinea, N.M. Peres, K.S. Novoselov, and A.K. Geim, The electronic properties of graphene, *Reviews of Modern Physics* 81 (2009) 109.

[9] C. Lee, X. Wei, J.W. Kysar, and J. Hone, Measurement of the elastic properties and intrinsic strength of monolayer graphene, *Science* 321 (2008) 385-388.

[10] A.A. Balandin, S. Ghosh, W. Bao, I. Calizo, D. Teweldebrhan, F. Miao, C.N. and Lau, Superior thermal conductivity of single-layer graphene, *Nano Letters* 8 (2008) 902-907.

[11] A.K. Geim, Graphene: status and prospects, *Science* 324 (2009) 1530-1534.

[12] Q. Li, B. Guo, J. Yu, J. Ran, B. Zhang, H. Yan, and J.R. Gong, Highly Efficient Visible-Light-Driven Photocatalytic Hydrogen Production of CdS-Cluster-Decorated Graphene Nanosheets, *Journal of the American Chemical Society* 133 (2011) 10878-10884.

[13] Y. Hernandez, V. Nicolosi, M. Lotya, F.M. Blighe, Z. Sun, S. De, I.T. McGovern, B. Holland, M. Byrne, Y.K. Gun'Ko, and J.J. Boland, High-yield production of graphene by liquid-phase exfoliation of graphite, *Nature Nanotechnology* 3 (2008) 563.

[14] K. Novoselov, V. Fal, L. Colombo, P. Gellert, M. Schwab, and K. Kim, A roadmap for graphene, *Nature* 490 (2012) 192-200.

[15] A. Reina, X. Jia, J. Ho, D. Nezich, H. Son, V. Bulovic, M.S. Dresselhaus, and J. Kong, Large area, few-layer graphene films on arbitrary substrates by chemical vapor deposition, *Nano Letters* 9 (2009) 30-35.

[16] S. Stankovich, D.A. Dikin, R.D. Piner, K.A. Kohlhaas, A. Kleinhammes, Y. Jia, Y. Wu, S.T. Nguyen, and R.S. Ruoff, Synthesis of graphene-based nanosheets via chemical reduction of exfoliated graphite oxide, *Carbon* 45 (2007) 1558-1565.

[17] K.R. Paton, E. Varrla, C. Backes, R.J. Smith, U. Khan, A. O'Neill, C. Boland, M. Lotya, O.M. Istrate, P. King, and T. Higgins, Scalable production of large quantities of defect-free few-layer graphene by shear exfoliation in liquids, *Nature Materials* 13 (2014) 624.

[18] A. Mayyas, D. Steward, and M. Mann, The case for recycling: Overview and challenges in the material supply chain for automotive li-ion batteries, *Sustainable Materials and Technologies* 19 (2019) e00087.

[19] B. Xing, C. Zhang, Y. Cao, G. Huang, Q. Liu, C. Zhang, Z. Chen, G. Yi, L. Chen, J. Yu, Preparation of synthetic graphite from bituminous coal as anode materials for high performance lithium-ion batteries, *Fuel Processing Technology* 172 (2018) 162-171.

[20] K. Vishakha, B. Kishor, and R. Sudha, Natural Polymers – A Comprehensive Review, *International Journal of Research in Pharmaceutical and Biomedical Sciences* 3 (2012) 1597-1613.

[21] Y. Habibi, L.A. Lucia, and O.J. Rojas, Cellulose Nanocrystals: Chemistry, Self-Assembly, and Applications, *Chemical Reviews* 110 (2010) 3479-3500.

[22] Z. Gui, H. Zhu, E. Gillette, X. Han, G.W. Rubloff, L. Hu, and S.B. Lee, Natural Cellulose Fiber as Substrate for Supercapacitor, *ACS Nano* 7 (2013) 6037-6046.

[23] S. Venkatarajan and A. Athijayamani, An overview on natural cellulose fiber reinforced polymer composites, Materials Today: Proceedings 37 (2021) 3620-3624.

[24] A.K. Bledzki and J. Gassan, Composites reinforced with cellulose based fibres, *Progress in Polymer Science* 24 (1999) 221-274.

[25] J.K. Saha and A. Dutta, A Review of Graphene: Material Synthesis from Biomass Sources, *Waste and Biomass Valorization* 13 (2022) 1385-1429.

[26] J.E. Omoriyekomwan, A. Tahmasebi, J. Dou, R. Wang, and J. Yu, A review on the recent advances in the production of carbon nanotubes and carbon nanofibers via microwave-assisted pyrolysis of biomass, *Fuel Processing Technology* 214 (2021) 106686.

[27] A. Abbas, L.T. Mariana, and A.N. Phan, Biomass-waste derived graphene quantum dots and their applications, *Carbon* 140 (2018) 77-99.

[28] W. Wu and B. Yu, Corn Flour Nano-Graphene Prepared by the Hummers Redox Method, *ACS Omega* 5 (2020) 30252-30256.

[29] Z. Gao, N. Song, Y. Zhang, Y. Schwab, J. He, and X. Li, Carbon nanotubes derived from yeast-fermented wheat flour and their energy storage application, *ACS Sustainable Chemistry & Engineering* 6 (2018) 11386-11396.

[30] Z. Kang, E. Wang, B. Mao, Z. Su, L. Chen, and L. Xu, Obtaining carbon nanotubes from grass, *Nanotechnology* 16 (2005) 1192.

[31] B. Goodell, X. Xie, Y. Qian, G. Daniel, M. Peterson, and J. Jellison, Carbon Nanotubes Produced from Natural Cellulosic Materials, *Journal of Nanoscience and Nanotechnology* 8 (2008) 2472-2474.

[32] J. Wang, Z. Wei, Y. Gong, S. Wang, D. Su, C. Han, H. Li, and Y. Wang, Ni-promoted synthesis of graphitic carbon nanotubes from in situ produced graphitic carbon for

dehydrogenation of ethylbenzene, *Chemical Communications* 51 (2015) 12859-12862.

[33] G. Wang, W. Wang, L. Wang, W. Yao, P. Yao, W. Zhu, P. Chen, and Q. Wu, A N-, Fe- and Co-tridoped carbon nanotube/nanoporous carbon nanocomposite with synergistically enhanced activity for oxygen reduction in acidic media, *Journal of Materials Chemistry A* 3 (2015) 17866-17873.

[34] M. Li, Y. Xiong, X. Liu, C. Han, Y. Zhang, X. Bo, and L. Guo, Iron and nitrogen co-doped carbon nanotube@hollow carbon fibers derived from plant biomass as efficient catalysts for the oxygen reduction reaction, *Journal of Materials Chemistry A* 3 (2015) 9658.

[35] E. Thompson, A.E. Danks, L. Bourgeois, and Z. Schnepp, Iron-catalyzed graphitization of biomass, *Green Chemistry* 17 (2015) 551-556.

[36] M.G.S. Bernd, S.R. Braganca, N. Heck, L.C.P.S. Filho, Synthesis of carbon nanostructures by the pyrolysis of wood sawdust in a tubular reactor, *Journal of Materials Research and Technology* 6 (2017) 171-177.

[37] Y. Yao, C. Lian, G. Wu, Y. Hu, F. Wei, M. Yu, and S. Wang, Synthesis of "sea urchin"-like carbon nanotubes/porous carbon superstructures derived from waste biomass for treatment of various contaminants, *Applied Catalysis B: Environmental* 219 (2017) 563-571.

[38] G. Wang, Y. Deng, J. Yu, L. Zheng, L. Du, H. Song, and S. Liao, From Chlorella to Nestlike Framework Constructed with Doped Carbon Nanotubes: A Biomass-Derived, High-Performance, Bifunctional Oxygen Reduction/Evolution Catalyst, *ACS Applied Materials & Interfaces* 9 (2017) 32168-32178.

[39] J. Zhang, H. Zhao, J. Li, H. Jin, X. Yu, Y. Lei, and S. Wang, In Situ Encapsulation of Iron Complex Nanoparticles into Biomass-Derived Heteroatom-Enriched Carbon Nanotubes for High-Performance Supercapacitors, *Advanced Energy Materials* 9 (2018) 1803221.

[40] Y. Zhang, L. Lu, S. Zhang, Z. Lv, D. Yang, J. Liu, Y. Chen, X. Tian, H. Jin, and W. Song, Biomass chitosan derived cobalt/nitrogen doped carbon nanotubes for the electrocatalytic oxygen reduction reaction, *Journal of Materials Chemistry A* 6 (2018) 5740.

[41] A.I. Osman, J. Blewitt, J.K. Abu-Dahrieh, C. Farrell, A.H. Al-Muhtaseb, J. Harrison,

and D.W. Rooney, Production and characterisation of activated carbon and carbon nanotubes from potato peel waste and their application in heavy metal removal, *Environmental Science and Pollution Research* 26 (2019) 37228-37241.

[42] A.I. Osman, E. O'Connor, G. McSpadden, J.K. Abu-Dahrieh, C. Farrell, A.H. Al-Muhtaseb, J. Harrison, D.W. Rooney, Upcycling brewer's spent grain waste into activated carbon and carbon nanotubes for energy and other applications via two-stage activation, *Journal of Chemical Technology & Biotechnology* 95 (2020) 183-195.

[43] S. Zhou, B. Zhang, Z. Liao, L. Zhou, and Y. Yuan, Autochthonous N-doped carbon nanotube/activated carbon composites derived from industrial paper sludge for chromate (VI) reduction in microbial fuel cells, *Science of The Total Environment* 712 (2020) 136513.

[44] M. Yang, Y. Yuan, Y. Li, X. Sun, S. Wang, L. Liang, Y. Ning, J. Li, W. Yin, R. Che, and Y. Li, Dramatically enhanced electromagnetic wave absorption of hierarchical CNT/Co/C fiber derived from cotton and metal-organic-framework, *Carbon* 161 (2020) 517-527.

[45] K. Shi, J. Yan, E. Lester, and T. Wu, Catalyst-free synthesis of multiwalled carbon nanotubes via microwave-induced processing of biomass, *Industrial & Engineering Chemistry Research* 53 (2014) 15012-15019.

[46] R. Afre, T. Soga, T. Jimbo, M. Kumar, Y. Ando, and M. Sharon, Growth of vertically aligned carbon nanotubes on silicon and quartz substrate by spray pyrolysis of a natural precursor: Turpentine oil, *Chemical Physics Letters* 414 (2015) 6-10.

[47] P. Ghosh, R.A. Afre, T. Soga, T. Jimbo, A simple method of producing single-walled carbon nanotubes from a natural precursor: Eucalyptus oil, *Materials Letters* 61 (2007) 3768-3770.

[48] K. Awasthi, R. Kumar, H. Raghubanshi, S. Awasthi, R. Pandey, D. Singh, T.P. Yadav, and O.N. Srivastava, Synthesis of nano-carbon (nanotubes, nanofibres, graphene) materials, *Bulletin of Materials Science* 34 (2011) 607-614.

[49] R. Kumar, R.M. Yadav, K. Awasthi, T. Shripathi, A.S.K. Sinha, R.S. Tiwari, and O.N. Srivastava, Synthesis of carbon and carbon–nitrogen nanotubes using green precursor: jatropha-derived biodiesel, *Journal of Experimental Nanoscience* 8 (2013) 606-620.

[50] R. Kumar, R.K. Singh, P. Kumar, P.K. Dubey, R.S. Tiwari, and O.N. Srivastava, Clean

and Efficient Synthesis of Graphene Nanosheets and Rectangular Aligned-Carbon Nanotubes Bundles Using Green Botanical Hydrocarbon Precursor: Sesame Oil, *Science of Advanced Materials* 6 (2014) 76-83.

[51] N. Gupta, S.M. Gupta, and S.K. Sharma, Carbon nanotubes: synthesis, properties and engineering applications, *Carbon Letters* 29 (2019) 419-447.

[52] L. Chopra and Manikanika, Extraction of cellulosic fibers from the natural resources: A short review, *Materials Today: Proceedings* 48 (2022) 1265-1270.

[53] M. Abdollahifar, S. Doose, H. Cavers, and A. Kwade, Graphite Recycling from End-of-Life Lithium-Ion Batteries: Processes and Applications, *Advanced Materials Technologies* 8 (2023) 2200368.

[54] L. Lu, X. Han, J. Li, J. Hua, and M. Ouyang, A review on the key issues for lithium-ion battery management in electric vehicles, *Journal of Power Sources* 226 (2013) 272-288.

[55] X. Zhao, B. Sánchez, P.J. Dobson, and P.S. Grant, The role of nanomaterials in redox-based supercapacitors for next generation energy storage devices, *Nanoscale* 3 (2011) 839-855.

[56] X. Liu, Z. Huang, S. Oh, B. Zhang, P. Ma, M. Yuen, and J. Kim, Carbon nanotube (CNT)-based composites as electrode material for rechargeable Li-ion batteries: A review, *Composites Science and Technology* 2 (2012) 121-144.

[57] Z. Chen, V. Augustyn, J. Wen, Y. Zhang, M. Shen, B. Dunn, and Y. Lu, High-performance supercapacitors based on intertwined CNT/V2O5 nanowire nanocomposites, *Advanced Materials* 23 (2011) 791-795.

[58] Z. Sun, M. Zheng, H. Hu, H. Dong, Y. Liang, Y. Xiao, B. Lei and Y. Liu, From biomass wastes to vertically aligned graphene nanosheet arrays: A catalyst-free synthetic strategy towards high-quality graphene for electrochemical energy storage, *Chemical Engineering Journal* 336 (2018) 550-561.

[59] L. Chang and Y.H. Hu, Breakthroughs in Designing Commercial-Level Mass-Loading Graphene Electrodes for Electrochemical Double-Layer Capacitors, *Matter* 1 (2019) 596-620.

[60] K. Zhu, C. Wang, Z. Chi, F. Ke, Y. Yang, A. Wang, W. Wang, and L. Miao, How Far Away Are Lithium-Sulfur Batteries From Commercialization?, *Frontiers in Energy*

Research 7 (2019) 123.

[61] K. Liu, S. Yang, L. Luo, Q. Pan, P. Zhang, Y. Huang, F. Zheng, H. Wang, and Q. Li, From spent graphite to recycle graphite anode for high-performance lithium ion batteries and sodium ion batteries, *Electrochimica Acta* 356 (2020) 136856.

[62] S. Natarajan, K. Krishnamoorthy, A. Sathyaseelan, V.K. Mariappan, P. Pazhamalai, S. Manoharan, and S.J. Kim, A new route for the recycling of spent lithium-ion batteries towards advanced energy storage, conversion, and harvesting systems, *Nano Energy* 101 (2022) 107595.

[63] H. Yang, Y. Li, P. Long, J. Han, C. Cao, F. Yao, and W. Feng, Amorphous red phosphorus incorporated with pyrolyzed bacterial cellulose as a free-standing anode for high-performance lithium ion batteries, *RSC Advances* 8 (2018) 17325-17333.

[64] Y. Zhang, Z. Gao, and X. Li, Capillarity Composited Recycled Paper/Graphene Scaffold for Lithium–Sulfur Batteries with Enhanced Capacity and Extended Lifespan, *Small* 13 (2017) 1701927.

[65] Y.R. Lee, A.R. Cho, S. Kim, R. Kim, S. Wang, Y. Han, H. Nam, and D. Lee, Utilizing waste carbon residue from spent lithium-ion batteries as an adsorbent for CO2 capture: A recycling perspective, *Chemical Engineering Journal* 470 (2023) 144232.

[66] G.K. Parshetti, S. Chowdhury, and R. Balasubramanian, Plant derived porous graphene nanosheets for efficient CO_2 capture, *RSC Advances* 4 (2014) 44634-44643.

[67] F. Valdebenito, R. García, K. Cruces, G. Ciudad, G. Chinga-Carrasco, and Y. Habibi, CO2 Adsorption of Surface-Modified Cellulose Nanofibril Films Derived from Agricultural Wastes, *ACS Sustainable Chemistry & Engineering* 6 (2018) 12603-12612.

Chapter 2. Recycled Cellulose Fibers from Paper Waste for Energy Storage

2.1 Introduction

Over the past several decades, energy crises and environmental issues have grown into worldwide problems. To overcome the problems, an ever-growing number of sustainable and eco-friendly materials have been explored for efficient and renewable energy storage. Among them, cellulose fiber (CF), a type of natural polymers, has received extensive attention due to their abundance and wide applications in daily supplies, such as newspapers and paper containers [1, 2]. Although CFs are used in many everyday products, they are not recycled at a very high rate [3]. Purified crystalline CFs have the potential to be employed in high value-added applications, such as natural fiber-reinforced thermosets, thermoplastic composites. Moreover, CF-reinforced separators can be used in lithium-ion (Li-ion) batteries, which are currently the most common energy-storage devices [4-9].

Replacing combustion engines with high-energy batteries is considered to be an effective route to reduce the consumption of fossil fuel and pollutant emissions [9]. However, after years of optimization, the Li-ion battery is approaching its theoretical energy density limit. Electric vehicles that utilize Li-ion batteries will always be restricted in their range by this theoretical limit. In order to increase the effective range of electric vehicles, the energy density of batteries needs to be increased past the theoretical maximum of Li-ion based systems. The lithium-sulfur (Li-S) battery is a promising alternative for replacing current Li-ion battery due to its high theoretical specific capacity (1,675 mAh g^{-1}) and energy density (2,600 Wh kg^{-1}) [10-14]. Li-S batteries are also constructed with inexpensive raw materials. Nevertheless, the practical application of Li-S batteries is hindered by two major challenges: the soluble polysulfides' shuttle effect, which leads to self-discharging, and the growth of mossy Li, arising from nonhomogeneous distribution of Li-ions [15-18]. To overcome the current challenges that prevent Li-S batteries from commercialization, all components in the battery must be systematically optimized. Although the anode, cathode, and electrolyte of Li-S batteries have been researched extensively, the separator has been largely overlooked until recently [19-21]. For example, Yao *et al.* [22] reported on directly coating a thin, porous carbon layer onto the separator,

rendering the Li-S battery with an initial specific capacity of 1,350 mAh g^{-1}, a lifespan of over 500 cycles at 0.5 C, and a capacity decay rate as low as 0.09 % per cycle. In addition to coating, another strategy to enhance separator's efficacy is introducing interlayers between separators and electrodes [23, 24]. These studies indicate that battery performance can be largely enhanced by modifying the separator. However, introducing interlayers increases the overall thickness of the battery, leading to reduced volume energy density and increased ion transport distance. Most recently, studies on carbon- and polymer-based separator coatings and interlayers have been mainly focusing on polysulfide trapping mechanisms via various methods such as nitrogen doping and carbon functionalization [25-30]. This helps mitigate the migration of polysulfides to reach the anode by trapping polysulfides in coating layers or interlayers; however, it inevitably increases the irreversible waste of active materials because some of them are anchored in those layers. Besides, in order to reduce the cost of the synthesis process, new cost-effective raw materials with simple manufacturing strategies are much needed.

The CFs from recycled paper are capable of being manufactured and functionalized as effective additives to enhance separators. Unlike current separators in Li-S batteries, recycled paper is low-cost and readily available. In past research, we used activated paper carbon (APC) with graphene and sulfur as the cathode and a piece of APC as an interlayer between the separator and anode in the Li-S battery to prevent the growth of mossy Li, which led to a stretch of lifespan up to 1,000 cycles with a capacity retention rate of 52.3 % [31]. This created a new possibility to obtain high-performance full Li-S batteries from biomass materials containing CFs. Our previous study indicates that high-temperature treated CF-based biomass materials as interlayers in Li-S batteries can redistribute Li-ions [31]. This effectively prevents the growth of mossy Li. Furthermore, negatively charged functional groups on CFs are expected to mitigate the shuttle effect by repelling soluble polysulfides [32-34]. Unlike the trapping mechanism, this concept reduces the polysulfide shuttle effect without sacrificing active materials. Hence, high-purity CFs are a promising material that may simultaneously mitigate the shuttle effect and mossy Li growth in Li-S batteries.

Here, the CFs extracted from paper waste were uniformly coated onto commercial polypropylene separators on the cathode side when being assembled into Li-S batteries

with an APC/S cathode. It was found that the functional groups on the CFs, such as carboxylic groups and phenolic groups, tended to lose their H^+ ions and form a negatively charged surface, which simultaneously repelled the anionic polysulfides (S_x^{2-}) and redistributed the cationic Li-ions (Li^+) during battery operation (**Figure 2.1**). This led to a joint improvement of rate ability, lifespan, and capacity retention rate. This waste-to-wealth approach employed low-cost CFs to simultaneously prevent the polysulfide shuttle effect and nonhomogeneous Li degradation, paving the way towards commercially viable Li-S batteries.

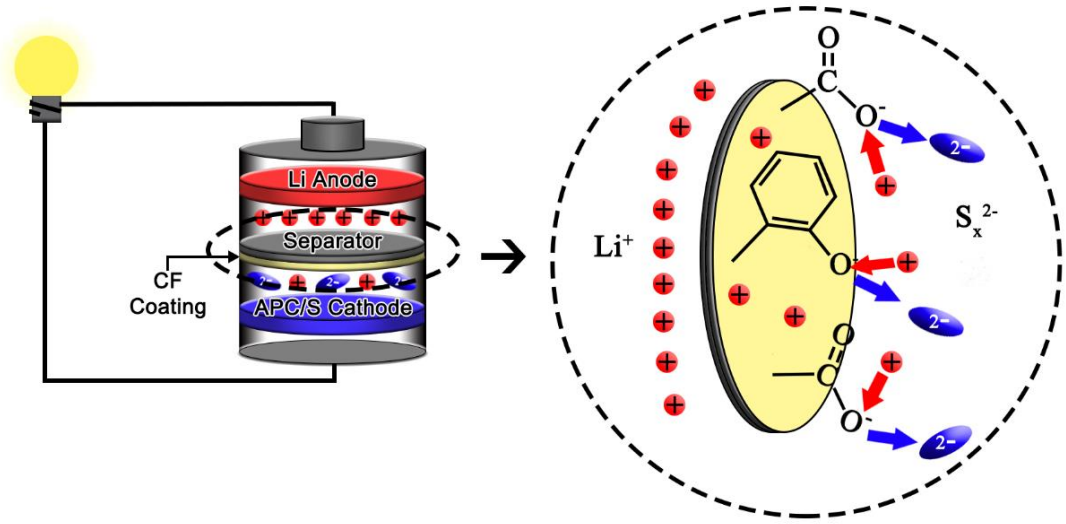

Figure 2.1. Schematic of the CF-coated separator repelling polysulfide-ions and redistributing Li-ions.

2.2 Methods

2.2.1 CF extracting process

A piece of 65 x 50 mm rectangular hardboard was cut into pieces. The 5 wt.% sodium hydroxide (NaOH) solution was stirred with the paper pieces at room temperature, and then the suspension was held at 80 °C for 3 hours. Sonicating was performed to further disperse the CFs after the alkaline treatment. The centrifugation was used three times in DI water and twice in isopropyl alcohol at a rate of 3500 rpm for 10 minutes. Eventually, the isopropyl alcohol was added to preserve the suspension in an organic solution condition.

2.2.2 CF coating process

The Celgard 2400 separators were cut into rectangular pieces. Vacuum filtration was applied to coat the CFs onto the surfaces of the separators. The coated separators were then dried at 60 °C for 12 hours.

2.2.3 Battery assembling

The dried CF-coated separators were punched into circular pieces for coin cells. The electrolyte was produced by dissolving 1 mol L^{-1} lithium bis(trifluoromethanesulfony)imide (LiTFSI) and 0.4 mol L^{-1} $LiNO_3$ in an organic solvent of dimethoxyethane (DME) + 1,3-dioxolane (DOL) at a 1:1 volume ratio. The electrolyte for each battery was 16 μL. An activated paper carbon with sulfur (APC/S) was employed as the electrode. To prepare the APC/S, thin pieces of hardboards were first punched into round pieces and heat-treated in a tube furnace at 1,000 °C for one hour with argon. The APC pieces were then loaded with sulfur powders, followed by a heat treatment at 155 °C for 12 hours and at 200 °C for 2 hours to impregnate sulfur and form the APC/S pieces to be directly used as cathodes. The areal mass loadings of APC/S cathodes in the CF-enabled battery and non-CF battery were 5.15 mg cm^{-2} and 5.38 mg cm^{-2}, respectively. The APC/S cathodes, separators, electrolytes, and Li anodes were assembled into coin cells manually.

2.2.4 Battery disassembling

In order to observe polysulfide distribution, the batteries were in charged condition, disassembled manually in the glove box with argon. Failed batteries were also disassembled manually to conduct a post-failure study. The cycled cathodes, anodes and separators were collected separately for inspection without further treatment.

2.2.5 Materials and Structural Characterization

The SEM (FEI Quanta 650 with EDS detector), XRD (Empyrean Multipurpose X-ray Diffractometer equipped with Cu Kα radiation (λ = 0.15406 nm)), and XPS (PHI Versaprobe III Scanning XPS with Processing Chamber and Reaction Cell) were employed to characterize the as-prepared APC/S cathodes, CF layers, separators, and Li anodes.

2.2.6 Electrochemical Characterization

A LAND CT2003A battery test instrument was used to conduct galvanostatic charge/discharge measurements, including cyclic performance, polarization voltage, and rate performance. The polarization voltage was calculated using the following equation in the test station

$$V_p = V_t - IR_0 - V_{oc} \quad (2.1)$$

where V_p is the polarization voltage, V_t is the terminal voltage, I is the current, R_0 is the ohmic resistance, and V_{oc} is the open-circuit voltage, which were measured by the test station. A CHI 660E electrochemical workstation was used to conduct the EIS test in the frequency range from 100 kHz through 0.01 Hz with an AC perturbation of 5 mV, as well as the CV test from 1.5 V to 2.8 V with a scan rate of 0.0001 V s^{-1}. The Zview software was applied to perform the curve-fitting on the EIS test data.

2.3 Results and Discussion

2.3.1 Characterization of CF-coated separator

The process regarding the fabrication of CF-coated separators is illustrated in **Figure 2.2**. The CF suspension (**Figure 2.3**b) was extracted from a used hardboard (the inset of **Figure 2.3**a) through an alkaline treatment and coated onto a Celgard 2400 polypropylene separator (the inset of **Figure 2.3**c) via vacuum filtration. The CF coating weighed 1.3 mg (0.56 mg cm^{-2}), which was the most optimal CF loading. With lower or higher loading of CFs, consequences that the repelling phenomenon was weak or the CFs partially blocked the route for ion exchanging would occur, respectively. The CFs (**Figure 2.3**c) exhibit a cross laid fiber surface with an average length of more than 1 mm and width of nearly 18 μm, enabling Li-ion transport through the separator. The thickness of the CF coating was measured to be 47.18 μm on average (**Figure 2.3**d).

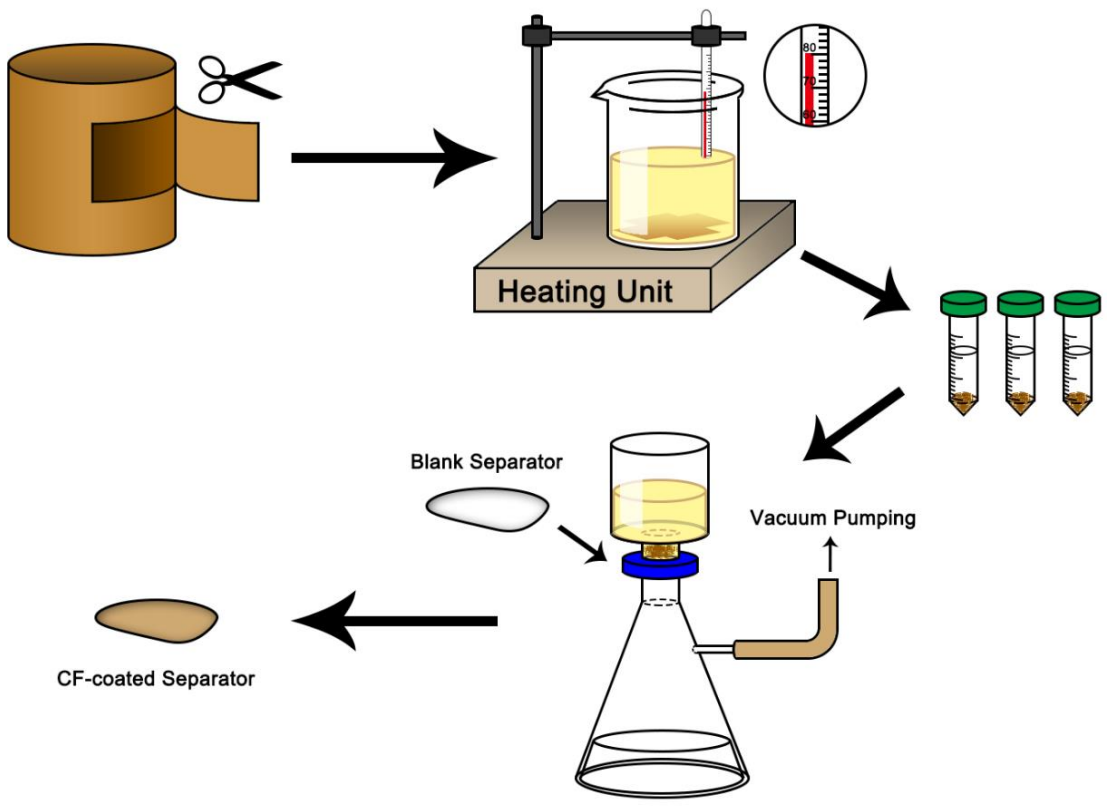

Figure 2.2. Experimental details of preparing CF-coated separators.

Energy-dispersive X-ray Spectroscopy (EDS) mapping showed carbon (**Figure 2.3**e) and oxygen (**Figure 2.3**f) on the CF coating. X-ray Diffraction (XRD) was performed on the recycled paper and CF coating (**Figure 2.3**g). The broad peaks in the 2θ range of 14.0 ° to 16.0 ° and at 22.5 ° match the characteristic peaks of the typical cellulose I (native cellulose) [35]. The peaks at 12.5 °, 25 °, and 27.5 ° correspond to kaolin ($Al_2Si_2O_5(OH)_4$) and the peak at 29.5 ° is characteristic of calcium carbonate ($CaCO_3$) [36, 37]. Both of these compounds are often used as additives in the production of paper products [38]. The alkaline treatment and coating process eliminated most of the impurities, except for a small amount of $CaCO_3$ (1.2 wt%), which should have little impact on the electrochemical reaction [39, 40]. X-ray photoelectron spectrometer (XPS) inspection unveiled a small Ca2p peak (Supporting information, **Figure 2.3**j), which is in good agreement with the XRD results. The three peaks with binding energies of 288.14 eV, 286.56 eV and 284.77 eV (**Figure 2.3**h) are from the carboxylic (-COOH) group, phenolic (-C-OH) group, and aromatic (C=C) group, respectively [41, 42]. This is consistent with the O1s spectrum

(**Figure 2.3**i), where a large peak is located at a binding energy of 533.10 eV (representing co-existence of the -COOH and -C-OH groups), while a small peak at 531.22 eV corresponds to the C=O group [41, 43]. The -COOH and -C-OH groups easily lose their H^+ ions, which enables the separator surface facing the cathode to become negatively charged [32, 44, 45]. The negatively charged surface is expected to repel the anionic S_x^{2-} and attract the cationic Li^+. Consequently, this reduces the shuttle effect of polysulfides, increases the efficiency of the Li-ion exchange, and promotes uniform ion distribution [32, 34]. On the other hand, although nitrogen (N) -containing functional groups were detected in the raw recycled paper, no N-related functional groups were observed on the surface of the CF-coated separator (**Figure 2.3**k) due to the alkaline treatment using NaOH [32]. This rules out the possibility that the CF layer traps polysulfide-ions [46]. Therefore, the negatively charged surface was able to repel soluble polysulfides during battery operation, rendering the active materials fully usable.

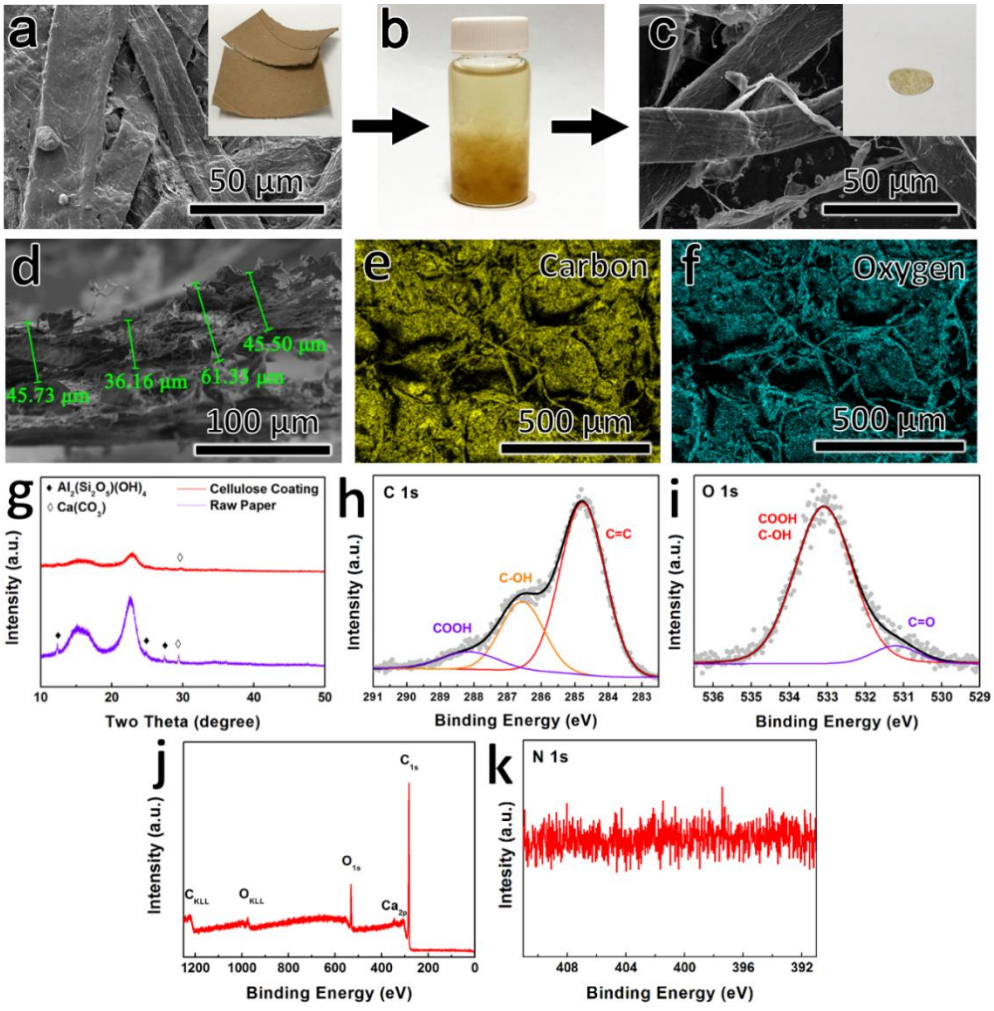

Figure 2.3. (a) SEM image of a paper hardboard. The inset shows the optical image of the hardboard. (b) CF suspension in ethanol. (c) SEM image of the CF-coated separator. The inset shows the optical image of the CF-coated separator. (d) SEM image of the CF coating cross section. (e) EDS map of carbon. (f) EDS map of oxygen. (g) XRD spectra of the hardboard and CF coating. (h) C1s spectrum on the CF coating. (i) O1s spectrum on the CF coating. (j) Surface overall XPS spectrum of the CF coating. (k) N1s spectrum on the CF coating.

2.3.2 Electrochemical performance of CF-enabled batteries

The CF-coated separator was used to construct the Li-S battery with APC/S as the cathode and Li as the anode. **Figure 2.4**a shows the typical charge/discharge cycle (0.16 C) of the CF-coated separator enabled battery. During discharging, four stages (I to IV) appeared and can be ascribed to the formation of S_8^{2-} (stage I), change from S_8^{2-} to S_6^{2-} and S_4^{2-} (stage II), transformation from S_4^{2-} to Li_2S_2 (stage III), and formation of Li_2S solid (stage IV), respectively. The charge curve, similarly, can be grouped into three stages (V to VII), which are ascribed as the change from the solid Li_2S to low-order polysulfides (stage V), conversion from low-order to high-order polysulfides (stage VI), and solidification from high-order polysulfides back to the solid sulfur (stage VII). Compared with the non-CF battery (**Figure 2.4**b), the CF-enabled battery had a flatter plateau at stage I and a much broader and flatter plateau at the stage III in the discharge segment, as well as a flatter plateau at stage VII in the charge segment. These indicate that a large number of polysulfides were repelled, remaining at the cathode side for electrochemical reaction. The faster decrease of the potential at stage IV of the CF-enabled battery also supported the conclusion. Moreover, the CF-enabled battery had a larger potential gap between the charge curve and discharge curve. This is further analyzed in the electrochemical impedance spectroscopy (EIS) section.

Cyclic voltammetry (CV) curves collected after the 0^{th} cycle, 5^{th} cycle, 50^{th} cycle, and 200^{th} cycle are plotted in **Figure 2.4**c. The CV curves with cycle numbers of the CF-enabled battery were consistent with the typical values and similar to the non-CF battery (**Figure 2.4**d) after the initial cycle, indicating that the CF layer was stable without significant changes under electrochemical reaction condition [47]. For the cathodic scan, two sharp troughs, troughs (1) and (2), appeared to represent the two plateaus (stages I and III) in the typical charge/discharge cycle. Similarly, for the anodic scan, the broad peak (3) at 2.5 V indicated that the Li_2S fully transformed into S_8^{2-}, corresponding to the broad

plateau (stage VII) in the charge/discharge cycle. During cycling, the trough (1) moved to a higher potential, and after the 50^{th} cycle, the CF-enabled battery became stabilized. When the battery reached the 200^{th} cycle, the intensity of trough (1) became higher in the discharge scan, which represents the transformation from S_4^{2-} to S_2^{2-} and S^{2-}, indicating developing mitigation of the shuttle effect. For comparison, CV curves after the 0^{th} cycle, 5^{th} cycle, 50^{th} cycle, and 200^{th} cycle were also obtained from the non-CF battery (**Figure 2.4**d), where no substantial difference was observed until the 50^{th} cycle, and hereafter, similarly, a developing intensity of trough (1) was detected. The potential difference between trough (2) and peak (3) in the CF-enabled battery was larger than that in the non-CF battery.

To further study the electrochemical performance of the CF-enabled battery, EIS measurements were carried out on both CF-enabled and non-CF batteries. Except for the impedance curve from the 0^{th} cycle, two semicircles and a straight line emerged in the high-frequency regime, intermediate-frequency regime, and low-frequency regime, respectively (**Figure 2.4**e). The semicircles and the straight line can be further described as an equivalent circuit (the inset of **Figure 2.4**e). The intercept between the semicircle in the high-frequency regime and Z' axis is equal to the R_I in the circuit, denoting the equivalent series resistance R_Ω. The semicircle in the high-frequency regime is the impedance of ions traveling through the solid-electrolyte interface (SEI) of the anode and electrolyte. This semicircle can be represented by a resistor and a capacitor in the equivalent circuit where the resistor is noted as R_{II} (or R_{int}) and can be calculated by the diameter of the semicircle. The second semicircle at the intermediate-frequency regime is known as the impedance of the charge exchanging between the electrodes and electrolyte, which also can be described as a resistor R_{III} (also known as R_{CT}) and a capacitor in the equivalent circuit. The straight line in the low-frequency regime is the Warburg impedance and can be derived from an ion-diffusion limited condition in the electrolyte, written as Z in the circuit. During cycling, the overall impedance of the CF-enabled battery decreased gradually. In contrast, the total impedance of the non-CF battery (**Figure 2.4**f) decreased rapidly after the first cycle and then increased with further cycling.

Another intriguing property of the CF-enabled battery is its rate ability. The rate performance tests were carried out on the batteries after stabilization (**Figure 2.4**g). It was

shown that with the CF coating layer, the rate ability of the battery could still be maintained at a high level, which was even slightly better than the non-CF battery. More specifically, the CF-enabled battery exhibited a good capacity retention rate of 72.43 % from 744.29 mAh g^{-1} to 539.12 mAh g^{-1} when the operation rate was octupled from 0.16 C to 1.28 C, while the non-CF battery showed a retention rate of 70.14 % from 754 mAh g^{-1} to 528.84 mAh g^{-1} with the same operation rate increase. The higher capacity retention rate of the CF-enabled battery was attributed to the repelling mechanism induced by the functional groups on the CFs, which kept more polysulfides at the cathode side. This allowed the relatively more polysulfides to react at a high operation rate. When the operation rate returned to 0.64 C, the specific capacities of both the CF-enabled battery and non-CF battery were fully recovered.

Table 2.1. Comparison among recent work with polymer-based coatings on pp separators.

Coating Material	Coating thickness (μm)	S Loading (mg cm^{-2})	Initial capacity (mAh g^{-1})	Cycle Number	Decay rate (per cycle)	Ref.
rGO-PVDF	130	1.1	1322	200	0.255 %	48
Nafion	1	0.53	781	500	0.080 %	49
Nafion	1-5	1.6	1100	110	0.410 %	50
g-PLiSS	25-32	2	1070	40	0.750 %	51
GO/Nafion	0.13	1.2	1128	200	0.210 %	52
SP/Nafion	3	1.5	859	250	0.190 %	53
PEG/MWCNT	25	3.9	1206	300	0.160 %	54
PAH/PAA	0.03	N/A	1418	50	1.400 %	45
Polydopamine	N/A	1.3	885	200	0.120 %	55
Polypyrrole	10	1.5	586	300	0.040 %	56
PAA-SWNT	7	2.7	770	200	0.120 %	57
PAN/GO	65	0.7-1	987	100	0.395 %	58
Our work	47.18	3.1	1016	**800**	**0.035 %**	

The CF-enabled battery with a sulfur load of 3.1 mg cm^{-2} (60.2 wt%) cycled over 800 times at the rate of 0.5 C. An initial discharge capacity of 1,016.0 mAh g^{-1} (3.15 mAh cm^{-2}) (**Figure 2.5**a) was attained. For comparison, the cyclic performance of the non-CF battery using an APC/S cathode with a sulfur load of 3.3 mg cm^{-2} (61.3 wt%) was also measured. Figure 4e reveals that the capacity decay of the first cycle in the CF-enabled battery was 33.2 %; the retention rate at the 800^{th} cycle was 71.69 % (nearly 0.035 % capacity decay per cycle); and more importantly, there was almost no capacity fading after the initial two cycles. For comparison, the non-CF battery exhibited a capacity decay of 39.6 % after the first cycle, which is 19.3 % larger than that of the CF-enabled battery. The

first cycle decay of a Li-S battery is often induced by the SEI layer formation, causing the irreversible capacity decrease and unusable sulfur formation [59, 60]. Therefore, the CF-reinforced separator can prevent more polysulfide-ions from passing through due to the repelling mechanism of the functional groups than the uncoated separator. In addition, the much smaller overall capacity decay and more stable cyclic performance were also attained in the CF-enabled battery with the assistance of the CF-coated separator. It is worth mentioning that the non-CF battery failed after cycling 466 times, which is much shorter than the lifespan of the CF-enabled battery (over 800 times). The stable cycling performance with the long lifespan of the CF-enabled battery is also better than that of the recent Li-S batteries with similar coatings or interlayers (**Table 2.1**) [25, 26, 28]. The higher capacity of the non-CF battery in the initial cycles was mainly due to the lower impedance in the non-CF battery at the beginning [59, 61]. With the impedance increase of the non-CF battery and the impedance decrease of the CF-enabled battery during cycling, the specific capacity of the CF-enabled battery exceeded that of the non-CF battery. The Coulombic efficiency was close to 100 % in the CF-enabled battery. Due to the excess Li metal anode, the capacity retention rate maintained at 71.69 % after 800 cycles even with the Coulombic efficiency lower than 100 %. After the 350^{th} cycle, the Coulombic efficiency started decreasing, yet it was above 93 % until failure.

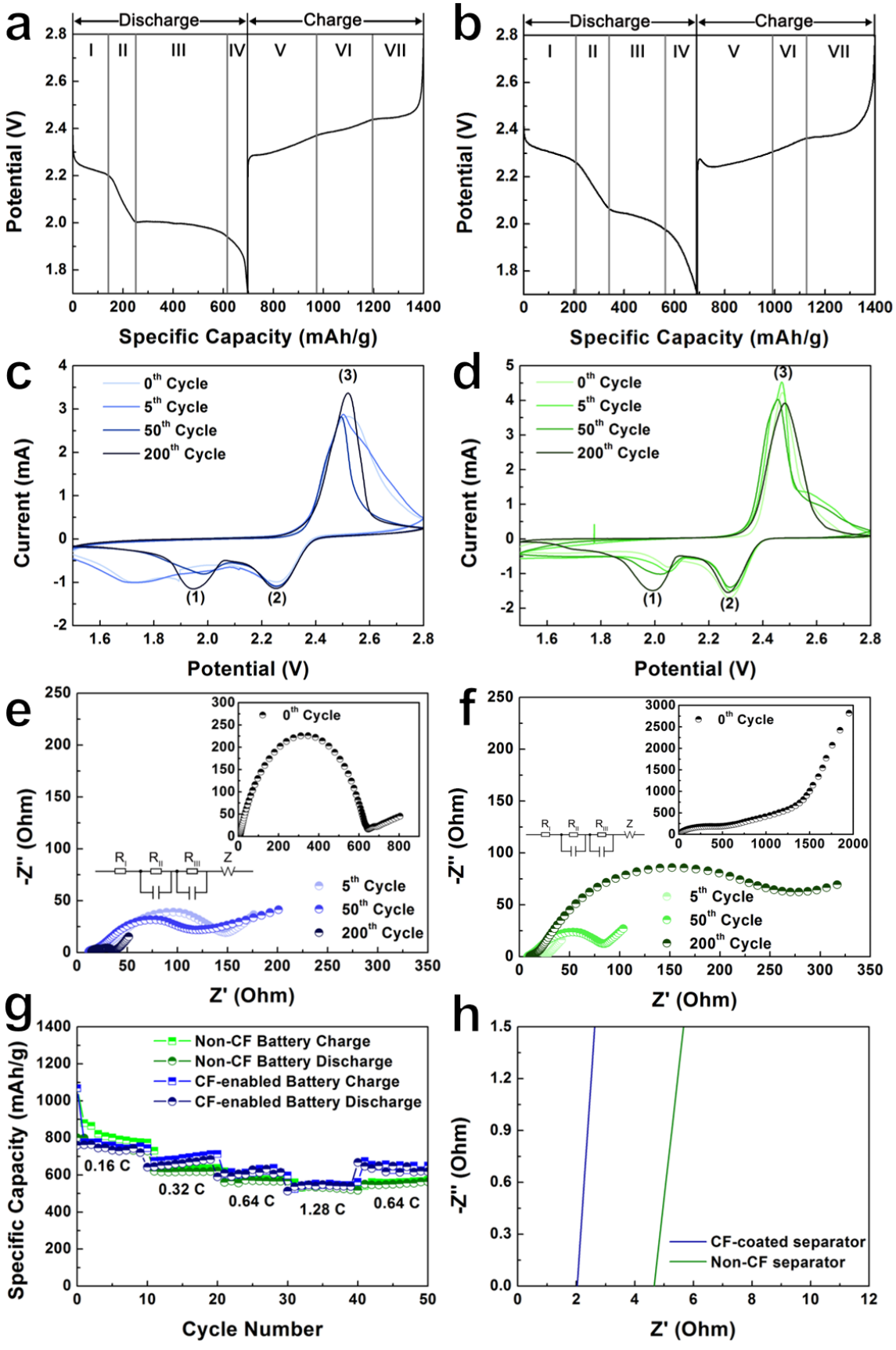
a
Discharge
Charge
I
II
III
IV
V
VI
VII
Potential (V)
Specific Capacity (mAh/g)
b
Discharge
Charge
I
II
III
IV
V
VI
VII
Potential (V)
Specific Capacity (mAh/g)
c
0th Cycle
5th Cycle
50th Cycle
200th Cycle
(1)
(2)
(3)
Current (mA)
Potential (V)
d
0th Cycle
5th Cycle
50th Cycle
200th Cycle
(1)
(2)
(3)
Current (mA)
Potential (V)
e
0th Cycle
5th Cycle
50th Cycle
200th Cycle
-Z'' (Ohm)
Z' (Ohm)
f
0th Cycle
5th Cycle
50th Cycle
200th Cycle
-Z'' (Ohm)
Z' (Ohm)
g
Non-CF Battery Charge
Non-CF Battery Discharge
CF-enabled Battery Charge
CF-enabled Battery Discharge
0.16 C
0.32 C
0.64 C
1.28 C
0.64 C
Specific Capacity (mAh/g)
Cycle Number
h
CF-coated separator
Non-CF separator
-Z'' (Ohm)
Z' (Ohm)

Figure 2.4. (a) Typical charge/discharge cycle of the CF-enabled battery. (b) Typical charge/discharge cycle of the non-CF battery. (c) CV curve of the CF-enabled battery. (d) CV curve of the non-CF battery. (e) EIS curve of the CF-enabled battery. The insets show the EIS curve of the battery before cycling and equivalent circuit of the EIS data. (f) EIS curve of the non-CF battery. The insets show the EIS curve of the battery before cycling and equivalent circuit of the EIS data. (g) Rate performance of the CF-enabled battery and non-CF battery. (h) EIS regression lines of the batteries with only electrolyte and a CF-coated separator or an uncoated separator.

Polarization voltages of the CF-enabled battery and non-CF battery were calculated to describe the polarization characteristics in the batteries during cycling (**Figure 2.5**b). Curve fitting was performed to numerically analyze the variation trend. A large polarization voltage of 672.1 mV was found in the first cycle of the non-CF battery. It then drastically decreased to 496.5 mV in the second cycle, and gradually increased to 667.3 mV up to the 466th cycle. Surprisingly, the CF-enabled battery only experienced an initial polarization voltage of 293.9 mV. It then rapidly decreased to 206.2 mV in the second cycle, and gradually increased to 363.4 mV until the 800th cycle. The much smaller polarization voltage and increasing trend of the CF-enabled battery jointly indicate that the polarization was much lower in the CF-enabled battery than that of the non-CF battery.

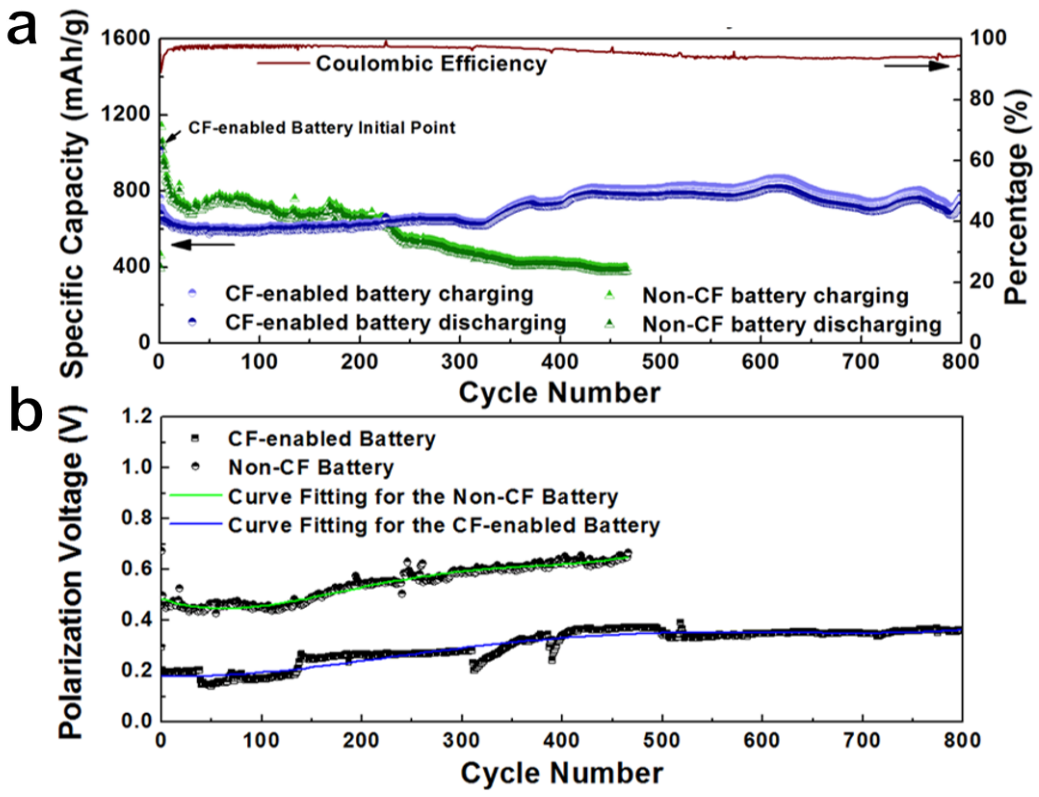

Figure 2.5. (a) Overall cyclic performance of the CF-enabled battery with the areal cathode mass of 5.15 mg cm^{-2} and non-CF battery with the areal cathode mass of 5.38 mg cm^{-2}. (b) Polarization voltage of the CF-enabled battery and non-CF battery.

2.3.3 Analyses of impedance and polarization

To quantitatively analyze the impedance variation with the cycle number, curve fitting (**Figure 2.6**) was employed using Zview with the fitting model same as the circuit inset in **Figure 2.4**e. Comparing the two data sets (**Table 2.2**), the series resistance R_Ω of the CF-enabled battery is slightly larger than that of the non-CF battery due to the introduction of the negatively charged CF layer. This explains the slightly larger gap of potential between the charge and discharge curves in the typical charge/discharge cycle analysis section, and the larger potential difference between the trough (2) and peak (3) in the CV analysis section of the CF-enabled battery than those of the non-CF battery. In accordance with the fitting data, high resistance was obtained, which corresponds to the semicircles at the high-frequency regime in both the CF-enabled battery (565.8 Ω) and non-CF battery (203.3 Ω) before cycling, which suggests the existence of oxidized layers on the Li anodes. This impeded the Li-ion transport in the battery. These values decreased drastically and remained low after the first cycle as the oxidized layers were removed. Upon cycling (the end of the 5^{th} cycle), the larger R_{int} in the CF-enabled battery (19.37 Ω) than that in the non-CF battery (3.74 Ω) represented a faster formation of the SEI layer. As the cycling proceeded, the CF-enabled battery exhibited a decreasing trend of the R_{int}, while the R_{int} of the non-CF battery increased and then stabilized. The reduction of R_{int} in the CF-enabled battery may be ascribed to the extra kinetic energy from the negatively charged CF layer on particles, such as Li-ions during charging and electrons during discharging. This energy accelerated particle transport, which gradually weakened the formation of SEI layers. In addition, the higher R_{CT} in the CF-enabled battery (101.8 Ω) than that in the non-CF battery (13.19 Ω) at the end of the 5^{th} cycle could arise from the inactive CF layer introducing an impedance layer at the beginning, which decreased the electrically conductive area [59]. However, as the CF layer being activated during cycling (losing H^+ ions), the R_{CT} decreased rapidly because the negatively charged layer repelled the anions and accelerated the transport of cations. Therefore, the side reactions between the cations and anions were decreased, leading to an increasingly thinner impedance layer formed on the electrode. This

decreasing trend can also explain the increasing specific capacity after the initial cycles and the trough (1) in the CV curve moving to a higher potential [47, 59, 62]. In contrast, the absence of the CF layer in the non-CF battery induced a cumulative impedance layer, leading to an increase in R_{CT} and a consecutive decay in capacity [59].

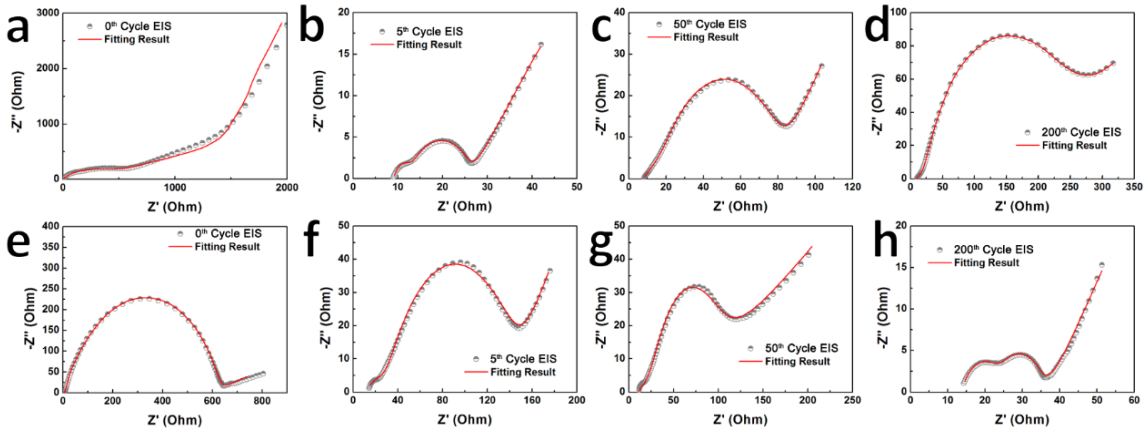

Figure 2.6. EIS curve fitting data for the non-CF battery at the (a) 0th cycle, (b) 5th cycle, (c) 50th cycle, (d) 200th cycle, and the CF-enabled battery at the (e) 0th cycle, (f) 5th cycle, (g) 50th cycle, (h) 200th cycle.

Table 2.2. Curve fitting data of the EIS test.

	Non-CF Battery				CF-enabled Battery			
	0th Cycle	5th Cycle	50th Cycle	200th Cycle	0th Cycle	5th Cycle	50th Cycle	200th Cycle
R_{Ω} (Ohm)	2.987	9.083	7.782	8.71	2.419	11.09	10.1	13.55
R_{SEI} (Ohm)	203.3	3.74	18.02	20.33	565.6	19.37	16.2	9.986
R_{CT} (Ohm)	288.1	13.19	54.17	183	-	101.8	50.2	12.51

Due to the introduction of the negatively charged functional group layer on the separator, the potential balance in the battery was maintained to a certain degree, leading to a smaller polarization. To better understand the polarization mechanism, the expression for polarization provided by the separator [63] can be formulated as

$$E^{\Delta s} = E_1^{\Delta s} + E_2^{\Delta s} = \frac{1}{j_{appl}}\left[\int_0^{L^s}\left(\frac{j_L^2}{\kappa_{eff}}\right)dx - \int_0^{L^s} j_L \cdot \frac{2RT}{c_L F}\kappa_c \frac{\partial c_L}{\partial x}dx\right] \quad (2.2)$$

where $E^{\Delta s}$ is the polarization of the separator, $E_1^{\Delta s}$ is the polarization caused by the ohmic potential drop, $E_2^{\Delta s}$ is the diffusion polarization , j_{appl} is the applied current density, L^s is the thickness of the separator, j_L is the current density in electrolyte, κ_{eff} is the effective ionic conductivity accounting for the porosity and tortuosity, R is the ideal gas constant, T is the temperature, c_L is the concentration in the electrolyte, F is the

Faraday's constant, and κ_c is the concentration conductivity. Because the two batteries were cycled in the same conditions, and the only difference between them was the CF layer, we can consider that j_{appl}, L^s, j_L and T are invariant. The ionic conductivity κ_{eff} can be calculated from the following equation [64, 65]

$$\kappa_{eff} = \frac{d}{A \cdot R_e} \tag{2.3}$$

where *d* is the thickness of electrolyte, *A* is the contact area, and R_e is the resistance of the electrolyte. *d* can be obtained by measuring the thicknesses of the separator and coating layer, *A* is the area of the separator, and R_e can be obtained from the intercept of Z' axis and the regression of the straight line (denoting the Warburg impedance) derived from an ion-diffusion limited condition in the EIS data. To obtain R_e, two batteries with only electrolyte and a CF-coated separator or an uncoated separator were separately built. From the regression of the EIS results (**Figure 2.4**h), the R_e of the CF-coated separator battery was calculated to be 2.028 Ω, while the R_e of the non-CF separator battery was calculated to be 4.658 Ω. With *d* of 67.18 μm for the CF-coated separator and 20 μm for the uncoated separator, and *A* value of 3.1416 cm^2 for both batteries, κ_{eff} values of the CF-coated separator and uncoated separator were calculated to be $1.054 \cdot 10^{-3}$ S cm^{-1} and $1.367 \cdot 10^{-4}$ S cm^{-1}, respectively. During battery cycling, the *d* of the CF-coated separator would become smaller, yet it would be still larger than that of the uncoated separator. Therefore, the κ_{eff} was higher in the CF-enabled battery, indicating that the polarization from the ohmic potential drop ($E_1^{\Delta s}$) was lower. On the other hand, practically, the κ_c is proportional to the square root of c_L (i.e., $\kappa_c = \alpha\sqrt{c_L}$, where α is a constant) [66], so the second term in equation (2.2) can be rewritten as

$$E_2^{\Delta s} = \frac{1}{j_{appl}}\left[-\int_0^{L^s} j_L \cdot \frac{2\alpha RT}{\sqrt{c_L}F} \cdot \frac{\partial c_L}{\partial x}\, dx\right] = \frac{1}{j_{appl}}\left[-\int_0^{L^s} j_L \cdot \frac{4\alpha RT}{F} \cdot \frac{\partial \sqrt{c_L}}{\partial x}\, dx\right] \tag{2.4}$$

where $\frac{\partial \sqrt{c_L}}{\partial x} \propto \frac{\partial c_L}{\partial x}$. Considering that the CF layer provided the extra kinetic energy, the ionic mobility was higher in the CF-enabled battery than that in the non-CF battery. Because of the higher mobility in the CF-enabled battery, the concentration gradient $\left|\frac{\partial c_L}{\partial x}\right|$ was lower, and so was the $\left|\frac{\partial \sqrt{c_L}}{\partial x}\right|$, leading to lower diffusion polarization. Due to the decrease in polarizations from both the ohmic potential drop and diffusion, consequently,

the overall polarization induced by the CF-coated separator was much lower. Theoretically, the total polarization of a battery is calculated by adding all polarizations from different parts within the battery, which explains the relatively lower polarization voltage of the CF-enabled battery than that of the non-CF battery.

2.3.4 Sulfur distribution in batteries

The cycled batteries were disassembled to determine how the CFs affected the distribution of polysulfides. SEM/EDS inspections were carried out on the APC/S cathode, Li anode, separator surface towards the cathode (separator@cathode), and separator surface towards the anode (separator@anode) (**Figure 2.7**a). The corresponding sulfur contents on the surfaces of individual components after cycling 10 times for the CF-enabled battery and non-CF battery are graphically summarized in **Figure 2.7**b. Compared with the non-CF battery, the CF-enabled battery possessed a higher amount of sulfur on the cathode surface and separator@cathode, while less sulfur content was observed on the anode surface and separator@anode. This suggests that polysulfides were repelled by the CF-coated separator and remained at the cathode side in the CF-enabled battery. Moreover, the SEM image of the APC/S cathode surface in the CF-enabled battery after cycling 10 times (**Figure 2.7**c) shows pitting all over, which provided adequate spaces to load sulfur. This resulted in the sulfur content of 60.4 wt%. These pits were created by the CF layer due to the repelling behavior within the battery and could also be observed on the cellulose fibers. In the non-CF battery, no pitting was found on the APC/S cathode surface after cycling 10 times (**Figure 2.7**d). This led to a lower sulfur content of 47.7 wt%. On the other hand, the Li anode surface of the CF-enabled battery (**Figure 2.7**e) after 10 cycles showed fewer sulfur-containing regimes (24.2 wt%) than that (37.7 wt%) of the non-CF battery (**Figure 2.7**f). The impurities on the separator@cathode were found to be Ca-containing salts, which came originally from the CF coating and should have little impact on the electrochemical reaction [39, 40].

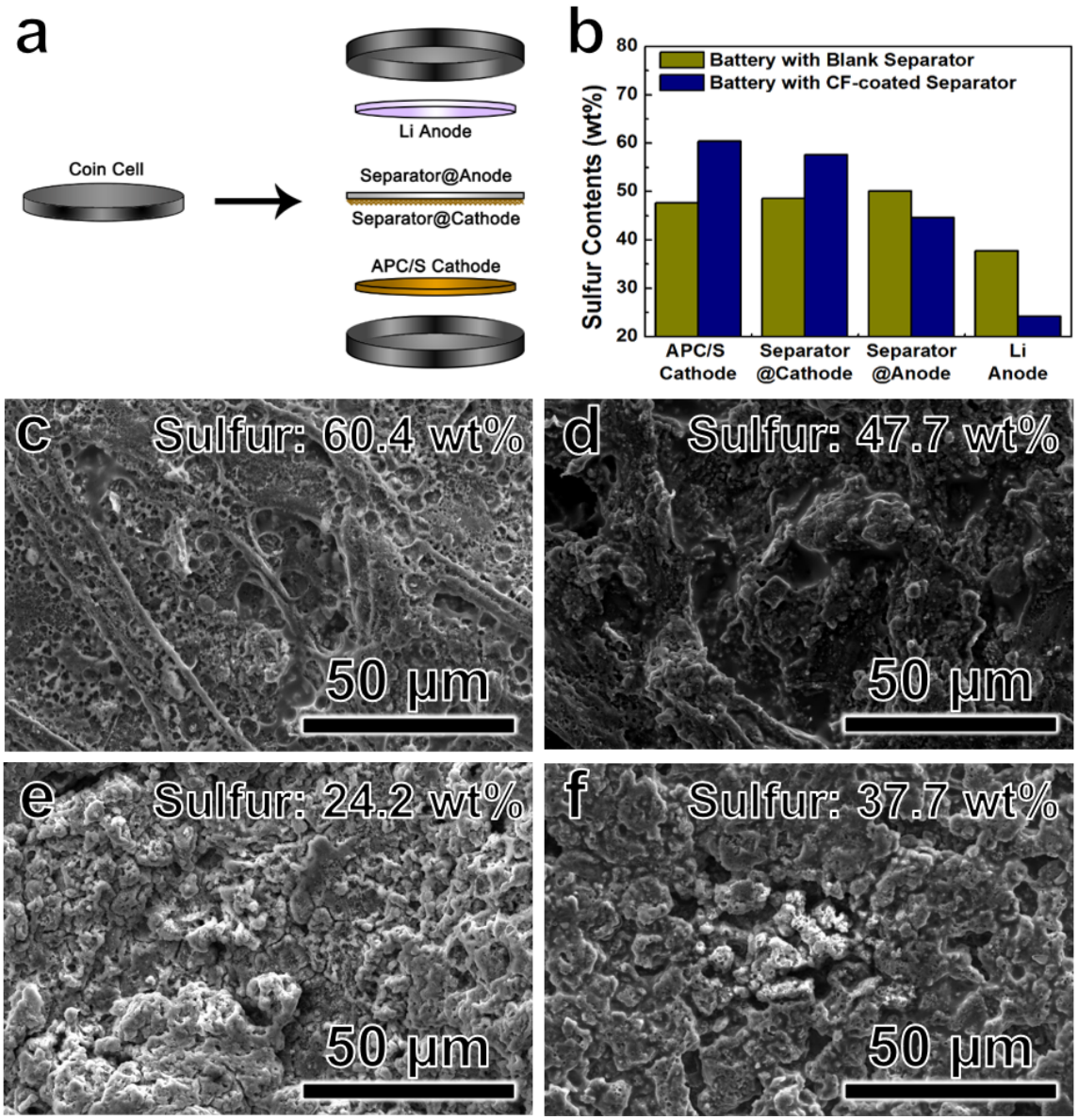

Figure 2.7. (a) Graphical constitute of a Li-S battery. (b) Sulfur contents on different surfaces after cycling 10 times. (c) SEM image of the APC/S cathode surface in the CF-enabled battery after cycling 10 times. (d) SEM image of the APC/S cathode surface in the non-CF battery after cycling 10 times. (e) SEM image of the Li anode surface in the CF-enabled battery after cycling 10 times. (f) SEM image of the Li anode surface in the non-CF battery after cycling 10 times.

2.3.5 Post-failure analysis of cycled batteries

The CF-enabled battery and non-CF battery failed after the 800th cycle and 466th cycle, respectively. Both batteries failed due to short circuiting, which was probably caused by the penetration of Li dendrites. Therefore, the longer lifespan of the CF-enabled battery is ascribed to the negatively charged CF-coated separator which inhibited Li dendrite growth

by redistributing the Li-ions during cycling. SEM inspection unveiled that local degradation of the Li anode in the non-CF battery (**Figure 2.8**b) was much more severe than that of the CF-enabled battery (**Figure 2.8**a). A similar conclusion can be made by comparing **Figure 2.8**c and d, where the red circles highlight the holes caused by the nonhomogeneous Li degradation on the Li anode in the non-CF battery. In contrast, no hole appeared on the Li piece in the CF-enabled battery. The optical inspection also revealed a more corroded Li anode in the non-CF battery (the inset of **Figure 2.8**d), and a relatively flat and intact Li anode in the CF-enabled battery (the inset of **Figure 2.8**c). The improved homogeneity of Li-ion distribution and degradation of the anode in the CF-enabled battery was enabled by the negatively charged CF layer redistributing Li-ions and repelling polysulfides. In addition, more pores and scratches caused by mossy Li were found on the non-CF separator than those on the CF-coated separator (**Figure 2.9**), which also illustrates the more uniform Li distribution in the CF-enabled battery. The cathode in the CF-enabled battery kept its fiber structure, yet the fiber structure was barely seen on the cathode surface in the non-CF battery. In addition to more homogeneous distribution of Li-ions, the CF-enabled battery (**Figure 2.10**) demonstrated a suppressed polysulfide shuttle effect; lower sulfur content of 10.9 wt% was found on the cross section of the anode in the CF-enabled battery whereas higher sulfur content of 16.5 wt% was observed on the cross section of the anode in the non-CF battery.

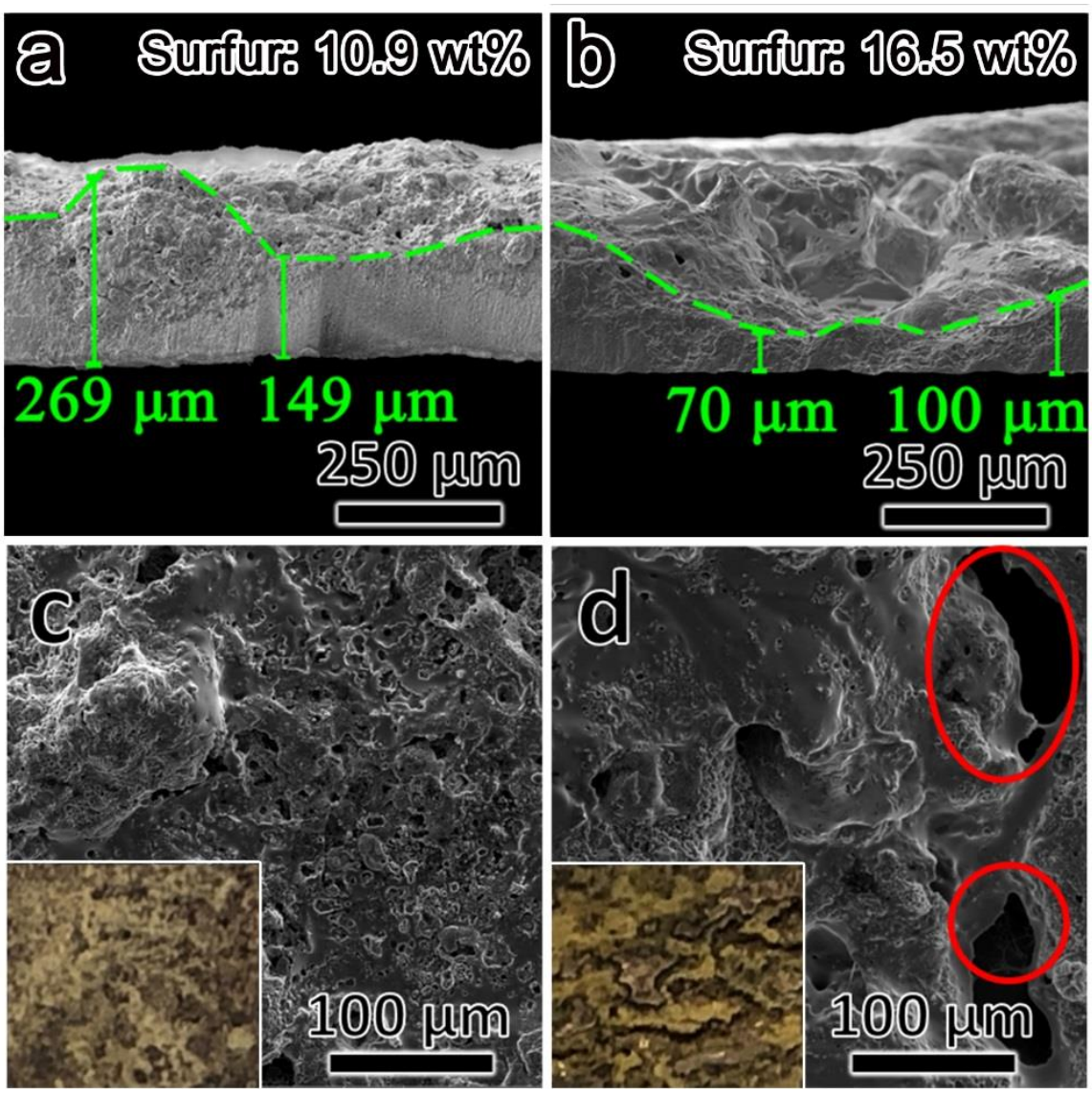

Figure 2.8. (a) SEM image of the Li anode cross section in the end-of-life CF-enabled battery. (b) SEM image of the Li anode cross section in the end-of-life non-CF battery. (c) SEM image of the Li anode surface in the end-of-life CF-enabled battery. The inset shows the optical image of the Li anode surface in the end-of-life CF-enabled battery. (d) SEM image of the Li anode surface in the end-of-life non-CF battery. The inset shows the optical image of the Li anode surface in the end-of-life non-CF battery.

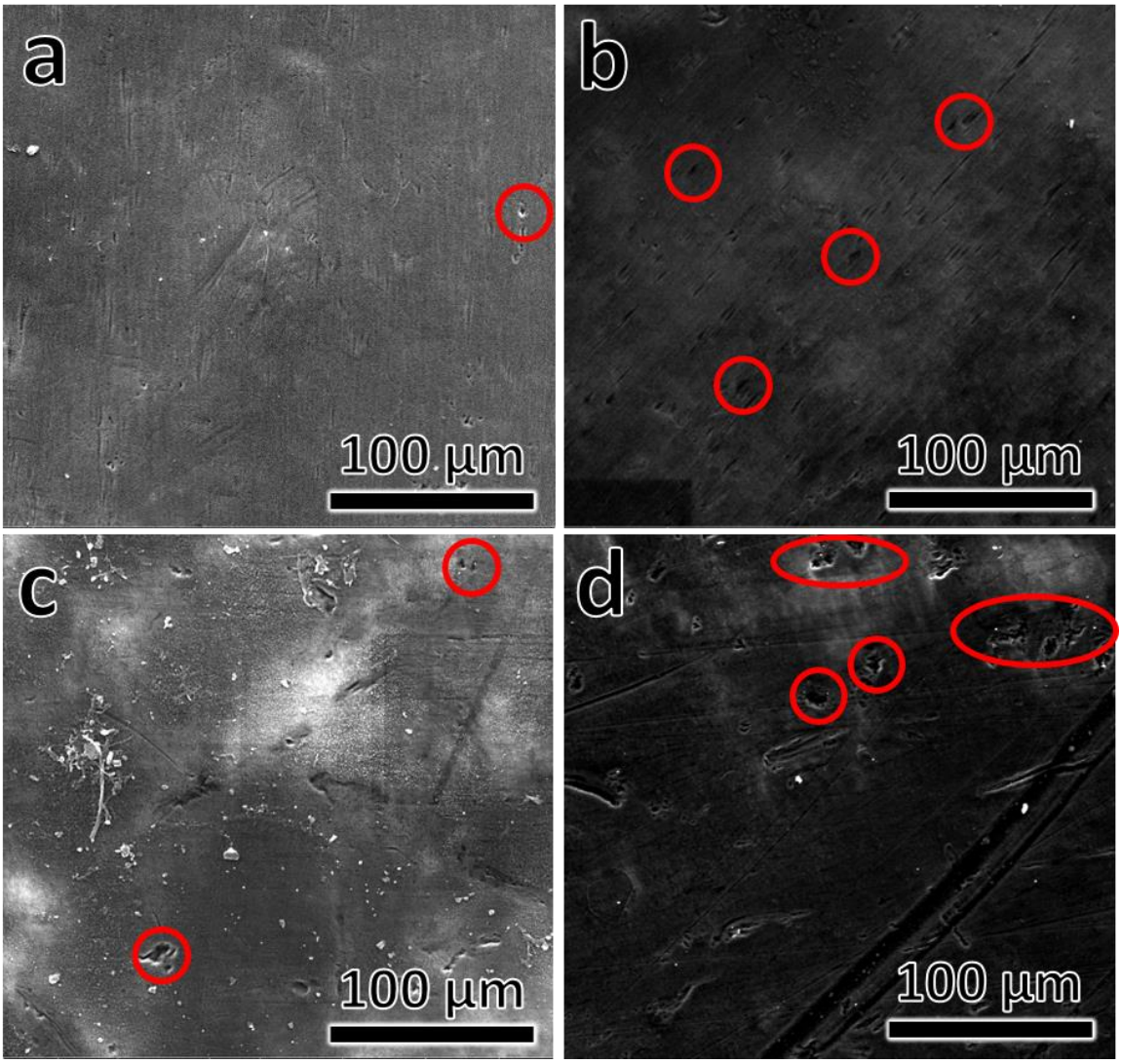

Figure 2.9. (a) SEM image of the separator surface facing the anode in the end-of-life CF-enabled battery. (b) SEM image of the separator facing the anode in the end-of-life non-CF battery. (c) SEM image of the separator surface facing the cathode in the CF-enabled battery. (d) SEM image of the separator surface facing the cathode in the non-CF battery.

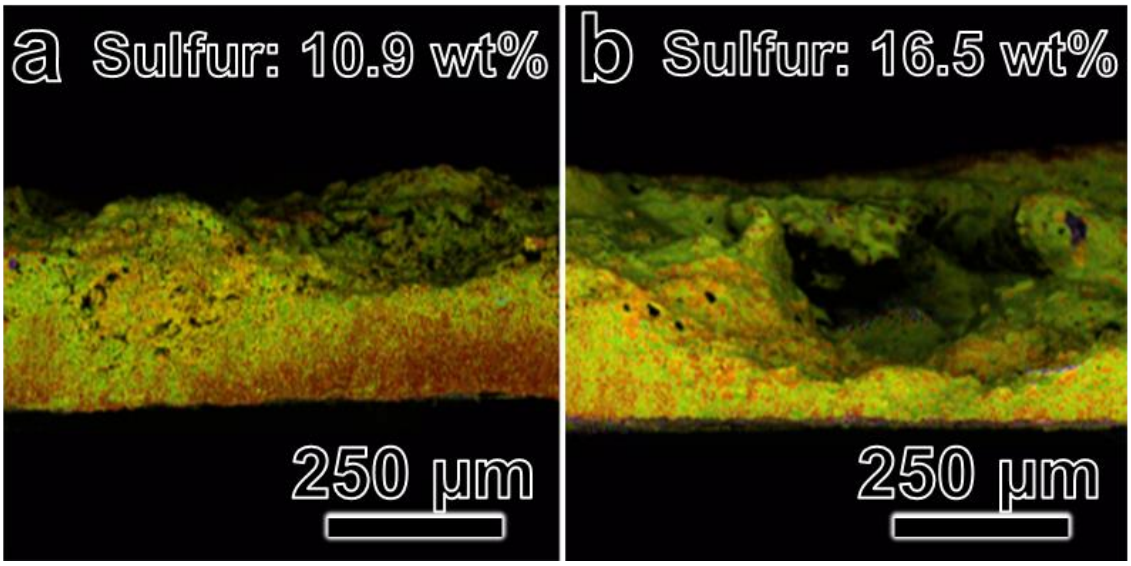

Figure 2.10. EDS maps of Li metal anode in (a) CF-enabled battery and (b) non-CF battery.

2.4 Conclusions

Recycled paper hardboards were upcycled into CF-coated separators for Li-S batteries via a cost-effective method. The functional groups on CFs, including -COO^- and -C-O^-, rendered a negatively charged surface which redistributed Li^+ and repelled S_x^{2-}, simultaneously mitigating the shuttle effect and mossy Li growth without sacrificing the active materials. The CF-enabled battery exhibited good rate ability with a 72.43 % retention rate when the operation rate was octupled from 0.16 C to 1.28 C. The battery was cycled over 800 times with a capacity retention rate of 71.69 % at 0.5 C. The CF-enabled battery exhibited a smaller polarization than that of the non-CF battery due to the lower ohmic potential drop and diffusion polarization. The CF-coated separators are promising innovations to simultaneously overcome the two major challenges of Li-S batteries - the shuttle effect of polysulfides and nonhomogeneous degradation of Li. The readily accessible, renewable materials used in this study provide the large potential for the commercialization of low-cost, eco-friendly Li-S batteries.

Reference

[1] H. P. S. Abdul Khalil, A. H. Bhat, A. F. Ireana Yusra, Green composites from sustainable cellulose nanofibrils: A review, *Carbohydrate Polymers* 87 (2012) 963-979.

[2] S. Osong, S. Norgren, and P. Engstrand, Processing of wood-based microfibrillated cellulose and nanofibrillated cellulose, and applications relating to papermaking: a review, *Cellulose* 23 (2016) 93-123.

[3] M. Jonoobi, R. Oladi, Y. Davoudpour, K. Oksman, A. Dufresne, Y. Hamzeh, and R. Davoodi, Different preparation methods and properties of nanostructured cellulose from various natural resources and residues: a review, *Cellulose* 22 (2015) 935-969.

[4] L. Mohammed, M. N. M. Ansari, G. Pua, M. Jawald, and M. S. Islam, A Review on Natural Fiber Reinforced Polymer Composite and Its Applications, *International Journal of Polymer Science* 2015 (2015) 243947.

[5] I. Siró, and D. Plackett, Microfibrillated cellulose and new nanocomposite materials: a review, *Cellulose* 17 (2010) 459-494.

[6] D. Boriboon, T. Vongsetskul, P. Limthongkul, W. Kobsiriphat, and P. Tammawat, Cellulose ultrafine fibers embedded with Titania particles as a high performance and eco-friendly separator for lithium-ion batteries, *Carbohydrate Polymers* 189 (2018) 145-151.

[7] H. Zhang, J. Liu, M. Guan, Z. Shang, Y. Sun, Z. Lu, H. Li, X. An, and H. Liu, Nanofibrillated Cellulose (NFC) as a Pore Size Mediator in the Preparation of Thermally Resistant Separators for Lithium Ion Batteries, *ACS Sustainable Chemistry & Engineering* 6 (2018) 4838-4844.

[8] J. J. Zhang, Z. H. Liu, Q. S. Kong, C. J. Zhang, S. P. Pang, L. P. Yue, X. J. Wang, J. H. Yao, and G. L. Cui, Renewable and Superior Thermal-Resistant Cellulose-Based Composite Nonwoven as Lithium-Ion Battery Separator, *ACS Applied Materials & Interfaces* 5 (2013) 128-134.

[9] J. Y. Hwang, H. M. Kim, S. Shin, and Y. K. Sun, Designing a High-Performance Lithium-Sulfur Batteries Based on Layered Double Hydroxides-Carbon Nanotubes Composite Cathode and a Dual-Functional Graphene-Polypropylene-Al_2O_3 Separator, *Advanced Functional Materials* 28 (2018) 1704294.

[10] W. L. Cai, G. R. Li, K. L. Zhang, G. N. Xiao, C. Wang, K. F. Ye, Z. W. Chen, Y. C. Zhu, and Y. T. Qian, Conductive Nanocrystalline Niobium Carbide as High-Efficiency Polysulfides Tamer for Lithium-Sulfur Batteries, *Advanced Functional Materials* 28 (2018) 1704965.

[11] Y. Zhong, L. Yin, P. He, W. Liu, Z. Wu, and H. Wang, Surface Chemistry in Cobalt Phosphide-Stabilized Lithium–Sulfur Batteries, *Journal of the American Chemical Society* 140 (2018) 1455-1459.

[12] X. Liang, C. Hart, Q. Pang, A. Garsuch, T. Weiss, and L. F. Nazar, A highly efficient polysulfide mediator for lithium–sulfur batteries, *Nature Communications* 6 (2015) 5682.

[13] A. Manthiram, S. H. Chung, and C. X. Zu, Lithium-Sulfur Batteries: Progress and Prospects, *Advanced Materials* 27 (2015) 1980-2006.

[14] Y. Zhang, Z. Gao, N. Song, J. He, and X. Li, Graphene and its derivatives in lithium–sulfur batteries, *Materials Today Energy* 9 (2018) 319-335.

[15] Y. Y. Zhang, F. M. Heim, N. N. Song, J. L. Bartlett, and X. D. Li, New Insights into Mossy Li Induced Anode Degradation and Its Formation Mechanism in Li-S Batteries, *ACS Energy Letters* 2 (2017) 2696-2705.

[16] J. Zhang, M. Huang, B. Xi, K. Mi, A. Yuan, and S. Xiong, Systematic Study of Effect on Enhancing Specific Capacity and Electrochemical Behaviors of Lithium–Sulfur Batteries, *Advanced Energy Materials* 8 (2018) 1701330.

[17] H. J. Peng, J. Q. Huang, X. B. Cheng, and Q. Zhang, Review on High-Loading and High-Energy Lithium–Sulfur Batteries, *Advanced Energy Materials* 7 (2017) 1700260.

[18] R. P. Fang, S. Y. Zhao, Z. H. Sun, D. W. Wang, H. M. Cheng, and F. Li, More Reliable Lithium-Sulfur Batteries: Status, Solutions and Prospects, *Advanced Materials* 29 (2017) 1606823.

[19] R. Elazari, G. Salitra, A. Garsuch, A. Panchenko, and D. Aurbach, Sulfur-Impregnated Activated Carbon Fiber Cloth as a Binder-Free Cathode for Rechargeable Li-S Batteries, *Advanced Materials* 23 (2011) 5641-5644.

[20] G. Q. Ma, Z. Y. Wen, M. F. Wu, C. Shen, Q. S. Wang, J. Jin, and X. W. Wu, A lithium anode protection guided highly-stable lithium-sulfur battery, *Chemical Communications* 50 (2014) 14209-14212.

[21] J. Q. Huang, Q. Zhang, and F. Wei, Multi-functional separator/interlayer system for high-stable lithium-sulfur batteries: Progress and prospects, *Energy Storage Materials* 1 (2015) 127-145.

[22] H. B. Yao, K. Yan, W. Y. Li, G. Y. Zheng, D. S. Kong, Z. W. Seh, V. K. Narasimhan, Z. Liang, and Y. Cui, Improved lithium-sulfur batteries with a conductive coating on the separator to prevent the accumulation of inactive S-related species at the cathode-separator interface, *Energy & Environmental Science* 7 (2014) 3381.

[23] Y.S. Su and A. Manthiram, A new approach to improve cycle performance of rechargeable lithium–sulfur batteries by inserting a free-standing MWCNT interlayer, *Chemical Communications* 48 (2012) 8817-8819.

[24] B. Zheng, N. Li, J. Yang, and J. Xi, Waste cotton cloth derived carbon microtube textile: a robust and scalable interlayer for lithium–sulfur batteries, *Chemical Communications* 55 (2019) 2289-2292.

[25] J. Yoo, S.J. Cho, G.Y. Jung, S.H. Kim, K.H. Choi, J.H. Kim, C.K. Lee, S.K. Kwak, and S.Y. Lee, COF-Net on CNT-Net as a Molecularly Designed, Hierarchical Porous Chemical Trap for Polysulfides in Lithium–Sulfur Batteries, *Nano Letters* 16 (2016) 3292-3300.

[26] S. Li, G. Ren, M.N.F. Hoque, Z. Dong, J. Warzywoda, and Z. Fan, Carbonized cellulose paper as an effective interlayer in lithium-sulfur batteries, *Applied Surface Science* 396 (2017) 637-643.

[27] H. Yuan, T. Liu, Y. Liu, J. Nai, Y. Wang, W. Zhang, and X. Tao, A review of biomass materials for advanced lithium–sulfur batteries, *Chemical Science* 10 (2019) 7484.

[28] M. Rana, M. Li, X. Huang, B. Luo, I. Gentle, and R. Knibbe, Recent advances in separators to mitigate technical challenges associated with re-chargeable lithium sulfur batteries, *Journal of Materials Chemistry A* 7 (2019) 6596.

[29] J. Li, Y. Guo, P. Wen, J. Zhu, C. Jiao, L. Zhong, J. Wang, A.L. Narayana, J. Li, and Y. Qiu, Constructing a sandwich-structured interlayer with strong polysulfides adsorption ability for high-performance lithium-sulfur batteries, *Materials Today Energy* 14 (2019) 100339.

[30] C.H. Chang, S.H. Chung, S. Nanda, and A. Manthiram, A rationally designed polysulfide-trapping interface on the polymeric separator for high-energy Li–S batteries, *Materials Today Energy* 6 (2017) 72-78.

[31] Y. Y. Zhang, Z. Gao, and X. D. Li, Capillarity Composited Recycled Paper/Graphene Scaffold for Lithium-Sulfur Batteries with Enhanced Capacity and Extended Lifespan, *Small* 13 (2017) 1701927.

[32] X. W. Yu, J. Joseph and A. Manthiram, Suppression of the polysulfide-shuttle behavior in Li-S batteries through the development of a facile functional group on the polypropylene separator, *Materials Horizons* 3 (2016) 314.

[33] Y. Lu, S. Gu, J. Guo, K. Rui, C. H. Chen, S. P. Zhang, J. Jin, J. H. Yang, and Z. Y. Wen, Sulfonic Groups Originated Dual-Functional Interlayer for High Performance Lithium-Sulfur Battery, *ACS Applied Materials & Interfaces* 9 (2017) 14878-14888.

[34] T. Y. Lei, W. Chen, W. Q. Lv, J. W. Huang, J. Zhu, J. W. Chu, C. Y. Yan, C. Y. Wu, Y. C. Yan, W. D. He, J. Xiong, Y. R. Li, C. L. Yan, J. B Goodenough, and X. F. Duan, Inhibiting Polysulfide Shuttling with a Graphene Composite Separator for Highly Robust Lithium-Sulfur Batteries, *Joule* 2 (2018) 2091-2104.

[35] S. H. Kim, C. M. Lee, and K. Kafle, Characterization of crystalline cellulose in biomass: Basic principles, applications, and limitations of XRD, NMR, IR, Raman, and SFG, *Korean Journal of Chemical Engineering* 30 (2013) 2127-2141.

[36] L. Hajji, A. Boukir, J. Assouik, S. Pessanha, J. L. Figueirinhas, M. L. Carvalho, Artificial aging paper to assess long-term effects of conservative treatment. Monitoring by infrared spectroscopy (ATR-FTIR), X-ray diffraction (XRD), and energy dispersive X-ray fluorescence (EDXRF), *Microchemical Journal* 124 (2016) 646-656.

[37] D. Dewi, H. Agusnar, Z. Alfian, and Tamrin, Characterization of technical kaolin using XRF, SEM, XRD, FTIR and its potentials as industrial raw materials, *Journal of Physics: Conference Series* 1116 (2018) 042010.

[38] N. M. Julkapli, and S. Bagheri, Developments in nano-additives for paper industry, *Journal of Wood Science* 62 (2016) 117-130.

[39] D. Aurbach, R. Skaletsky, and Y. Gofer, The Electrochemical Behavior of Calcium Electrodes in a Few Organic Electrolytes, *Journal of The Electrochemical Society* 138 (1991) 12.

[40] M. Wang, C. Jiang, S. Zhang, X. Song, Y. Tang, and H.M. Cheng, Reversible calcium alloying enables a practical room-temperature rechargeable calcium-ion battery with a high discharge voltage, *Nature Chemistry* 10 (2018) 667-672.

[41] W. Zhang, D. Liu, H. Lin, H. Lu, J. Xu, and D. Liu, On the cycling stability of the supercapacitive performance of activated carbon in KOH and H_2SO_4 electrolyte, *Colloids and Surfaces A: Physicochemical and Engineering Aspects* 511 (2016) 294-302.

[42] B. Singh, Y. Fang, B. Cowie, L. Thomsen, NEXAF and XPS characterisation of carbon functional groups of fresh and aged biochars, *Organic Geochemistry* 77 (2014) 1-10.

[43] D. Briggs, and G. Beamson, XPS Studies of the Oxygen 1s and 2s Levels in a Wide Range of Functional Polymers, *Analytical Chemistry* 65 (1993) 1517-1523.

[44] J. McMurry, *Properties of Alcohols and Phenols*, Organic Chemistry Enhanced Edition, Eds. 7 (pp. 602–607), Belmont, 2009.

[45] M. Gu, J. Lee, Y. Kim, J. S. Kim, B. Y. Jang, K. T. Lee, and B. S. Kim, Inhibiting the shuttle effect in lithium–sulfur batteries using a layer-by-layer assembled ion-permselective separator, *RSC Advances* 4 (2014) 46940-46946.

[46] A. Schneider, J. Janek, and T. Brezesinski, Improving the capacity of lithium-sulfur batteries by tailoring the polysulfide absorption efficiency of hierarchical oxygen/nitrogen-functionalized carbon host materials, *Physical Chemistry Chemical Physics* 19 (2017) 8349.

[47] S. Bai, X. Liu, K. Zhu, S. Wu, and H. Zhou, Metal–organic framework-based separator for lithium–sulfur batteries, *Nature Energy* 1 (2016) 16094.

[48] P. Zhu, J. Zhu, J. Zang, C. Chen, Y. Lu, M. Jiang, C. Yan, M. Dirican, R.K. Selvan, and X. Zhang, A novel bi-functional double-layer rGO–PVDF/PVDF composite nanofiber membrane separator with enhanced thermal stability and effective polysulfide inhibition for high-performance lithium–sulfur batteries, *Journal of Materials Chemistry A* 5 (2017) 15096-15104.

[49] J.Q. Huang, Q. Zhang, H.J. Peng, X.Y. Liu, W.Z. Qian, and F. Wei, Ionic shield for polysulfides towards highly-stable lithium–sulfur batteries, *Energy & Environmental Science* 7 (2014) 347.

[50] I. Bauer, S. Thieme, J. Bruckner, H. Althues, and S. Kaskel, Reduced polysulfide shuttle in lithium–sulfur batteries using Nafion-based separators, *Journal of Power Sources* 251 (2014) 417-422.

[51] J. Conder, A. Forner-Cuenca, E.M. Gubler, L. Gubler, P. Novák, and S. Trabesinger, Performance-Enhancing Asymmetric Separator for Lithium–Sulfur Batteries, *ACS Applied Materials & Interfaces* 8 (2016) 18822-18831.

[52] T.Z. Zhuang, J.Q. Huang, H.J. Peng, L.Y. He, X.B. Cheng, C.M. Chen, and Q. Zhang, Rational Integration of Polypropylene/Graphene Oxide/Nafion as Ternary-Layered Separator to Retard the Shuttle of Polysulfides for Lithium–Sulfur Batteries, *Small* 12 (2016) 381-389.

[53] Z. Hao, L. Yuan, Z. Li, J. Liu, J. Xiang, C. Wu, R. Zeng, and Y. Huang, High performance lithium-sulfur batteries with a facile and effective dual functional separator, *Electrochimica Acta* 200 (2016) 197-203.

[54] L. Luo, S.H. Chung, and A. Manthiram, A trifunctional multi-walled carbon nanotubes/polyethylene glycol (MWCNT/PEG)-coated separator through a layer-by-layer coating strategy for high-energy Li–S batteries, *Journal of Materials Chemistry A* 4 (2016) 16805-16811.

[55] Z. Zhang, Z. Zhang, J. Li, and Y. Lai, Polydopamine-coated separator for high-performance lithium-sulfur batteries, *Journal of Solid State Electrochemistry* 19 (2015) 1709-1715.

[56] G. Ma, Z. Wen, J. Jin, M. Wu, X. Wu, and J. Zhang, Enhanced cycle performance of Li–S battery with a polypyrrole functional interlayer, *Journal of Power Sources* 267 (2014) 542-546.

[57] J.H. Kim, J. Seo, J. Choi, D. Shin, M. Carter, Y. Jeon, C. Wang, L. Hu, and U. Paik, Synergistic Ultrathin Functional Polymer-Coated Carbon Nanotube Interlayer for High Performance Lithium–Sulfur Batteries, *ACS Applied Materials & Interfaces* 8 (2016) 20092-20099.

[58] J. Zhu, C. Chen, Y. Lu, J. Zang, M. Jiang, D. Kim, and X. Zhang, Highly porous polyacrylonitrile/graphene oxide membrane separator exhibiting excellent anti-self-discharge feature for high-performance lithium–sulfur batteries, *Carbon* 101 (2016) 272-280.

[59] E. Peled, and S. Menkin, Review-SEI: Past, Present and Future, *Journal of The Electrochemical Society* 164 (2017) A1703-A1719.

[60] Y. X. Lin, Z. Liu, K. Leung, L. Q. Chen, P. Lu, and Y. Qi, Connecting the irreversible capacity loss in Li-ion batteries with the electronic insulating properties of solid electrolyte interphase (SEI) components, *Journal of Power Sources* 309 (2016) 221-230.

[61] Z. F. Deng, Z. A. Zhang, Y. Q. Lai, J. Liu, J. Li, and Y. X. Liu, Electrochemical Impedance Spectroscopy Study of a Lithium/Sulfur Battery: Modeling and Analysis of Capacity Fading, *Journal of The Electrochemical Society* 160 (2013) A553-A558.

[62] R.P. Ramasamy, R.E. White, and B.N. Popov, Calendar life performance of pouch lithium-ion cells, *Journal of Power Sources* 141 (2005) 298-306.

[63] A. Nyman, T. G. Zavalis, R. Elger, M. Behm, and G. Lindbergh, Analysis of the Polarization in a Li-Ion Battery Cell by Numerical Simulations, *Journal of The Electrochemical Society* 157 (2010) A1236-A1246.

[64] B. Huber, L. Rossrucker, J. Sundermeyer, and B. Roling, Ion transport properties of ionic liquid-based polyelectrolytes, *Solid State Ionics* 247-248 (2013) 15-21.

[65] Y. Zhang, J. He, Z. Gao, and X. Li, Converting eggs to flexible, all-solid supercapacitors, *Nano Energy* 65 (2019) 104045.

[66] G. M. Roger, S. Durand-Vidal, O. Bernard, P. Turq, T. M. Perger, and M. Bester-Rogac, Interpretation of Conductivity Results from 5 to 45 °C on Three Micellar Systems below and above the CMC, *The Journal of Physical Chemistry B* 112 (2008) 16529-16538.

Chapter 3. Mechanism Study of Recycled Cellulose Fibers in Li-S Batteries

3.1 Introduction

Decarbonization needs more batteries and sustainable materials [1-3]. Li-ion battery as one of the most successful energy storage devices is reaching its theoretical limit [4-6]. Li-S battery is considered one of the next-generation candidates to substitute Li-ion batteries due to the high theoretical capacity (1675 mAh g^{-1} of sulfur) and energy density (2600 Wh kg^{-1}), as well as the low-cost, high-accessible sulfur [7,8]. However, two major challenges are hindering the practical viability of Li-S batteries: polysulfide shuttle effect and mossy/dendritic Li growth [9,10]. The shuttle effect of polysulfides arises because the small-size polysulfide molecules can freely travel from the cathode side through separators to reach the anode and corrode it, leading to a waste of active materials and poor battery capacity and stability [11,12]. The mossy/dendritic Li growth occurs due to the active Li metal anode and unevenly distributed Li-ions within batteries tending to aggregate at edges and uneven surfaces to form Li whiskers, resulting in a localized short circuit and poor lifespan [13,14].

Scientists have devoted much effort to experimentally resolve these challenges, yet the efficiency remains debatable mostly due to restricted techniques [15,16]. Since both challenges happen within assembled batteries, simulations play a more efficient role in addressing them [17,18]. Wang *et al.* [19] applied a massive number of simulations, including the molecular dynamics (MD) simulation, density functional theory (DFT) calculation, and finite element (FE) simulation, to study the functions of a hydrogen bonding cross-linked multi-functional binder of Lithiated polyacrylic acid-co-vinylphosphonic acid (AA-VPA) and phosphorylated soy protein (P-SPI). They used the DFT simulation to verify that the abundant polar groups within the polymeric network provided strong polysulfide anchoring capacity to inhibit the shuttle effect. Bai *et al.* [20] employed the DFT calculation on metal-organic framework modified electrolyte to evidence its function towards homogeneous Li-ion flux and stable Li plate. These outstanding results show that simulations are excellent at identifying, validating, and expecting the effectiveness of certain materials towards the two challenges. Despite all the

simulation studies on cathodes, anodes, and electrolytes, reports on separators are much overlooked [21,22].

Recently, cellulose fibers (CFs) were used to coat commercial separators and diminished both the polysulfides shuttling and mossy Li growth, leading to a Li-S battery with a lifespan of over 800 cycles and a retention rate of over 70% [23]. CFs are well-known as a green, low-cost, and highly accessible material in nature. Although some DFT simulation has been reported in the paper, more thorough simulations are needed to better understand how CFs work and how much effect the CFs can provide regarding the suppression of the shuttle effect and mossy Li.

Herein, we report a more comprehensive analysis of the CF coating towards polysulfide shuttle effect and dendritic/mossy Li growth using theoretical simulations. The functional groups on CFs are readily to lose H^+ and form a negatively charged surface to mitigate polysulfide shuttling and evenly distribute Li-ions (**Figure 2.1**). MD simulations are used to mimic realistic battery conditions during operation, separately study the functions of CFs towards polysulfides and Li-ions, and compare the results with polypropylene (PP) separators. DFT calculations further unveil the behaviors and energy differences of various species of polysulfides and Li-ions when encountering CFs or PP separators. The findings provide insights on not only the CFs' potential regarding solutions to current challenges that Li-S batteries are facing, but also other similar materials probabilities regarding the challenges, paving the way towards a more practical, stable, and sustainable Li-S battery.

3.2 Methods

3.2.1 CF extraction and coating

A piece of hardboard was cut off from a paper container to be alkaline treated using 5 wt% NaOH solution. The suspension was constantly stirred and then held at 80 ℃ for 3 hours. Sonication and centrifugation using DI water and isopropyl alcohol were applied afterward to wash the CFs and eventually held the CFs in isopropyl alcohol to keep an organic solution condition. Vacuum filtration was applied to coat the CFs onto a piece of a Celgard 2400 separator. The coated separator was then dried at 60 °C for 12 hours. More details could be found in our previous study [23].

3.2.2 Battery assembling, disassembling, and characterization

The dried CF-coated separators were punched into circular pieces for coin cells. The electrolyte was produced by dissolving 1 mol L^{-1} lithium bis(trifluoromethanesulfony)imide (LiTFSI) and 0.4 mol L^{-1} $LiNO_3$ in an organic solvent of dimethoxyethane (DME) + 1,3-dioxolane (DOL) at a 1:1 volume ratio. An activated paper carbon with sulfur (APC/S) was prepared using the same way as our previous study and employed as the electrode [23,24]. The APC/S cathodes, separators, electrolytes, and Li anodes were assembled into coin cells manually. After running for 100 cycles, the batteries were manually disassembled. The Li metal plates were retrieved to be characterized by the scanning electron microscope (SEM) and energy-dispersive X-ray spectroscopy (EDS) (FEI Quanta 650 with EDS detector).

3.2.3 Permeation experiment

Shredded Li metal pieces and sulfur powders with an atomic ratio of 1:3 were added to a beaker filled with electrolytes. The mixture was stirred at a temperature of 60 °C for 48 hours to obtain the Li_2S_6 solution. The solution was separately added into two small glass tubes attached to the lids with 1 mL for each. The glass tubes were then covered separately by an uncoated separator or a CF-coated separator and sealed in two vials filled with electrolyte. The whole experiment was conducted in a glove box filled with Ar.

3.2.4 MD simulation

MD calculations were conducted using the Largescale Atomic/Molecular Massively Parallel Simulator (LAMMPS) [25]. A CF chain model and its net model were built up using ($C_6H_{10}O_5$) as the unit cell. Similarly, a PP chain model and its net model were also built up as references using (C_3H_6) as the unit cell. Polysulfide (Li_2S, Li_2S_2, S_4^{2-}, S_6^{2-}, and S_8^{2-}) models were created and relaxed before use. The calculations were performed using the canonical ensemble (N, V, T), where the temperature was raised to 300 K in 4 ps. For Li-ion related models, the interatomic interactions were described by the reactive force field (ReaxFF) [26]. For polysulfide related models, a different reactive force field (ReaxFF) was used [27]. After the temperature was raised to the target temperature and held for 10 ps, an initial velocity of 0.004 Ang/fs was applied to the Li-ion model or polysulfide model to allow them to travel through the CF or PP chains or nets. For the Li-ion related simulation, a wall was set up at the end of the simulation box to collect the final

positions of all Li ions. For the electric field MD simulation, an electric field of 2 V to resemble the realistic condition was applied.

3.2.5 DFT simulation

The QUANTUMESPRESSO software package was used to perform the density functional theory (DFT) calculations with a norm-conserving pseudopotential and with the SCAN meta-GGA exchange-correlation functional [28,29]. A gamma k-point mesh was used, and the kinetic energy cutoffs for the wave function and charge density were 30 and 300 Ry, respectively. The models were relaxed using the Broyden-Fletcher-Goldfarb-Shanno quasi-Newton algorithm [30].

3.3 Results and Discussion

3.3.1 Li-ion redistribution simulation

A significant observation from experiments (**Figure 3.1**a and b) has shown that the CF-coated separator was able to suppress the corrosion of Li plates and the growth of dendritic/mossy Li. Specifically, with assistance from the CF coating, the Li anode in the CF-enabled battery (**Figure 3.1**a) revealed a flatter surface with a higher thickness after 100 cycles compared with the Li anode in the non-CF battery (**Figure 3.1**b). To explain the experimental observation, an MD model (**Figure 3.1**c) was designed with four cellulose chains to mimic CF-coated separators and three lines of Li-ions between each two successive chains. For comparison, another similar MD model was set up using PP chains (**Figure 3.2**a). After reaching room temperature in the MD simulation, an initial velocity was applied to the Li-ions and allowed them to travel through the cellulose or PP fence until reaching the end of the simulation box. The processes were recorded and the final patterns on the back of the box were collected. The Li-ions were redirected when they traveled through the cellulose fence, whereas they remained on almost the same tracks when they traveled through the PP fence. The final patterns can reflect the results, where the pattern after the CF fence (**Figure 3.1**d) was more random than the pattern after the PP fence (**Figure 3.1**e). More specifically, the Li ions' positions after the CF fence were usually far from their original positions whereas the Li ion's positions after the PP fence were just a few angstroms from their original positions. The neighbor maps (**Figure 3.2**b and c) of the center ions can also result in the same conclusion. To simulate a more realistic scenario of Li-ion passing through a CF-coated separator, a double-fence model with both

the CF fence and PP fence was designed (**Figure 3.2**d). A higher initial velocity was given to the Li-ions such that they could have sufficient kinetic energy to pass through both fences. The Li-ion patterns before the simulation, after the CF fence, and after both the CF and PP fences were recorded (**Figure 3.2**e). After the CF fence, most of the Li-ions were redirected. Whereas, after the PP fence, only four Li-ions (Li-ion 2, 6, 9, 12) that were very close to the PP chains were further redirected. This reveals that coating CFs on PP can further enhance the randomness of Li-ions after they travel through the separator. All these results demonstrated that CFs have much stronger interactions towards Li-ions, which redistributed the Li-ions and, as observed in experiments, resulted in a more even surface and slower Li consumption, eventually leading to a smaller chance of mossy/dendritic Li growth. This result can be reflected in section 3.3, where the interaction energy between Li ions and CFs is much higher than that between Li ions and PP. To study the interaction between the CFs and Li-ions, a DFT simulation was carried out. The result (**Figure 3.1**f) showed that an attraction force was endowed to the cellulose chain towards Li-ions and that provided the redirection phenomenon when Li-ions passed through the cellulose fence, which is in agreement with the description in the paper [23]. The significant attraction behavior could explain the largely random redistribution in the MD simulation. In comparison, the DFT simulation using Li-ions and PP chains was also set up (**Figure 3.2**f). A tiny repulsion was observed during the simulation, opposite to the result of cellulose and Li-ions. This tiny repulsion could evidence the small changes in Li-ion traveling tracks in the MD simulation.

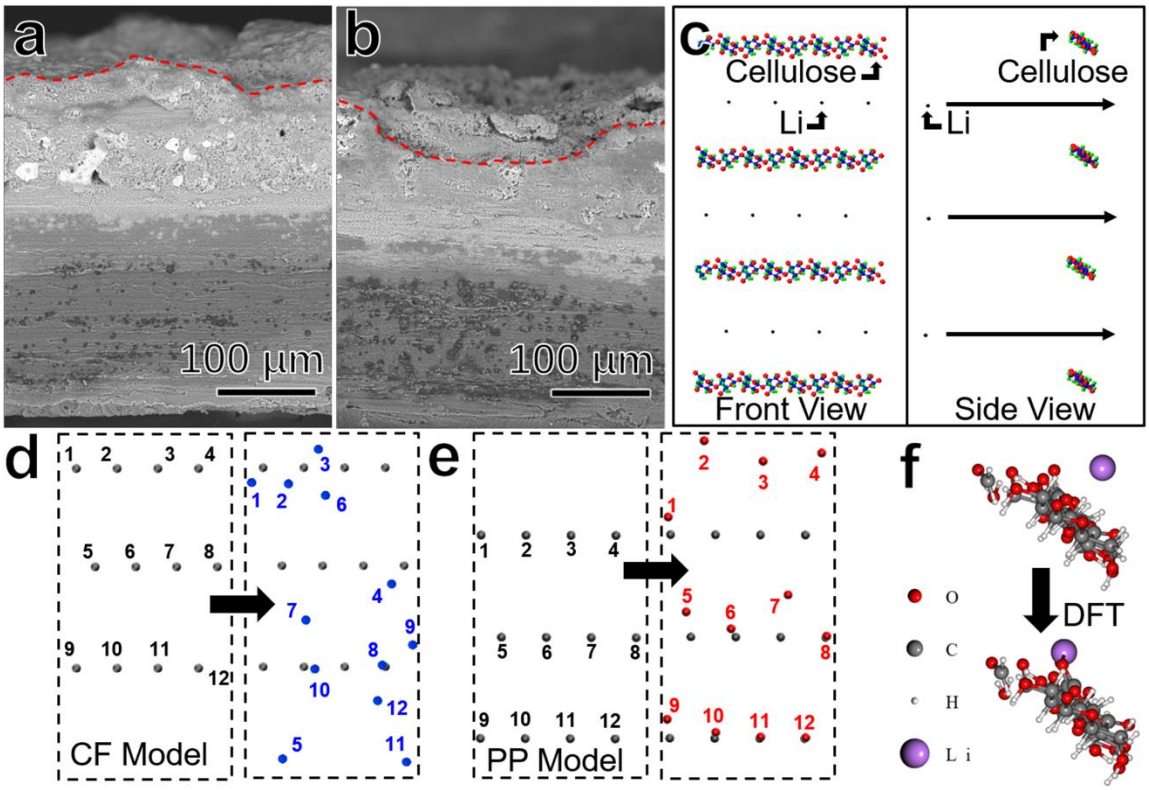

Figure 3.1. (a) SEM image of the Li anode edge in CF-enabled battery after 100 cycles. (b) SEM image of the Li anode edge in non-CF battery after 100 cycles. (c) MD model for Li-ion traveling simulation using cellulose chains. (d) MD result of Li-ion traveling simulation using cellulose chains. (e) MD result of Li-ion traveling simulation using PP chains. (f) DFT result of interactions between a cellulose chain and a Li ion.

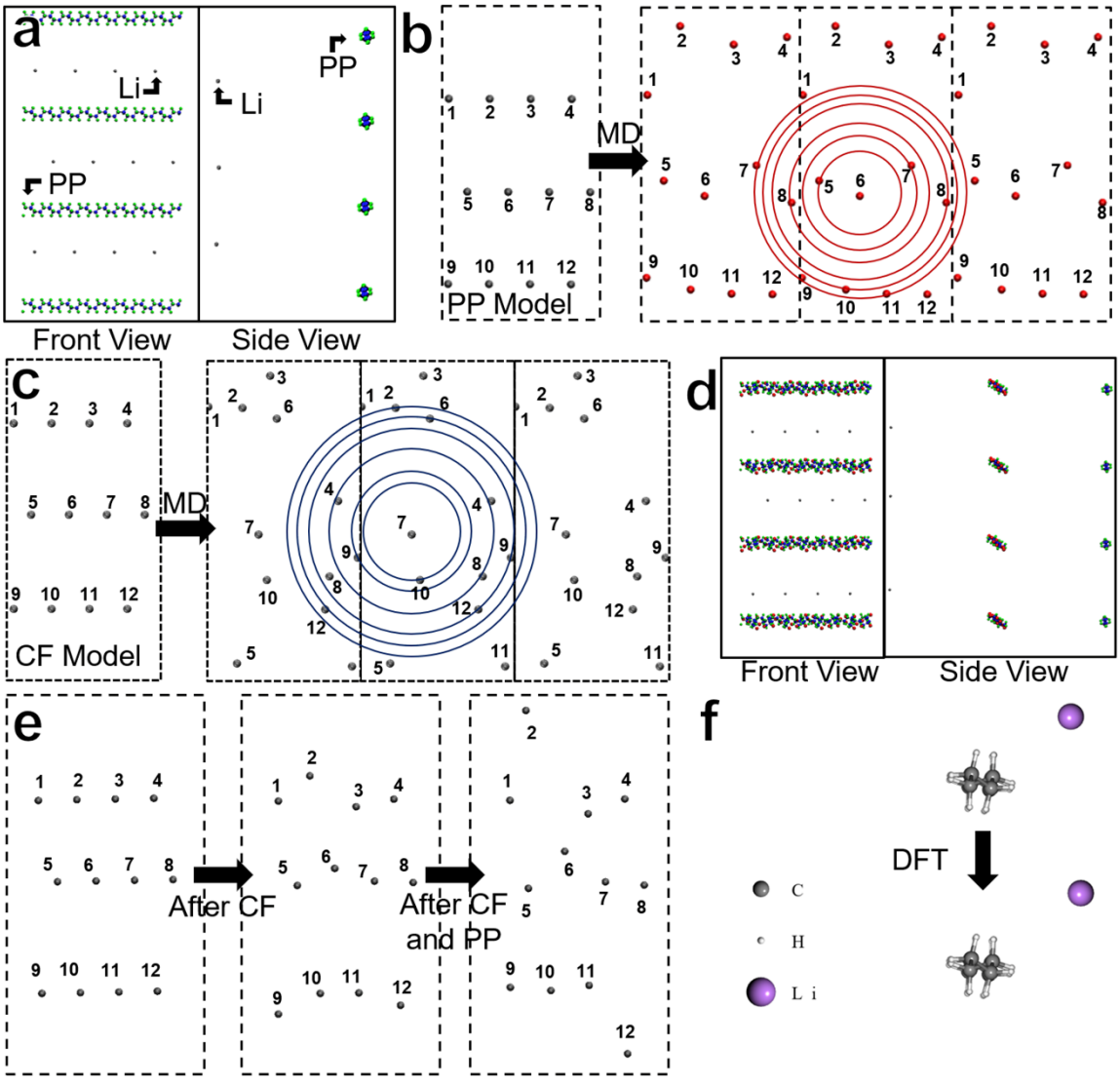

Figure 3.2. (a) MD model for Li-ion traveling simulation using PP chains. (b) Neighbor map for the MD result of the PP model. (c) Neighbor map for the MD result of the CF model. (d) MD model for Li-ion traveling simulation using both CF and PP chains. (e) MD result of Li-ion traveling simulation using both CF and PP chains. (f) DFT result of interactions between a PP chain and a Li ion.

3.3.2 Polysulfide MD simulation

To evaluate a product using in a Li-S battery, the suppression towards polysulfide shuttling is another critical feature. From the experimental observation using EDS, more fluorine (from the electrolyte) and less sulfur (from polysulfides) were found in the Li anode in the CF-enabled battery (**Figure 3.3**a) than that in the non-CF battery (**Figure 3.3**c) after 100 cycles, indicating that a large number of polysulfides were blocked by the CF

coating layer. Because of that, less lithium was corroded in the CF-enabled battery, providing the battery with a safer working condition and a much longer lifespan. To closely study what happened when polysulfides travel through the separators, similar MD models were constructed for both cellulose (**Figure 3.3**b) and PP (**Figure 3.3**d), where polysulfide models were used to replace the Li-ions in the Li-ion traveling simulation models. Multiple polysulfide species were investigated including S_4^{2-}, S_6^{2-}, and S_8^{2-}. Similarly, an initial velocity (0.004 Ang fs^{-1}) was given to the polysulfides and allowed them to travel through the cellulose or PP fence. The average velocities of different species were recorded before arriving at the fences (**Figure 3.3**e). Due to interactions between the cellulose chains and the polysulfides, the velocities of the polysulfides reduced when approaching the cellulose fence while they remain almost unchanged when approaching the PP fence. This conclusion was evidenced by a published work, where a permeation experiment showed that the polysulfides permeated faster through the uncoated separator than the CF-coated separator [23].

To study the effectiveness of the CF coating, a new CF model, named CF net model, was built with a pore in the middle, together with a similar model using PP (**Figure 3.3**f). These models in a periodic simulation box were first relaxed to be stable before use. Unlike the fence models that focused mainly on chemical interactions between the fence materials and the polysulfides, the more realistic net models imitated the real porous separator structure and considered both physical and chemical interactions. Before the simulation, nine S_8^{2-} as examples were placed at the left side of the cellulose model (**Figure 3.3**g) or the PP model (**Figure 3.3**i) ready to be activated with an initial velocity. As a result, all nine S_8^{2-} were blocked by the cellulose fence (**Figure 3.3**h), and three of the nine S_8^{2-} passed through the PP fence (**Figure 3.3**j). Another example with twelve S_8^{2-} also exhibited the similar result, where all twelve S_8^{2-} were blocked by the cellulose fence (**Figure 3.4**a and b), and four of the twelve S_8^{2-} passed through the PP fence (**Figure 3.4**c and d, supporting information). To quantify the effectiveness, a typical energy density equation for Li-S battery is used as follows [31],

$$E_d = \frac{V \cdot m_A \cdot C}{\sum W_i} \tag{3.1}$$

where E_d is the specific energy density (Wh kg^{-1}), V is the average working voltage (V), m_A is the active material loading (mg cm^{-2}), C is the specific capacity (mAh g^{-1}), and W_i is the weight of each component within the battery (mg cm^{-2}). The effectiveness can be quantified as the percentage contribution to the specific energy density of a battery. Usually, the average working voltage can be treated the same for all Li-S batteries. The changeable terms for different batteries are m_A, C, and W_i. Here, we combine both experimental and simulation results to be plugged into the equation. The m_A in the equation can be considered the effective sulfur, and only the sulfur that remained at the left side of the fence in the simulation can be effectively reacted, meaning that 100.00% sulfur was active for the CF simulation case, and only 66.67% sulfur was active for the PP simulation case. The C and the W_i terms were obtained from the previously reported experimental observation, where C for the CF-enabled battery was 718.23 mAh g^{-1} and for the non-CF battery was 726.34 mAh g^{-1}, and the CF-enabled battery had a 0.56 mg cm^{-2} extra W_i comparing with the non-CF battery [23]. The calculation result is normalized and shown in **Figure 3.3**k, where the effectiveness of the CF is around 32% higher than that of the PP. This result indicated that coating the CF layer on the separator is significantly effective to address the polysulfide shuttling even with extra weight and slightly lower capacity.

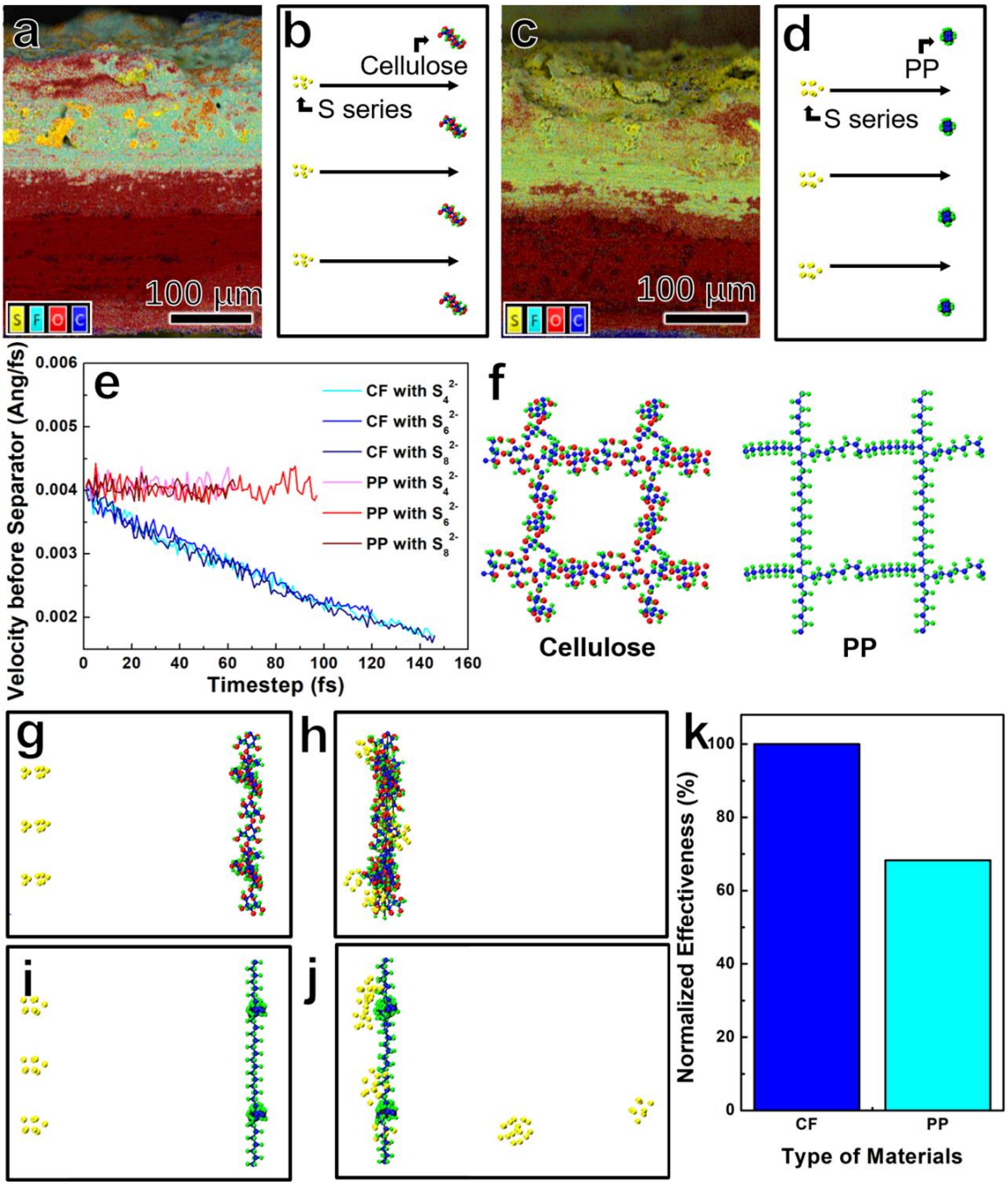

Figure 3.3. (a) EDS image of the Li anode in the CF-enabled battery. (b) MD model for CF chains with polysulfides. (c) EDS image of the Li anode in the non-CF battery. (d) MD model for PP chains with polysulfides. (e) Velocity changes of different polysulfide species before arriving the CF or PP chains. (f) MD net models of the CF and PP with pores in the middle. (g) Initial status of the MD simulation for polysulfides traveling through the CF net fence. (h) Final status of the MD simulation for polysulfides traveling through the CF net fence. (i) Initial status of the MD simulation for polysulfides traveling through the PP net fence. (j) Final status of the MD simulation

for polysulfides traveling through the PP net fence. (k) Normalized calculation result for the effectiveness of CF and PP.

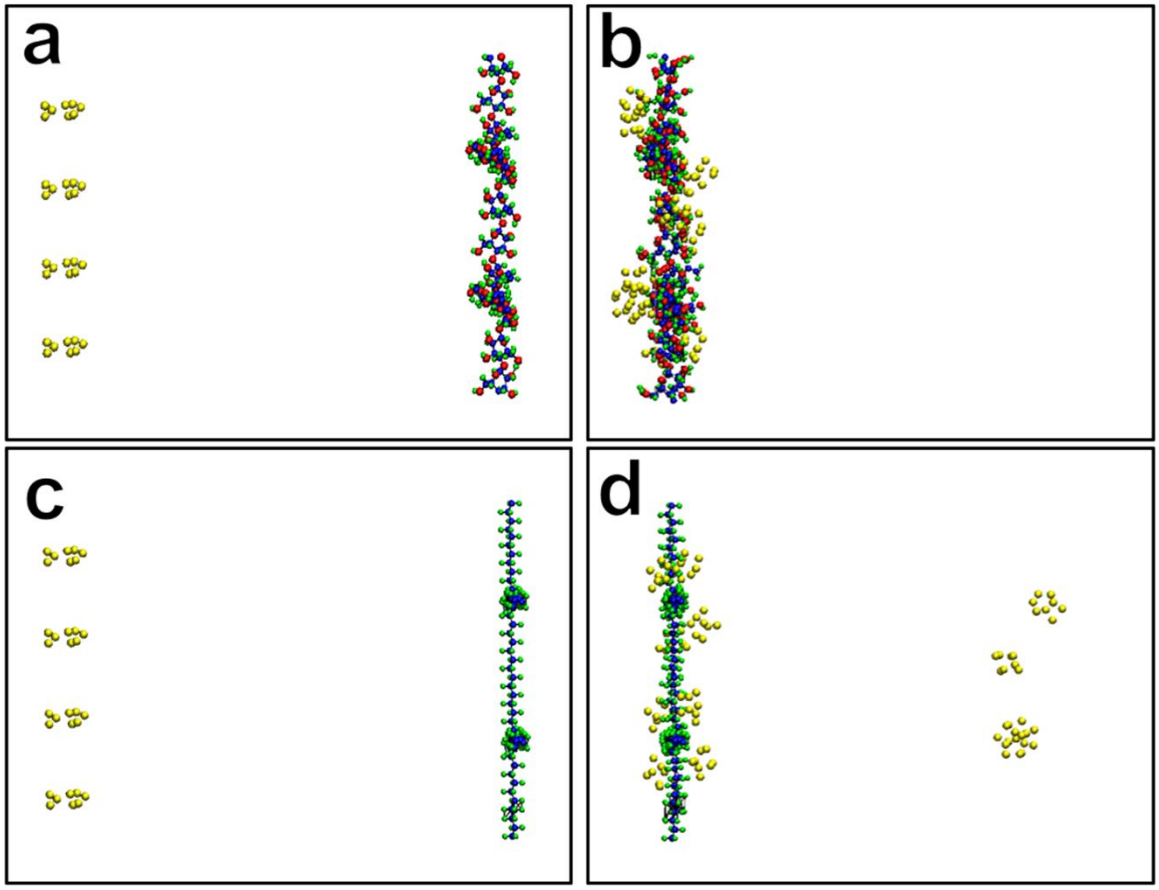

Figure 3.4. (a) Initial status of the MD simulation for twelve polysulfides traveling through the CF net fence. (b) Final status of the MD simulation for twelve polysulfides traveling through the CF net fence. (c) Initial status of the MD simulation for twelve polysulfides traveling through the PP net fence. (d) Final status of the MD simulation for twelve polysulfides traveling through the PP net fence.

3.3.3 Mechanism discussion

Density functional theory (DFT) calculations were used to validate the repelling mechanism of the CF functional groups. The S_8^{2-} and S_6^{2-} chain model was built and placed in the front of the $-COO^-$ (**Figure 3.5**a and c) group and $-C-O^-$ (**Figure 3.5**b and d) group models which were connected to fixed benzene models. All models were relaxed separately before calculation to ensure accuracy. The DFT simulations demonstrate that both carboxylic and phenolic groups without H^+ repel the S_8^{2-} and S_6^{2-} chains to achieve lower total energy. Figure 3a shows that the distances between atom 1 (the oxygen) and atom 2

(the nearest sulfur), and atom 1 and atom 3 (the second nearest sulfur) increased from 2.011 Å to 2.976 Å, and 2.191 Å to 2.207 Å, respectively. While the distances, in Figure 3b, between atom 1 (the oxygen) and atom 2 (the nearest sulfur), and atom 1 and atom 3 (the second nearest sulfur) increased from 2.070 Å to 2.861 Å, and 2.343 Å to 2.736 Å, respectively. Similar results regarding the functional groups repelling S_6^{2-} can be also observed. **Figure 3.5**c reveals that the distances between atom 1 (the oxygen) and atom 3 (the nearest sulfur), and atom 1 and atom 2 (the second nearest sulfur) increased from 2.363 Å to 2.591 Å, and 2.706 Å to 2.802 Å, respectively. Moreover, the distances, in **Figure 3.5**d, between atom 1 (the oxygen) and atom 2 (the nearest sulfur), and atom 1 and atom 3 (the second nearest sulfur) increased from 2.223 Å to 2.751 Å, and 2.939 Å to 2.962 Å, respectively. To visualize the repelling mechanism, a comparison between polysulfides (mostly Li_2S_6) permeated through an uncoated separator or a CF-coated separator was exhibited with time (**Figure 3.5**e). The result showed that the polysulfides permeated faster through the uncoated separator than the CF-coated separator, indicating that the CF-coated separator partially repelled the polysulfides. Both the DFT calculations and permeation experiment demonstrate that the functional groups enable the polysulfide-ion repelling mechanism, which mitigates the shuttle effect without consuming active materials.

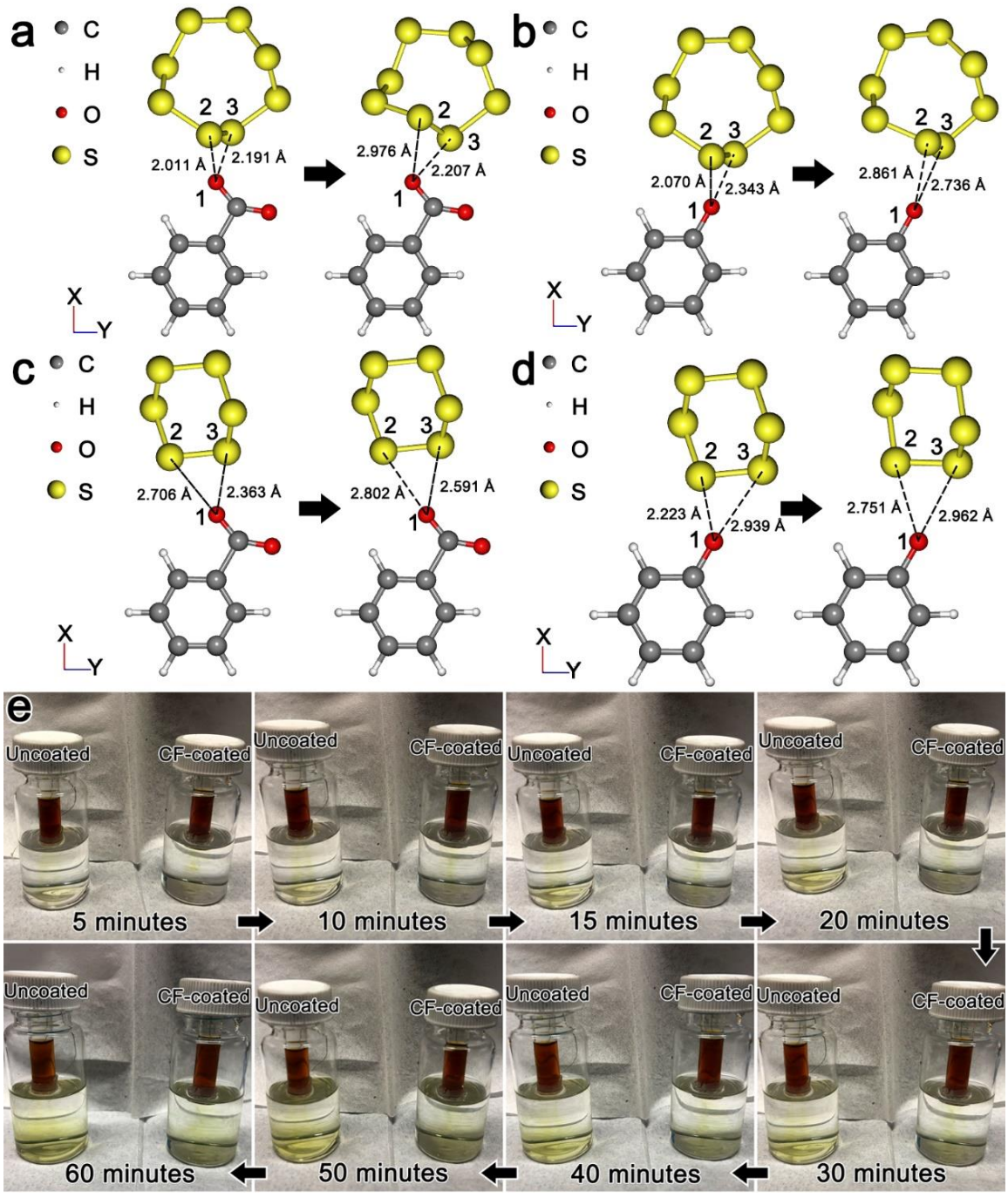

Figure 3.5. (a) DFT simulation of the carboxylic group on S_8^{2-} polysulfides. (b) DFT simulation of the phenolic group on S_8^{2-} polysulfides. (c) DFT simulation of the carboxylic group on S_6^{2-} polysulfides. (d) DFT simulation of the phenolic group on S_6^{2-} polysulfides. (e) Permeation experiment between the uncoated separator and CF-coated separator after 5 minutes, 10 minutes, 15 minutes, 20 minutes, 30 minutes, 40 minutes, 50 minutes, and 60 minutes.

To understand the mechanisms behind all phenomena observed in the experiments and MD simulations, a series of DFT simulations were carried out. Prior to that, an MD simulation to reveal the status of the CF within batteries during operation is set up for ensuring the accuracy of the DFT. An electric field was applied to the CF net model using MD and the result (**Figure 3.7**a) showed that some H^+ would be easily released from the CF. Meanwhile, many H^+ would move to one side, leaving the other side more negatively charged. A charge map (**Figure 3.6**) of the CF after the introduction of electric field was plotted to better visualize the charge difference, which revealed that most positively charged atoms (blue dots) gathered at the right side of the CF and most negatively charged atoms (red dots) remained at the left side of the CF, rendering the left surface negatively charged. Compared with that, the electric field was not able to remove H^+ from the PP net, nor move H^+ to one side of the PP net (**Figure 3.8**a). Therefore, the DFT study regarding the interactions between the cellulose and sulfides was proceeded with some H^+ being removed. Each model has been separately relaxed before the DFT simulation. The DFT simulation of Li_2S_2 and Li_2S with H-removed cellulose (HCF) (**Figure 3.7**b) showed that the HCF was able to repel the sulfur atoms yet attract Li atoms to some degree. The attraction of the Li sites was mainly caused by the loss of H^+ generating a negatively charged surface on the HCF, where the local uneven charges slightly polarized the Li_2S_x (x= 1 or 2) species and eventually generated a small attraction force to the Li_2S_x (x= 1 or 2) species at the Li sites. As known in the previous paper, there are also functional groups on the CFs, especially the C-OH group and -COOH group, which also lose their H^+ during battery operation [23, 32]. Hence, when performing DFT simulation in this study, O^- was also added to represent the functional groups (C-OH) after losing the H^+. With functional groups on the CF (OCF) (**Figure 3.7**c), the repulsion to the sulfur could no longer counteract the attraction to the Li caused by the same reason as HCF, leading to connections between the OCF and the Li_2S_2 or Li_2S. These phenomena could largely decrease the possibility of losing active materials (Li_2S_2 and Li_2S) by repelling or even anchoring them at the cathode side and preventing them from traveling through the separators to touch the anodes and be inactivated, especially if the active materials have already detached from the cathodes due to battery operation. The attraction between the HCF and the Li ions was also observed in the previous section (**Figure 3.1**f). For comparison, the DFT simulation

regarding PP chains and the sulfides was also performed (**Figure 3.8**b). Compared with the DFT of the CFs and sulfides, a small repulsion was detected for both Li_2S_2 and Li_2S with PP, which can also keep a small number of active materials at the cathode side. However, if the active materials have already traveled through the separator as polysulfides, they could hardly come back to the cathode side since PP had evenly distributed H^+ at the surface and the tiny repulsion was the same when facing the anode side.

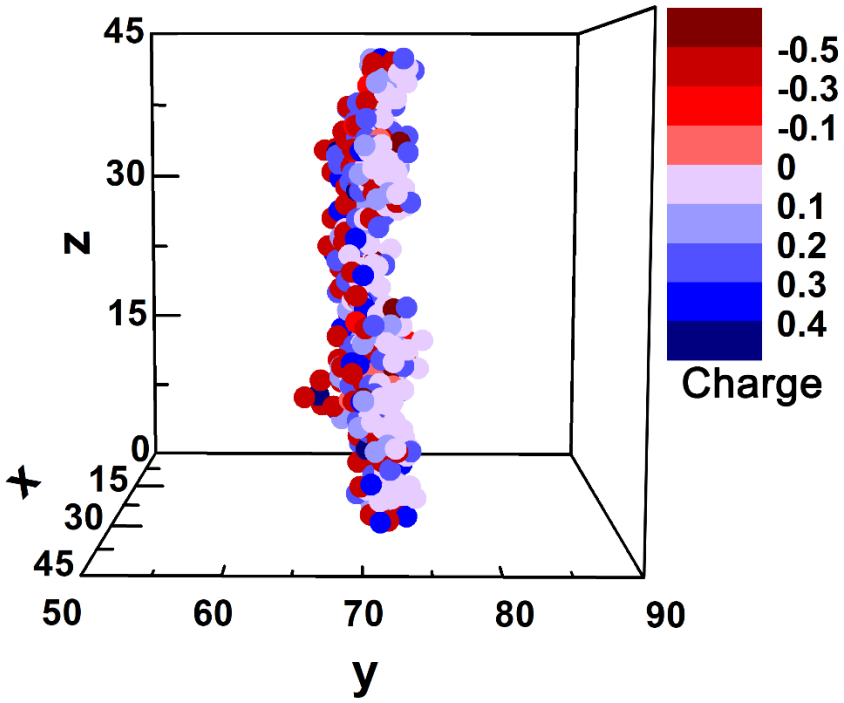

Figure 3.6. Charge map of the CF after the electric field.

Apart from the low-order polysulfides, S_4^{2-}, S_6^{2-}, and S_8^{2-} were also studied with HCF (**Figure 3.7**d) and OCF (**Figure 3.7**e) using DFT, as well as the PP as reference (**Figure 3.8**c). For polysulfides with HCF simulation, it is worth noting that the smaller the polysulfides were, the stronger the repulsion was. More specifically, after simulation, the S_4^{2-} was repelled by 0.861 Ang, the S_6^{2-} was repelled by 0.694 Ang, and the S_8^{2-} was repelled by 0.170 Ang. This trend was not applied to the OCF cases as the repulsion was larger when functional groups were added and the repulsion was location dependent based on the location of the functional groups. For instance, S_8^{2-} was repelled by 0.588 Ang by the OCF, which is much farther than that of the HCF. S_6^{2-} was also repelled by 1.732 Ang, larger than that of the HCF. For S_4^{2-}, the repelling distance was smaller than that of the HCF, most likely because the location of the added functional group is already a bit far

from the S_4^{2-}. In addition, compared with the DFT simulation using PP towards polysulfides, it can be clearly revealed that the interactions between PP and polysulfides were much smaller. This conclusion can also be proved by the energy difference of the DFT simulations (**Figure 3.7**f). It was calculated by

$$E_d = E_{Combine} - E_{CF} - E_S \tag{3.2}$$

where E_d is the energy difference, $E_{Combine}$ is the energy after DFT simulation, E_{CF} is the energy of the separator material (HCF, OCF, and PP), and E_S is the energy of the polysulfides or Li. As shown, prior to the calculation, the energy of each component was separately measured to be E_{CF} and E_S. After the simulation, the resultant combining energy of the system was measured to be $E_{Combine}$ to calculate the E_d. This can be used to represent the effectiveness of the interactions between the CF or PP and polysulfides or Li. It could be concluded that the interactions between CFs and polysulfides were larger than the interactions between PP and polysulfides. The more obvious difference could be obtained from the interactions between CFs or PP and Li discussed in the previous section 3.3.1, which was the reason that CFs could effectively redistribute the Li-ions whereas PP could only slightly redirect the Li-ions.

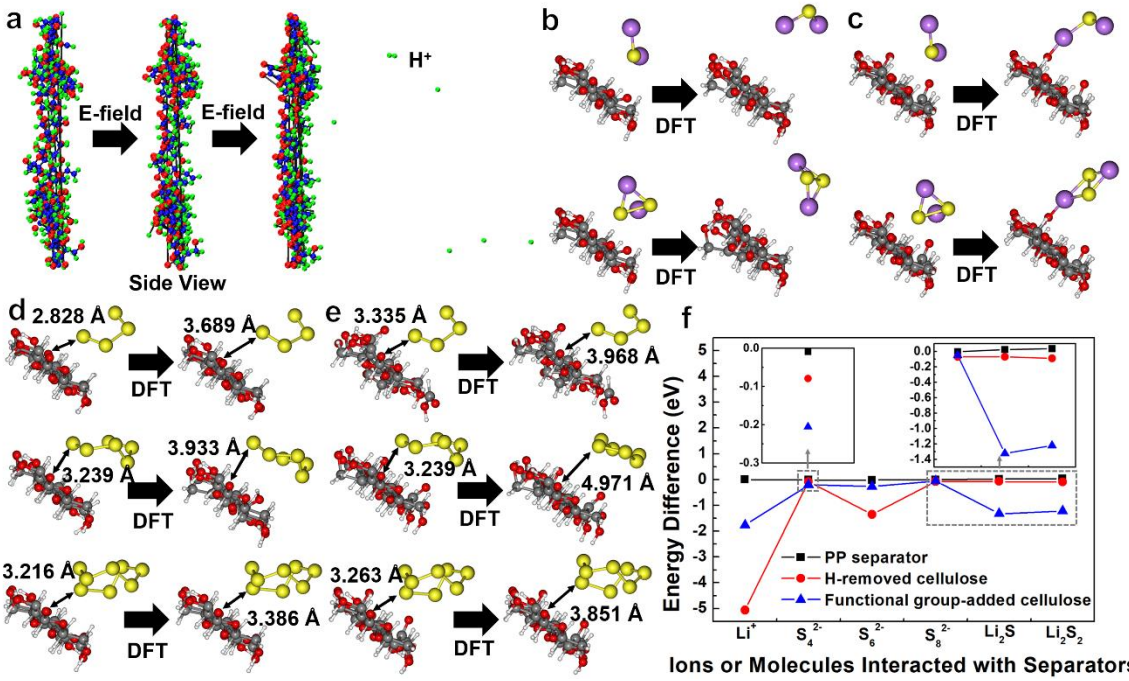

Figure 3.7. (a) MD simulation result for CF losing H^+ under electric field. (b) DFT simulation results of the interactions between HCFs and $Li2S_n$ ($n \leq 2$). (c) DFT simulation results of the

interactions between OCFs and $Li2S_n$ ($n \leq 2$). (d) DFT simulation results of the interactions between HCFs and S_n^{2-} ($n \geq 4$). (e) DFT simulation results of the interactions between OCFs and S_n^{2-} ($n \geq 4$). (f) Energy difference from DFT simulations of CFs (or PP) and polysulfides (or Li).

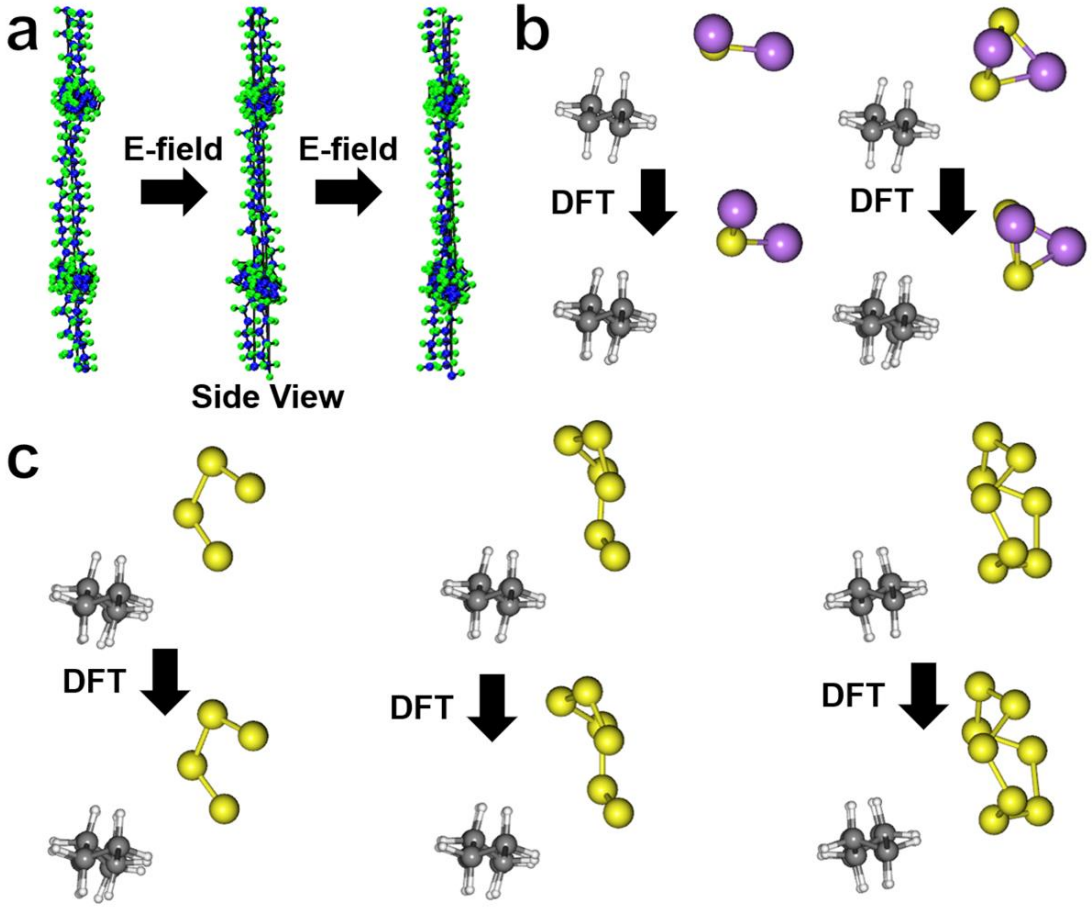

Figure 3.8. (a) MD simulation result for PP under electric field. (b) DFT simulation results of the interactions between PP and $Li2S_n$ ($n \leq 2$). (c) DFT simulation results of the interactions between PP and S_n^{2-} ($n \geq 4$).

3.4 Conclusions

Li-S battery has been considered a promising candidate to substitute Li-ion battery. Yet the practical application has been hindered by multiple challenges including the polysulfide shuttle effect and dendritic Li growth. Cellulose fiber has been proven to be an effective material to suppress both challenges. However, the theoretical reasons behind the phenomenon have not been thoroughly studied. Here, MD and DFT simulations were carried out in this study to more efficiently investigate the working mechanisms of CFs in Li-S batteries. It was proven that the CFs were readily to lose their H^+ when the battery is

in operation, leading to a negatively charged surface towards polysulfides. This surface has been evidenced to have the ability to effectively repel polysulfides and redirect Li ions, enabling suppression of both the shuttle effect and dendritic Li growth. In addition, the functional groups on the cellulose fiber are able to anchor solid Li_2S_n ($n \leq 2$) species to prevent additional loss of active materials. The findings not only proved the effectiveness of using cellulose fibers, but also provided the potential of materials that create repelling mechanisms to control the current challenges in Li-S batteries, paving the way towards low-cost, high-performance, and environmentally friendly Li-S batteries.

Reference

[1] X. Zhang, L. Hou, A. Ciesielski, and Paolo Samori, 2D Materials Beyond Graphene for High-Performance Energy Storage Applications, *Advanced Energy Materials* 6 (2016) 1600671.

[2] D.S. Su, and R. Schlogl, Nanostructured Carbon and Carbon Nanocomposites for Electrochemical Energy Storage Applications, *ChemSusChem* 3 (2010) 136-168.

[3] J.B. Goodenough, Electrochemical energy storage in a sustainable modern society, *Energy & Environmental Science* 7 (2014) 14-18.

[4] M. Li, J. Lu, Z. Chen, and K. Amine, 30 Years of Lithium-Ion Batteries, *Advanced Materials* 30 (2018) 1800561.

[5] N. Nitta, F. Wu, J.T. Lee, and G. Yushin, Li-ion battery materials: present and future, *Materials Today* 18 (2015) 252-264.

[6] A. Fotouhi, D.J. Anger, K. Propp, S. Longo, and M. Wild, A review on electric vehicle battery modelling: From Lithium-ion toward Lithium–Sulphur, *Renewable and Sustainable Energy Reviews* 56 (2016) 1008-1021.

[7] M. Barghamadi, A. Kapoor, and C. Wen, A Review on Li-S Batteries as a High Efficiency Rechargeable Lithium Battery, *Journal of The Electrochemical Society* 160 (2013) A1256.

[8] R. Kumar, J. Liu, J.Y. Hwang, and Y.K. Sun, Recent research trends in Li–S batteries, *Journal of Materials Chemistry A* 6 (2018) 11582-11605.

[9] S. Li, W. Zhang, J. Zheng, M. Lv, H. Song, and L. Du, Inhibition of Polysulfide Shuttles in Li–S Batteries: Modified Separators and Solid-State Electrolytes, *Advanced Energy Materials* 11 (2021) 2000779.

[10] S. Xia, X. Zhang, C. Liang, Y. Yu, and W. Liu, Stabilized lithium metal anode by an efficient coating for high-performance Li–S batteries, *Energy Storage Materials* 24 (2020) 329-335.

[11] W. Ren, W. Ma, S. Zhang, and B. Tang, Recent advances in shuttle effect inhibition for lithium sulfur batteries, *Energy Storage Materials* 23 (2019) 707-732.

[12] A.F. Hofmann, D.N. Fronczek, and W.G. Bessler, Mechanistic modeling of polysulfide shuttle and capacity loss in lithium–sulfur batteries, *Journal of Power Sources* 259 (2014) 300-310.

[13] D. Cao, X. Sun, Q. Li, A. Natan, P. Xiang, and H. Zhu, Lithium Dendrite in All-Solid-State Batteries: Growth Mechanisms, Suppression Strategies, and Characterizations, *Matter* 3 (2020) 57-94.

[14] Y. Zhang, F.M. Heim, N. Song, J.L. Bartlett, and X. Li, New Insights into Mossy Li Induced Anode Degradation and Its Formation Mechanism in Li–S Batteries, *ACS Energy Letters* 2 (2017) 2696-2705.

[15] Y. Cui, X. Wu, J. Wu, J. Zeng, A.P. Baker, F. Lu, X. Liang, J. Ouyang, J. Huang, X. Liu, Z. Li, and X. Zhang, An interlayer with architecture that limits polysulfides shuttle to give a stable performance Li-S battery, *Energy Storage Materials* 9 (2017) 1-10.

[16] Q. Jin, X. Zhang, H. Gao, L. Li, and Z. Zhang, Novel Li_xSiS_y/Nafion as an artificial SEI film to enable dendrite-free Li metal anodes and high stability Li–S batteries, *Journal of Materials Chemistry A* 8 (2020) 8979-8988.

[17] W. Zhao, L.C. Xu, R. Li, Y. Guo, Z. Yang, R. Liu, and X. Li, Enhance the anchoring and catalytic performance of lithium-sulfur batteries for lithium polysulfide by predicted TiS2 monolayer, *Materials Today Communications* 30 (2022) 103196.

[18] Y. Sun, T. Yang, H. Ji, J. Zhou, Z. Wang, T. Qian, and C. Yan, Boosting the Optimization of Lithium Metal Batteries by Molecular Dynamics Simulations: A Perspective, *Advanced Energy Materials* 10 (2020) 2002373.

[19] H. Wang, G. Zhang, Y. Chen, P. Zheng, H. Yi, Y. Deng, Y. Yang, C. Wang, Reversible cross-linked phosphorylate binder for recyclable lithium-sulfur batteries, *Chemical Engineering Journal* 452 (2023) 139128.

[20] S. Bai, Y. Sun, J. Yi, Y. He, Y. Qiao, H. Zhou, High-Power Li-Metal Anode Enabled by Metal-Organic Framework Modified Electrolyte, *Joule* 2 (2018) 2117-2132.

[21] J. Zhu, E. Yildirim, K. Aly, J. Shem, C. Chen, Y. Lu, M. Jiang, D. Kim, A.E. Tonelli, M.A. Pasquinelli, P.D. Bradford, and X. Zhang, Hierarchical multi-component nanofiber separators for lithium polysulfide capture in lithium–sulfur batteries: an experimental and molecular modeling study, *Journal of Materials Chemistry A* 4 (2016) 13572-13581.

[22] J. Cui, Z. Li, J. Li, S. Li, J. Liu, M. Shao, and M. Wei, An atomic-confined-space separator for high performance lithium–sulfur batteries, *Journal of Materials Chemistry A* 8 (2020) 1896-1903.

[23] Y. Zhou, Y. Zhang, and X. Li, Upcycling of paper waste for high-performance lithium-sulfur batteries, *Materials Today Energy* 19 (2021) 100591.

[24] Y. Zhang, Z. Gao, and X. Li, Capillarity composited recycled paper/graphene scaffold for lithium–sulfur batteries with enhanced capacity and extended lifespan, *Small* 13 (2017) 1701927.

[25] S. Plimpton, Fast Parallel Algorithms for Short-Range Molecular Dynamics, *Journal of Computational Physics* 117 (1995) 1-19.

[26] K. Ganeshan, Y. K. Shin, N. C. Osti, Y. Sun, K. Prenger, M. Naguib, M. Tyagi, E. Mamontov, D. Jiang, A. C. T. Duin, Structure and Dynamics of Aqueous Electrolytes Confined in 2D-TiO_2/$Ti_3C_2T_2$ MXene Heterostructures, *ACS Applied Materials & Interfaces* 12 (2020) 58378-58389.

[27] B. Zhang, A.C.T. van Duin, and J.K. Johnson, Development of a ReaxFF Reactive Force Field for Tetrabutylphosphonium Glycinate/CO_2 Mixtures, *The Journal of Physical Chemistry B* 118 (2014) 12008-12016.

[28] P. Giannozzi, S. Baroni, N. Bonini, M. Calandra, R. Car, C. Cavazzoni, D. Ceresoli, G. L. Chiarotti, M. Cococcioni, I. Dabo, A. Dal Corso, S. De Gironcoli, S. Fabris, G. Fratesi, R. Gebauer, U. Gerstmann, C. Gougoussis, A. Kokalj, M. Lazzeri, L. Martin-Samos, N. Marzari, F. Mauri, R. Mazzarello, S. Paolini, A. Pasquarello, L. Paulatto, C.

Sbraccia, S. Scandolo, G. Sclauzero, A. P. Seitsonen, A. Smogunov, P. Umari, and R. M. Wentzcovitch, Quantum Espresso: a Modular and Open-Source Software Project for Quantum Simulations of Materials, *Journal of Physics: Condensed Matter* 21 (2009) 395502.

[29] Y. Yao and Y. Kanai, Plane-Wave Pseudopotential Implementation and Performance of SCAN Meta-GGA Exchange-Correlation Functional for Extended Systems, *The Journal of Chemical Physics* 146 (2017) 224105.

[30] B. G. Pfrommer, M. Cote, S. G. Louie, and M. L. Cohen, Relaxation of Crystals with the Quasi-Newton Method, *Journal of Computational Physics* 131 (1997) 233-240.

[31] M. Agostini, J.Y. Hwang, H.M. Kim, P. Bruni, S. Brutti, F. Croce, A. Matic, and Y.K. Sun, Minimizing the Electrolyte Volume in Li–S Batteries: A Step Forward to High Gravimetric Energy Density, *Advanced Energy Materials* 8 (2018) 1801560.

[32] X. Yu, J. Joseph, and A. Manthiram, Suppression of the polysulfide-shuttle behavior in Li–S batteries through the development of a facile functional group on the polypropylene separator, *Materials Horizons* 3 (2016) 314-319.

Chapter 4. Use of Recycled Cellulose Fibers for Carbon Dioxide Adsorption

4.1 Introduction

The intensifying greenhouse effect around the world is inducing severe climate change and other environmental issues, which are attracting increasing attention [1-3]. Carbon dioxide (CO_2) gas, a type of greenhouse gas (GHG), as one of the necessary components in nature is also the major cause of the challenge [4]. Replacing fossil fuels with clean energy can largely ease the challenge, which, however, can hardly be achieved in the short term [5]. Therefore, a short-term/medium-term solution to trap CO_2 and accomplish carbon neutrality is of high interest and demand.

Many CO_2 adsorption/absorption methods and technologies have been explored, such as physical adsorption, chemical absorption, and physical separation [6-8]. Among all methods, physical adsorption is considered the most viable method because of its green nature, high CO_2 adsorption capacity, high accessibility, simple operation process, and low cost [5]. A large number of materials have been widely studied to fulfill this function. As the representatives, zeolite, activated carbon (AC), and their derivatives are the most commonly seen CO_2 adsorbers. Georgieva *et al.* [9] exhibited the Merlinoite zeolite (MER) with Na, K, and Cs forms for CO_2 uptake, among which K-MER revealed good capacity of CO_2 (3.5 mmol/g at 1 bar and 298 K), rapid adsorption and desorption kinetics, and promising CO_2/CH_4 separation. Rehman *et al.* [10] reported a series of alkali-activated microporous carbon materials with a high specific surface area and large micropore volume in the sub-nanometer range, which achieved 6.85 mmol/g of CO_2 adsorption capacity at 1 bar and 273 K attributed to well-defined micropores. These studies show a promising future of physical adsorption towards GHG control.

Despite the fact that zeolite and AC are both cost-effective and highly accessible, cellulose fiber (CF) as a natural polymer material with a large surface area, multiple functional groups, even higher availability, and lower cost is also a competitive candidate

for high-efficiency CO_2 adsorption [11,12]. CF is expected to have better selectivity and higher efficiency towards CO_2 adsorption in waste gas such as vehicle exhaust. The selectivity depends largely on the types of functional groups on the CFs, especially for the selectivity between CO_2 and N_2, which are the two main components of waste gas. Therefore, the CO_2/N_2 selectivity has always been one of the major features in determining the CO_2 effectiveness of a material [13,14].

Functional groups on different CFs can vary drastically, which strongly affects the CO_2 adsorption capability. Hosakun *et al.* [15] introduced the possible interactions between CO_2 and functional groups on bacteria cellulose that act as Lewis bases or electron donors, where the CO_2 enables positive charges on the hydroxyl group and the CO_2 becomes negative due to electron transfer, inducing intra- or inter-hydrogen bonding between the CO_2 and the cellulose. Similar behavior also happened to the interactions between the amide site and the CO_2. Recently, a specific type of CF from paper waste has been thoroughly studied and possesses the potential to achieve high-performance CO_2 adsorption with a decent CO_2/N_2 selectivity [16,17]. However, directly studying the CF experimentally is tedious and time-consuming. Computational prediction in advance is of great assistance in searching for and sieving the most appropriate conditions under which the CF is able to work in its most effective manner.

In this study, CO_2 adsorption behaviors of CF from paper waste were modeled and investigated using molecular dynamics (MD) simulation. The behaviors under multiple conditions, including different temperatures, gas velocities, gas concentration, and gas components, were simulated to reflect the performance of the CFs (**Figure 4.1**). The CO_2 adsorption behaviors of AC were also modeled to compare with the CFs. The findings bring new insights and predictions on GHG control using green materials from biomass, paving the way towards a more carbon-neutral community.

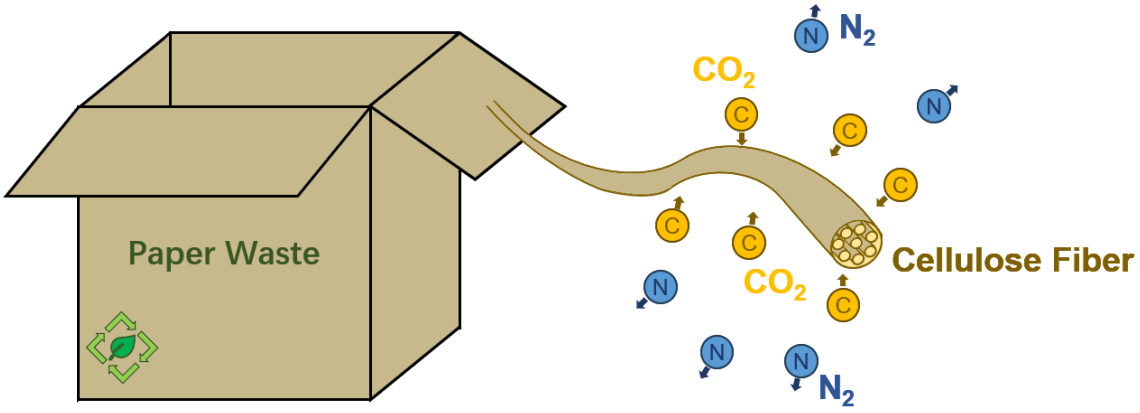

Figure 4.1. Schematic of cellulose fibers from paper waste achieving CO_2 adsorption with high CO_2/N_2 selectivity.

4.2 Methods

4.2.1 Model Design

A CF tube model was built using a unit cell of which a $C_6H_{10}O_5$ chain was twisted with another $C_6H_{10}O_5$ chain. Similarly, an AC tube model was also built by twisting two AC chains. Gas molecules, including N_2, O_2, and CO_2, were created separately. All models were relaxed before being used in MD simulations.

4.2.2 MD simulation

MD simulations were conducted using the Largescale Atomic/Molecular Massively Parallel Simulator (LAMMPS) [18]. The calculations were performed using the canonical ensemble (N, V, T), where the temperature was raised to 300 K in 4 ps. The interatomic interactions were described by the reactive force field (ReaxFF) [19]. For CO_2 adsorption studies with different velocities, three CF (or AC) tubes were set in the middle with their edges fixed and a number of CO_2 molecules were placed at the left side of the simulation box with a distance between each other to avoid atomic interactions at the beginning. After reaching the target temperature (300 K), an initial velocity (0.009 Ang/fs – 0.023 Ang/fs) was given to the CO_2 molecules for them to travel towards the CF (or AC) tubes, where a portion of the gas molecules would interact with the CF (or AC) tubes when they encountered. The adsorption ratios were recorded and presented. For CO_2 adsorption studies under different temperatures, a similar setup with three tubes in the middle with their edges fixed and a series of CO_2 molecules at the left side of the simulation box was used. The initial velocity of 0.015 Ang/fs and a temperature range from 240 K to 340 K

with a temperature step of 10 K were chosen for this simulation. The adsorption ratios were also recorded and presented. For the selectivity study, a single CF (or AC) tube was placed in the middle, together with 120 mixed gas molecules of N_2, O_2, and CO_2 at a concentration of 52.5%, 32.5%, and 15.0%, respectively, at both sides of the simulation box. Initially, two transparent walls were built to separate the gas molecules and the tube model from interactions before the target temperature. When reaching room temperature (300 K), the walls were removed to allow the gas molecules to naturally disperse in the simulation box for random interactions with the tube. After simulation, the numbers of N_2, O_2, and CO_2, adsorbed by the tube model were recorded for analysis.

4.2.3 Adsorption selectivity calculation

The CO_2/N_2 selectivity ($\alpha_{i/j}$) was calculated the equation defined as follows [5]:

$$\alpha_{i/j} = \frac{x_i/y_i}{x_j/y_j} \tag{4.1}$$

where x_i, x_j, y_i, and y_j are the molar fraction of the components i and j in the adsorptive and bulk adsorbate phases, respectively.

4.3 Results and Discussion

4.3.1 CO_2 adsorption performance under different conditions

Two CF chains were twisted to form a cellulose fiber tube as the unit cell for the computational studies (**Figure 4.2**a). As known to all, AC is one of the most commonly seen physical CO_2 adsorbents, hence, an AC tube model was also built by twisting two AC chains (**Figure 4.2**a) for comparison. Three tube models were placed in the middle and 24 CO_2 molecules were placed on the left side of the simulation box (**Figure 4.2**b and c). The tube models' edges were fixed to avoid being pushed by the CO_2 flow during the simulation. Meanwhile, the CO_2 molecules kept a distance between each other to prevent atomic interactions before the target temperature. After reaching the target temperature, an initial velocity was given to the CO_2 molecules, enabling them to move towards the tubes. When the CO_2 flow and the tubes were sufficiently close, atomic interactions happened and the adsorption ratios were recorded. As two examples that are shown in **Figure 4.2**b and c, an initial velocity of 0.015 Ang/fs was provided to the CO_2 molecules when the temperature reached 300 K, allowing them to travel from the left to the right. CFs were able to adsorb

75.00% CO_2 molecules, whereas AC could only adsorb 66.67% of the molecules under that velocity and temperature.

After adjusting the initial velocities of the CO_2 molecules at room temperature (300 K) (**Figure 4.2**e and f), a series of adsorption ratios was collected (**Figure 4.2**d). Both CFs and AC possessed a similar adsorption trend with the velocities of CO_2 flow. When the initial velocities were lower than 0.017 Ang/fs, CFs showed a relatively stable adsorption performance of over 70.00% while AC's adsorption ratios gradually decreased to 66.67% when the velocity was reaching 0.016 Ang/fs, revealing a higher stability of CFs than that of AC. When the initial velocities climbed to a degree higher than 0.017 Ang/fs, the adsorption abilities of both CFs and AC drastically worsened until 0.023 Ang/fs, of which the CO_2 flow was too strong to be caught by the materials. This result indicated that the CFs could adapt to a larger range of gas flow and had a stronger adsorption ability towards CO_2 than the AC.

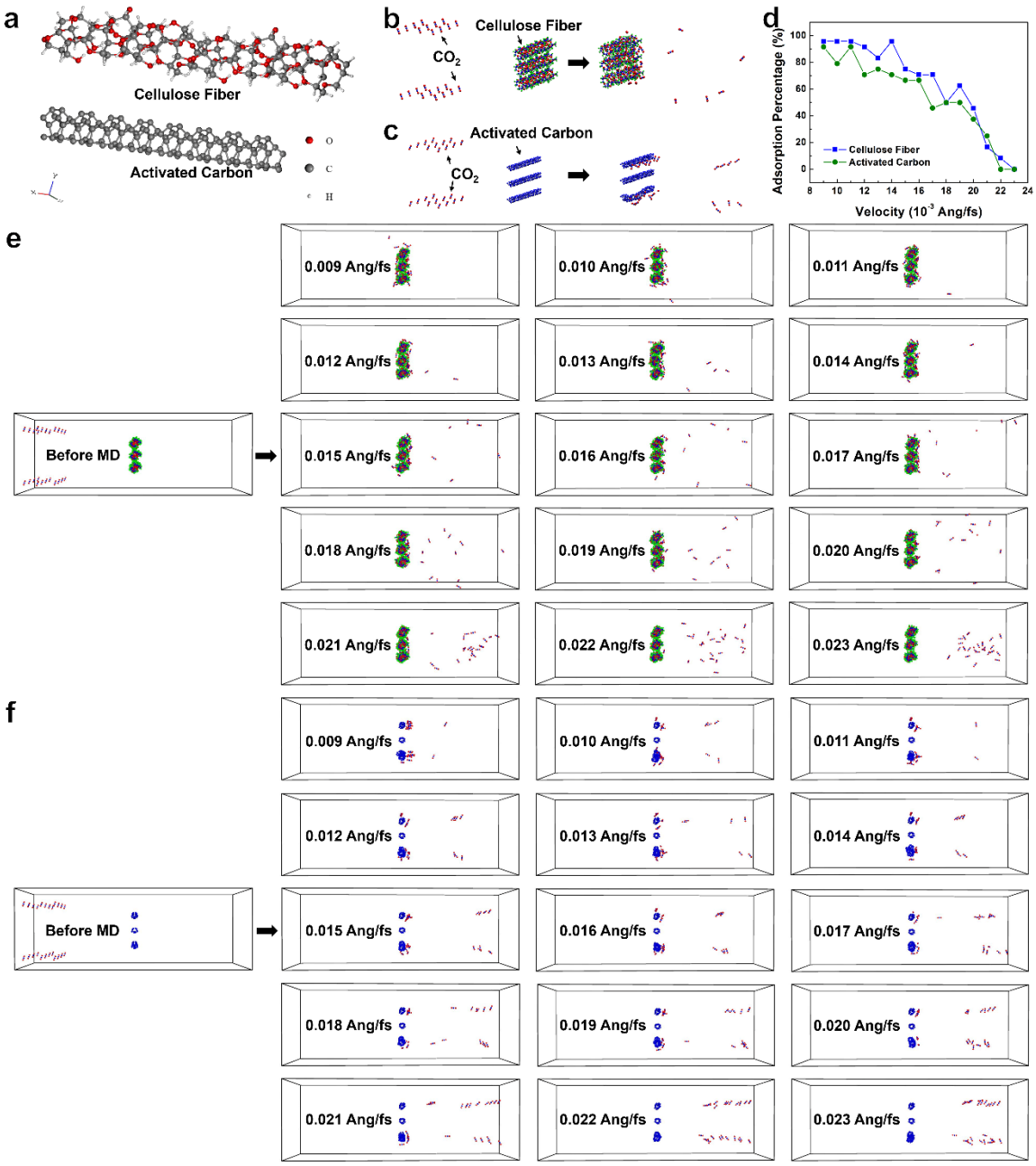

Figure 4.2. (a) CF and AC tube models for all the computational studies. (b) MD simulation box setup for CFs' velocity and temperature simulations, and the result with the CO_2 velocity of 0.015 Ang/fs and at 300 K. (c) MD simulation box setup for AC's velocity and temperature simulations, and the result with the CO_2 velocity of 0.015 Ang/fs and at 300 K. (d) CO_2 adsorption ratios of CFs and AC with the CO_2 velocities ranging from 0.009 Ang/fs to 0.023 Ang/fs at 300 K. (e) CO_2 adsorption behavior of CFs with a velocity of CO_2 flow from 0.009 Ang/fs to 0.023 Ang/fs. (f) CO_2 adsorption behavior of AC with a velocity of CO_2 flow from 0.009 Ang/fs to 0.023 Ang/fs.

To identify the most effective working temperature range for CFs, a list of temperatures ranging from 240 K to 340 K was applied to the simulation box with a fixed CO_2 flow velocity of 0.014 Ang/fs (**Figure 4.3**a). For comparison, similar simulations using AC were also conducted (**Figure 4.3**b) and the results were collected (**Figure 4.3**c). Despite the fact that AC has a weaker adsorption ability than CFs towards CO_2 under that velocity showing in the previous paragraph, the most effective working temperature ranges for CFs and AC were also different. For CFs, the adsorption ratio was above 60% over the entire temperature range, and the most promising working temperature was from 290 K to 310 K (~17 - 37 ℃), which is around room temperature. For AC, the optimal working temperature was from 270 K to 290 K (~-3 - 17 ℃), which is lower than the room temperature. Moreover, the high adsorption ratio of the AC could not last when the temperature rose above 310 K. These findings evidenced that CFs' CO_2 adsorption capability can stay reliable for a large range of temperatures, and it is especially effective at around room temperature, exhibiting a much better adaptability than traditional AC.

In addition, the sensitivity of CFs (**Figure 4.3**d) was validated by calculating the closest distances between the CF or AC tubes and each of the CO_2 molecules when the molecules first approached the tubes. It was found that the distances between CFs and CO_2 were mostly in a range of 6.2763 Å – 8.3612 Å with an average of 7.4057 Å, where the majority of the distances was longer than the distances between AC and CO_2 (4.9004 Å – 7.1138 Å with an average of 5.9545 Å). This result indicated that the CO_2 started interacting with the CFs earlier than the AC, meaning that the sensitivity of CFs towards CO_2 is stronger than AC, which also explained the better adaptation with the flow speed in the previous description.

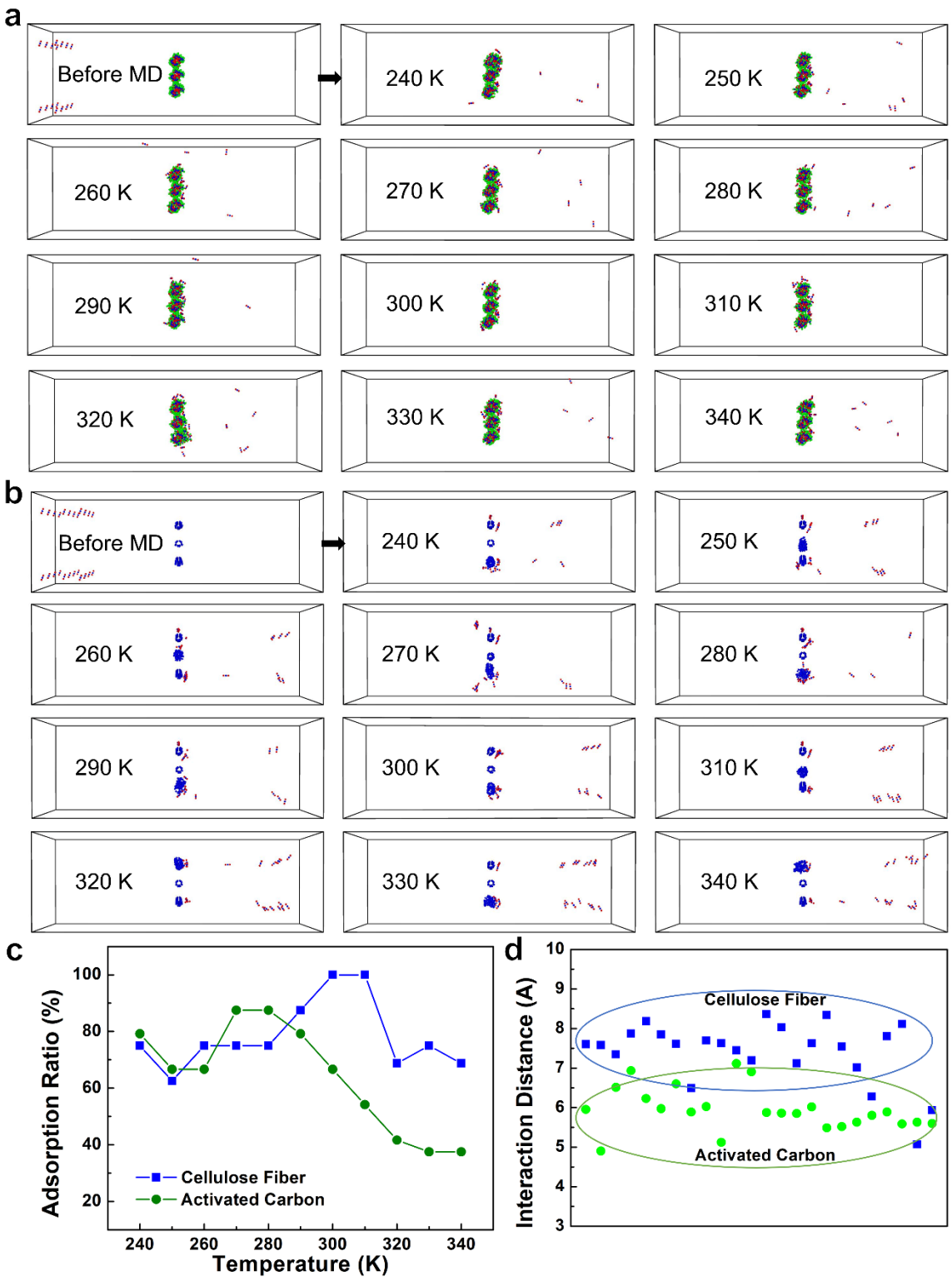

Figure 4.3. (a) CO_2 adsorption behavior of CFs with system temperatures from 240 K to 340 K. (b) CO_2 adsorption behavior of AC with system temperatures from 240 K to 340 K. (c) CO_2 adsorption

ratios of CFs and AC with the CO_2 velocity of 0.015 Ang/fs at temperatures ranging from 240 K to 340 K. (d) Interaction distances for each CO_2 approaching CF and AC.

4.3.2 Gas selectivity performance

As the highest component in air and waste gas, N_2 is an inevitable factor to consider when designing a CO_2 adsorbent. The CO_2/N_2 selectivity can be used to characterize a CO_2 adsorbent's effectiveness in such a situation, even though the calculation method for the selectivity has not been unified. To estimate the CFs' effectiveness of CO_2 adsorption in N_2-rich conditions, a mixed gas model was designed (**Figure 4.4**a). The mixed gas has 120 gas molecules in total with N_2, O_2, and CO_2 ratios of 52.5%, 32.5%, and 15.0%, respectively, where the O_2 was used to adjust component ratios in the mixed gas. The gas molecules were placed on both sides of the simulation box with two transparent walls to prevent them from interacting with the CF tube in the middle before the system reached the target temperature. The walls were removed after raising the temperature to room temperature, which then allowed the mixed gas molecules to randomly distribute in the simulation box and freely interact with the CF tube. The final pattern is shown in **Figure 4.4**b. During the process, many N_2 molecules were able to interact with or even be captured by the CF tube, however, they detached from the CF tube soon, leaving the CF tube mostly free of N_2 (**Figure 4.4**e). This was probably because of the weak Van der Waals connections between the N_2 and the CFs, as well as constant forces from surrounding molecules. The same simulation was also performed using AC to further confirm the conclusion (**Figure 4.4**c). As shown in **Figure 4.4**d, AC evenly captured all three types of gas molecules, which is the reason for the empty space around it. **Figure 4.4**e and f revealed the adsorption ratios of the three types of gas molecules within their own types by CFs and AC, respectively. Almost no N_2 was captured by the CF tube yet nearly 40% of the N_2 molecules were captured by the AC tube. Meanwhile, the same number of CO_2 molecules were captured by the CF tube and the AC tube, indicating a similar CO_2 capacity. Both the CF and the AC barely identified O_2 from CO_2, indicating that the oxygen in both the O_2 and CO_2 could serve as the most active site when interacting with the CF and the AC. Based on the data we collected and the equation (1), the CO_2/N_2 selectivity was calculated, which was 12.26 for the CF and 0.98 for the AC. These numbers are supposed to be much smaller than reality because only a single string of the CF or AC tube was used in the

simulations, yet the trend that the CF has a much better CO_2/N_2 selectivity than the AC can be obtained [20]. Overall, using the CF as an CO_2 adsorbent reduced the CO_2 content in the mixed gas by 3.78%, whereas AC only reduced the CO_2 content by 0.53% (**Figure 4.4**g). Although the CF from paper waste failed in distinguishing O_2 and CO_2, thanks to the excellent CO_2/N_2 selectivity, it is still considered a promising candidate for CO_2 adsorbents, especially when dealing with waste gas from engines.

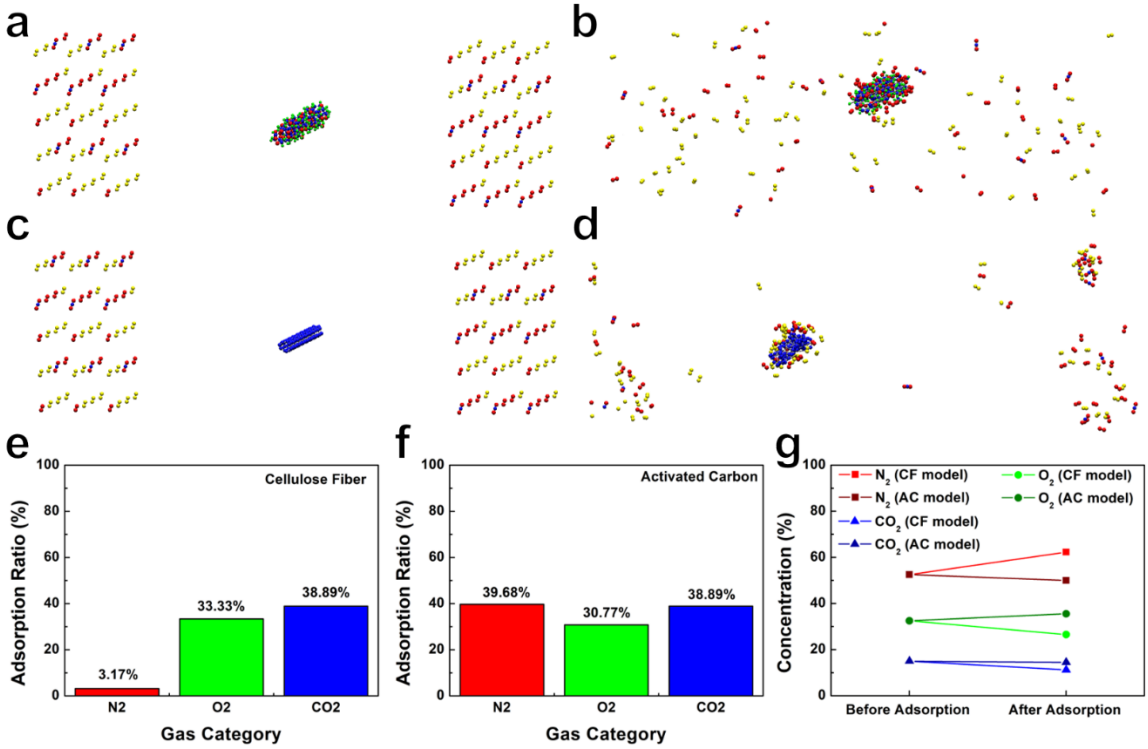

Figure 4.3. (a) MD simulation box setup for CFs' CO_2 selectivity in a gas mixture of N_2 (two-atom molecules in yellow), O_2 (two-atom molecules in red), and CO_2 (three-atom molecules). (b) Result of CF gas adsorption in the gas mixture. (c) MD simulation box setup for AC's CO_2 selectivity in the gas mixture. (d) Result of AC gas adsorption in the gas mixture. (e) Adsorption ratios of N_2, O_2, and CO_2 in CFs. (f) Adsorption ratios of N_2, O_2, and CO_2 in AC. (g) Concentration changes of N_2, O_2, and CO_2 before and after the adsorption simulation using CFs and AC.

4.4 Conclusions

As more and more attention is devoted to environmental issues, greenhouse gas control has become one of the most important topics in the twenty-first century. Cellulose fiber is abundant, green, and low-cost, and possesses a unique structure and a large number of useful functional groups towards CO_2 adsorption, which may be able to serve as a candidate

for efficient decarbonization. Experimentally studying the performance of cellulose fibers is time-consuming. Here, a computational study of the cellulose fiber regarding its CO_2 adsorption behavior and potential was conducted. The tolerable CO_2 flow speed and the most effective working temperature of the cellulose fiber were predicted, and its sensitivity towards CO_2 and CO_2/N_2 selectivity were calculated. Compared with traditional activated carbon, the cellulose fiber exhibited better adaptability regarding flow speed and temperature, a stronger sensitivity towards CO_2, and a much larger CO_2/N_2 selectivity. The findings proved the potential of the cellulose fiber being used as CO_2 adsorbent and provided instructions and predictions on the use of cellulose fiber in this field, paving the way towards a carbon-neutral society.

Reference

[1] S.M.S.U. Eskander and S. Fankhauser, Reduction in greenhouse gas emissions from national climate legislation, *Nature Climate Change* 10 (2020) 750-756.

[2] A. Gambhir, M. George, H. McJeon, N.W. Arnell, D. Bernie, S. Mittal, A.C. Köberle, J. Lowe, J. Rogelj, and S. Monteith, Near-term transition and longer-term physical climate risks of greenhouse gas emissions pathways, *Nature Climate Change* 12 (2022) 88-96.

[3] G.S. Malhi, M. Kaur, and P. Kaushik, Impact of Climate Change on Agriculture and Its Mitigation Strategies: A Review, *Sustainability* 13 (2021) 1318.

[4] J.H. Park, J. Yang, D. Kim, H. Gim, W.Y. Choi, J.W. Lee, Review of recent technologies for transforming carbon dioxide to carbon materials, *Chemical Engineering Journal* 427 (2022) 130980.

[5] S. Chen, M. Zhu, Y. Tang, Y. Fu, W. Li, and B. Xiao, Molecular simulation and experimental investigation of CO_2 capture in a polymetallic cation-exchanged 13X zeolite, *Journal of Materials Chemistry A* 6 (2018) 19570-19583.

[6] M.A. Khansary, M.A. Aroon, and S. Shirazian, Physical adsorption of CO2 in biomass at atmospheric pressure and ambient temperature, *Environmental Chemistry Letters* 18 (2020) 1423-1431.

[7] F. Vega, F.M. Baena-Moreno, L.M.G. Fernández, E. Portillo, B. Navarrete, and Z. Zhang, Current status of CO_2 chemical absorption research applied to CCS: Towards full deployment at industrial scale, *Applied Energy* 260 (2020) 114313.

[8] A.A. Olajire, CO_2 capture and separation technologies for end-of-pipe applications – A review, *Energy* 35 (2010) 2610-2628.

[9] V.M. Georgieva, E.L. Bruce, M.C. Verbraeken, A.R. Scott, W.J. Casteel Jr., S. Brandani, and P.A. Wright, Triggered Gate Opening and Breathing Effects during Selective CO_2 Adsorption by Merlinoite Zeolite, *Journal of the American Chemical Society* 141 (2019) 12744-12759.

[10] A. Rehman, Y.J. Heo, G. Nazir, and S.J. Park, Solvent-free, one-pot synthesis of nitrogen-tailored alkali-activated microporous carbons with an efficient CO_2 adsorption, *Carbon* 172 (2021) 71-82.

[11] F. Valdebenito, R. García, K. Cruces, G. Ciudad, G. Chinga-Carrasco, and Y. Habibi, CO_2 Adsorption of Surface-Modified Cellulose Nanofibril Films Derived from Agricultural Wastes, *ACS Sustainable Chemistry & Engineering* 6 (2018) 12603-12612.

[12] N.A.D. Ho and C.P. Leo, A review on the emerging applications of cellulose, cellulose derivatives and nanocellulose in carbon capture, *Environmental Research* 197 (2021) 111100.

[13] Y. Chen, D. Lv, J. Wu, J. Xiao, H. Xi, Q. Xia, and Z. Li, A new MOF-505@GO composite with high selectivity for CO_2/CH_4 and CO_2/N_2 separation, *Chemical Engineering Journal* 308 (2017) 1065-1072.

[14] E. Haldoupis, S. Nair, and D.S. Sholl, Finding MOFs for Highly Selective CO_2/N_2 Adsorption Using Materials Screening Based on Efficient Assignment of Atomic Point Charges, *Journal of the American Chemical Society* 134 (2012) 4313-4323.

[15] Y. Hosakun, K. Halász, M. Horváth, L. Csóka, and V. Djoković, ATR-FTIR study of the interaction of CO_2 with bacterial cellulose-based membranes, *Chemical Engineering Journal* 324 (2017) 83-92.

[16] Y. Zhou, Y. Zhang, and X. Li, Upcycling of paper waste for high-performance lithium-sulfur batteries, *Materials Today Energy* 19 (2021) 100591.

[17] Y. Zhou, R. Chen, J. He, and X. Li, Cellulose fiber-enabled mitigation of polysulfide shuttling and dendritic lithium growth in lithium–sulfur batteries, *Journal of Power Sources* 584 (2023) 233595.

[18] S. Plimpton, Fast Parallel Algorithms for Short-Range Molecular Dynamics, *Journal of Computational Physics* 117 (1995) 1-19.

[19] K. Ganeshan, Y. K. Shin, N. C. Osti, Y. Sun, K. Prenger, M. Naguib, M. Tyagi, E. Mamontov, D. Jiang, A. C. T. Duin, Structure and Dynamics of Aqueous Electrolytes Confined in 2D-TiO_2/$Ti_3C_2T_2$ MXene Heterostructures, *ACS Applied Materials & Interfaces* 12 (2020) 58378-58389.

[20] H. Jedli, M.M. Almoneef, M. Mbarek, A. Jbara, and K. Slimi, Experimental study of CO_2 and N_2 adsorption on activated carbon, *Materials Research Express* 10 (2023) 075601.

Chapter 5. Upcycled CNT/graphene Hybrid from End-of-life Batteries for Energy Storage

5.1 Introduction

Batteries are critical energy storage devices to decarbonize our societies [1-3]. High-capacity batteries, especially lithium-ion batteries, are in strong demand for electric vehicles (EVs) and stationary storage systems [4-6]. However, the disposal of end-of-life Li-ion batteries not only causes severe pollution to the environment, but also throws away critical materials. Therefore, it is vital to recycle and reintegrate end-of-life batteries into the battery supply chain to meet climate change and circular economy goals and to ensure good stewardship of critical materials [7,8]. On the other hand, Li-ion batteries are reaching their theoretical limits. Lithium-sulfur (Li-S) battery is one of the most promising "post-Li-ion" energy storage systems due to its high theoretical capacity (1,672 mAh/g) and energy density (2,600 Wh/kg) [9-13]. Nevertheless, the sulfur in Li-S battery cathodes suffers from an extremely low electrical conductivity and a large volume expansion (78%) upon lithiation [14]. Hence, an effective framework that synergistically provides high electrical conductivity and excellent volume buffering capability is required to solve these challenges in Li-S batteries.

Today's Li-ion batteries consist of lithium metal oxide cathodes, carbon (graphite) anodes, liquid electrolytes, polymer separators, and metal current collectors [15]. Many efforts have been focused on recovery of lithium, cobalt, and nickel from end-of-life Li-ion battery cathodes [16-18]. Compared to the cathode recycling, anode recycling has been largely overlooked. Graphite is commonly used as the anode material in Li-ion batteries and the anode graphite is considered a non-renewable resource [19]. Recently we upcycled anode graphite into graphene [20]. Graphene, a two-dimensional material made up of sheets of carbon atoms with exceptional electrical, mechanical, and thermal properties, has the potential to revolutionize industries ranging from healthcare to energy storage devices such as batteries [21,22]. However, graphene alone in Li-S batteries cannot encapsulate sulfur to increase sulfur loading and buffer volume expansion [23]. Carbon nanotubes (CNTs) can load more sulfur because of their tubular structure [24-26]. CNT/graphene hybrid nanostructures are anticipated to render the CNT/graphene/sulfur cathode with high

conductivity and provide extra storage to load more sulfur and accommodate volume expansion. However, most recent studies regarding CNT/graphene composites simply mixed the two materials with relatively weak connections, which limited the electrical conductivity and mechanical properties. Seamlessly growing CNTs on graphene can generate much stronger connections and natural interfaces, allowing electrons to be more freely conducted and accommodating more severe deformations such as large volume expansions. Both advantages can improve the performance of Li-S batteries. Yet, growing CNTs on graphene has been challenging and costly [27]. Chemical vapor deposition (CVD) is one of the most commonly adopted methods to grow CNTs on graphene, however, the cost-effectiveness of using CVD is debatable and the carbon sources are usually non-green [28]. Utilizing low-cost "green" feedstocks is favorable for lowering carbon emission and sustaining supply chain.

Herein, we report an all-green strategy for growing carbon nanotubes (CNTs) on graphene. The graphene was upcycled from end-of-life lithium-ion batteries using an upgraded, low-cost method and the CNTs were then grown directly on the graphene by pyrolyzing cotton as the carbon source and yeast as the catalyst (**Figure 5.1**). Molecular dynamics (MD) simulations unveiled the seamless structure of multi-wall CNT on graphene and validated the true catalytic component in yeast for the first time. When being used in a Li-S battery cathode, the graphene provided a highly conductive network while the CNTs enabled high sulfur loading and volume buffering, rendering the battery with high capacity, high stability, and long lifespan. Such all-green CNT/graphene strategy presents new pathways to upcycling batteries to second life.

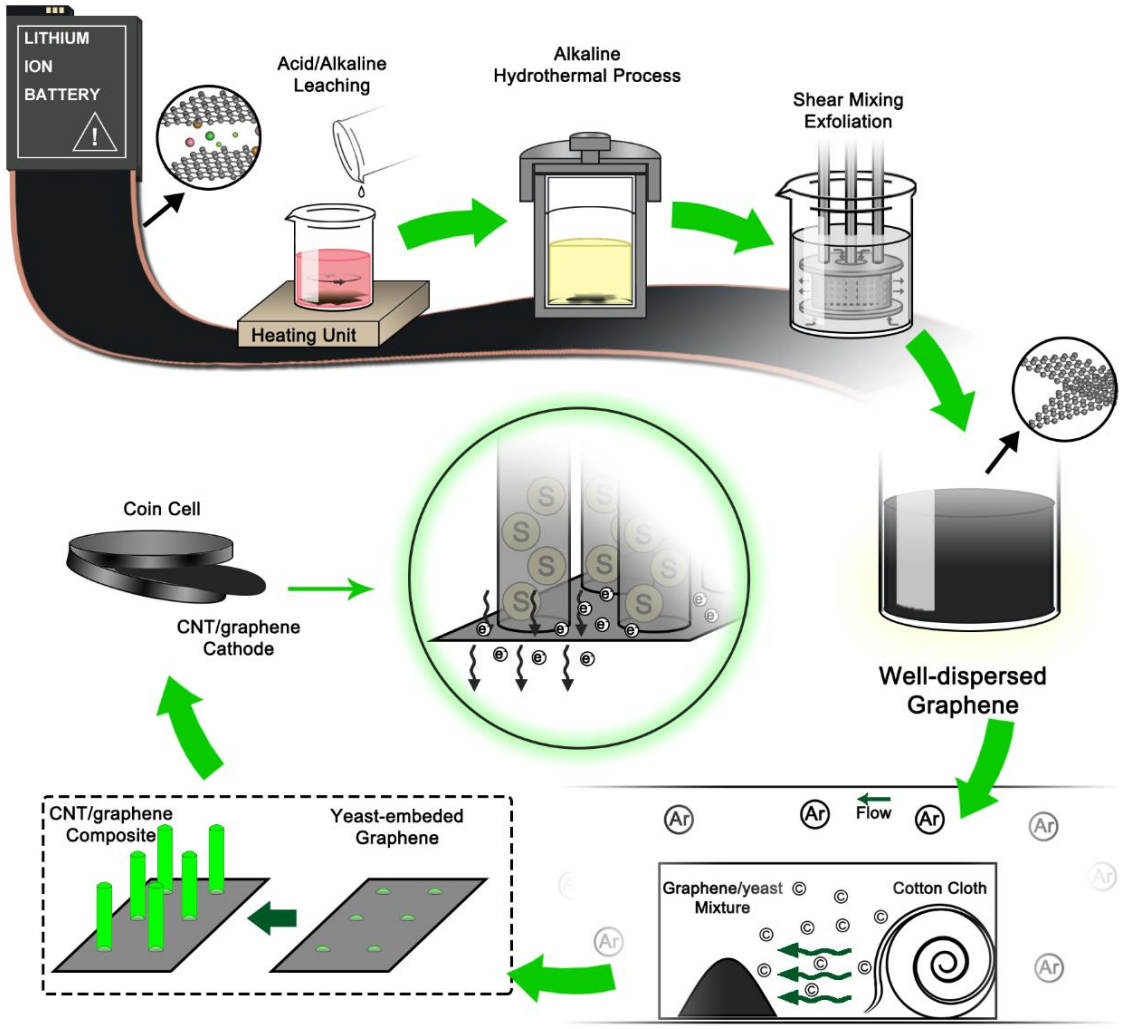

Figure 5.1. Schematic for upcycling end-of-life Li-ion battery anode graphite into graphene and growing CNTs on graphene to construct Li-S batteries.

5.2 Methods

5.2.1 End-of-Life Battery Pre-treatment

End-of-life batteries were manually disassembled. The cathodes ($LiCoO_2$, etc.) and anodes (graphite), together with separators, were collected and smashed into smaller parts. The mixture was briefly washed twice with diluted H_2SO_4 and H_2O_2 acids and sieved. The liquid was collected for Co and Ni recycling and the solid remnant (mixture of graphite with impurities and separators) was collected for further processing.

5.2.2 Upcycling Graphite to Graphene

End-of-life Li-ion battery anode graphite contains a large number of impurities including Cu and Al current collector scraps, remnant Co and Ni salts from cathodes, F-

containing binders, and leftover S. Such graphite powders were first alkaline washed for 2 hours at 80 °C using 4N NaOH solutions to partially remove Al and binders and break remaining graphite chunks. After filtration and washing with DI water, the powders were acid leached for 2 hours at 80 °C using 4N H_2SO_4 solution mixed with 35% H_2O_2 solution at a volume ratio of 5:1 to remove other impurities such as Co and Ni salts, Cu collectors, and most Al collectors. Thereafter, a newly introduced alkaline hydrothermal process was conducted using 8N NaOH solutions at 160 °C for 6 hours to further remove stubborn binders and Al residuals. This step has not been reported elsewhere and can be added to existed battery recycling routines. After filtrated and dried at 80 °C for 12 hours, the powders in DI water were shear mixed at 3,600 rpm for 5 hours to produce graphene. The graphene concentration was measured to be 1 mg/mL.

5.2.3 Growing CNTs on Graphene

The graphene solution was mixed with yeast with a mass ratio of 1:15 by ultrasonication at room temperature for 20 minutes. The obtained graphene/yeast solution was then frozen for 12 hours and freeze-dried for 12 hours. The freeze-dried powders were transported to a homemade steel box and placed at one end of the box, together with a roll of 0.35 g cotton cloth at the other end (**Figure 5.1**). The steel box was transferred into a quartz tube furnace, thermally heated to and maintained at 850 °C for 3 hours with Ar flow, and then cooled down to room temperature.

5.2.4 Battery Assembling

The obtained CNT/graphene powders were mixed with sulfur powders at a mass ratio of 1:2 and transferred to an autoclave which was then thermally treated at 155 °C for 12 hours and at 200 °C for 2 hours to impregnate sulfur into the CNT/graphene powders to form CNT/graphene/S composite powders. The as-obtained powders, carbon black, and polyvinyl difluoride (PVDF) were mixed with a mass ratio of 90:5:5 in N-methyl-2-pyrrolidone (NMP) solution to produce a homogeneous slurry. The slurry was coated onto a piece of Al foil and dried at 60 °C for 12 hours. Afterward, the CNT/graphene/S coated Al foil was punched into circular disks to be used as cathodes. The reference materials including commercial graphite (Sigma-Aldrich), recycled end-of-life anode graphite, and graphene from the end-of-life anode graphite (upcycled graphene) were treated using the same procedures with the same mass ratio of sulfur to make the reference cathodes for

comparison. The Li-S coin cells were assembled using the aforementioned cathodes, lithium metal anodes, and polypropylene separators (Cellgard 2400). The electrolyte was produced by dissolving 1 mol/L lithium bis(trifluoromethanesulfony)imide and 0.4 mol/L $LiNO_3$ in an organic solvent of dimethoxyethane + 1,3-dioxolane at a 1:1 vol ratio. The amount of electrolyte for each cell was 16 μL.

5.2.5 Density Functional Theory and Molecular Dynamics Calculations

The QUANTUMESPRESSO software package was used to perform the density functional theory (DFT) calculations with a norm-conserving pseudopotential and with the SCAN meta-GGA exchange-correlation functional [29,30]. A gamma k-point mesh was used, and the kinetic energy cutoffs for the wave function and charge density were 30 and 300 Ry, respectively. The models were relaxed using the Broyden-Fletcher-Goldfarb-Shanno quasi-Newton algorithm [31]. MD calculations were conducted using the Largescale Atomic/Molecular Massively Parallel Simulator (LAMMPS) [32]. Models of double-layer graphene with twelve doped atoms (potassium, phosphorous, or carbon) in the center were constructed to simulate the CNT growth on graphene. The calculations were performed using the canonical ensemble (N, V, T), where the absolute temperature was raised to 1,123 K (850 °C) in 1.05 ps before successively adding carbon atoms every 5 ps. The interatomic interactions were described by the reactive force field (ReaxFF) [33].

5.2.6 Materials and Structural Characterization

Scanning electron microscopy (SEM) (FEI Quanta 650 with energy-dispersive X-ray spectroscopy (EDS) detector), X-ray diffraction (XRD) (Empyrean Multipurpose X-ray diffractometer equipped with Cu Kα radiation (λ = 0.15406 nm)), and transmission electron microscopy (TEM) (FEI Titan Transmission Electron Microscope) were used to characterize the as-prepared CNT/graphene hybrid nanostructures, reference materials, and cathodes.

5.2.7 Electrochemical Characterization

A LAND CT2003A battery test instrument was used to conduct galvanostatic charge/discharge measurements, including cyclic performance, rate performance, and polarization potential. The polarization voltage was calculated using the following equation in the test station

$$V_p = V_t - IR_0 - V_{oc} \tag{5.1}$$

where V_p is the polarization voltage, V_t is the terminal voltage, I is the current, R_0 is the ohmic resistance, and V_{oc} is the open-circuit voltage, which were measured by the test station. A CHI 660E electrochemical workstation was employed to conduct the electrochemical impedance spectroscopy (EIS) tests in the frequency range from 100 kHz through 0.01 Hz with an alternating current (AC) perturbation of 5 mV, as well as the cyclic voltammetry (CV) test from 1.5 V to 2.8 V with a scan rate of 0.0001 V/s. Zview software was applied to perform the curve-fitting on the EIS test data.

5.3 Results and Discussion

5.3.1 Upcycling anode graphite into graphene

Table 5.1. Element contents after each purification step.

Element	C	O	Co	S	Mn	Ni	F	Al	Si	Na
Raw graphite (wt%)	60.4	18.3	7.2	4.9	3.3	3.3	1.6	0.8	0.1	0.0
Leached graphite (wt%)	87.0	4.4	0.0	0.0	0.0	0.0	7.7	0.7	0.0	0.3
Hydrothermal graphite (wt%)	94.9	3.9	0.0	0.0	0.0	0.0	0.7	0.0	0.0	0.5

Anode graphite often has impurities consisting of Co, S, Mn, Ni, F, Al, and Si (**Table 5.1**). The alkaline and acid leaching treatments removed most impurities of Co, S, Mn, Ni, and Si. Follow-up, novel alkaline hydrothermal treatment with concentrated NaOH further eliminated stubborn aluminum and binders without using expensive organic solutions, which highly increases the cost, or high-temperature treatment [34], which makes exfoliation harder by compressing graphite structure, enabling the graphite with a purity of more than 94% and swollen structure (**Figure 5.3**). This novel step has not been reported elsewhere and can be added to existed recycling process to achieve high-purity graphite and certain applications (eg. high-quality graphene production). With the assistance of both hydrogen ions and hydroxide ions, the carbon layer spacing in the treated graphite expanded from 0.336 nm to 0.402 nm (19.64% expansion) (**Figure 5.2**), which facilitated the shear mixing exfoliation of the graphite into graphene (**Figure 5.3**c). The same carbon layer spacing has also been found by Zhang *et al.* [20], where an expansion of 14.7% was experimentally observed. The as-obtained graphene consists of both single-layer and multilayer graphene with an average edge length of 1 micron. XRD inspection (**Figure 5.3**d) revealed graphite (002) peaks from both recycled graphite and the graphene derived from it (upcycled graphene), indicating the high purity of the obtained graphene. High-

resolution TEM imaging (**Figure 5.2**c and **Figure 5.3**f) reveals the high-quality upcycled graphene with (002) orientation [35].

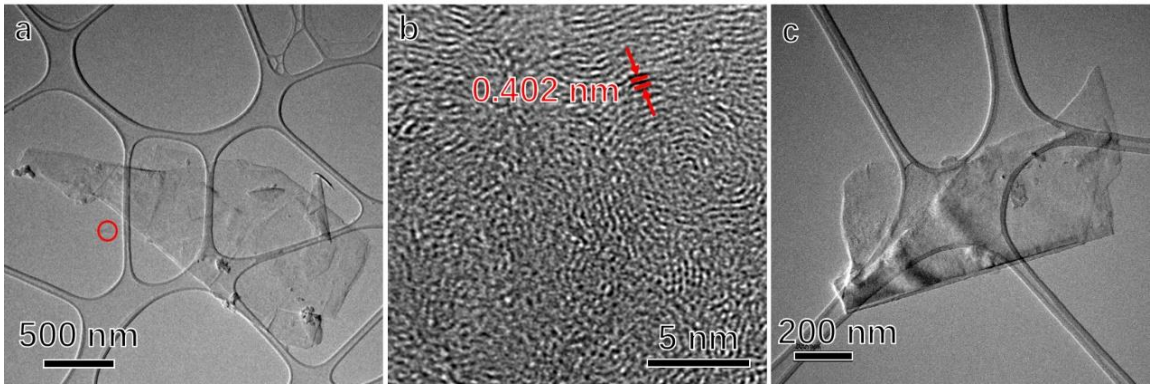

Figure 5.2. TEM image of upcycled graphene. (a) Low-resolution TEM image of a graphene sheet. (b) High-resolution TEM image of the circled area in (a). (c) Low-resolution TEM image of another graphene sheet.

The Li-ion intercalation and deintercalation in battery cycling expanded the carbon layers of the anode graphite, and the acid/alkaline leaching of recycled graphite further expanded the layers [20]. The expanded layers enable more efficient exfoliations to harvest graphene. To study the phenomenon, a set models consisting of H^+, OH^-, and graphene layers were established for the density functional theory (DFT) study. The H^+ and OH^- ions are able to insert into the space between two carbon layers, leading to 14.78% spacing expansion (from 4.343 Å to 4.985 Å) due to the H^+ insertion (**Figure 5.3**g) and 25.67% expansion (from 4.343 Å to 5.458 Å) from the OH^- insertion (**Figure 5.3**h). This explains the experimentally observed 19.64% expansion resulting from the acid/alkaline leaching and alkaline hydrothermal treatments.

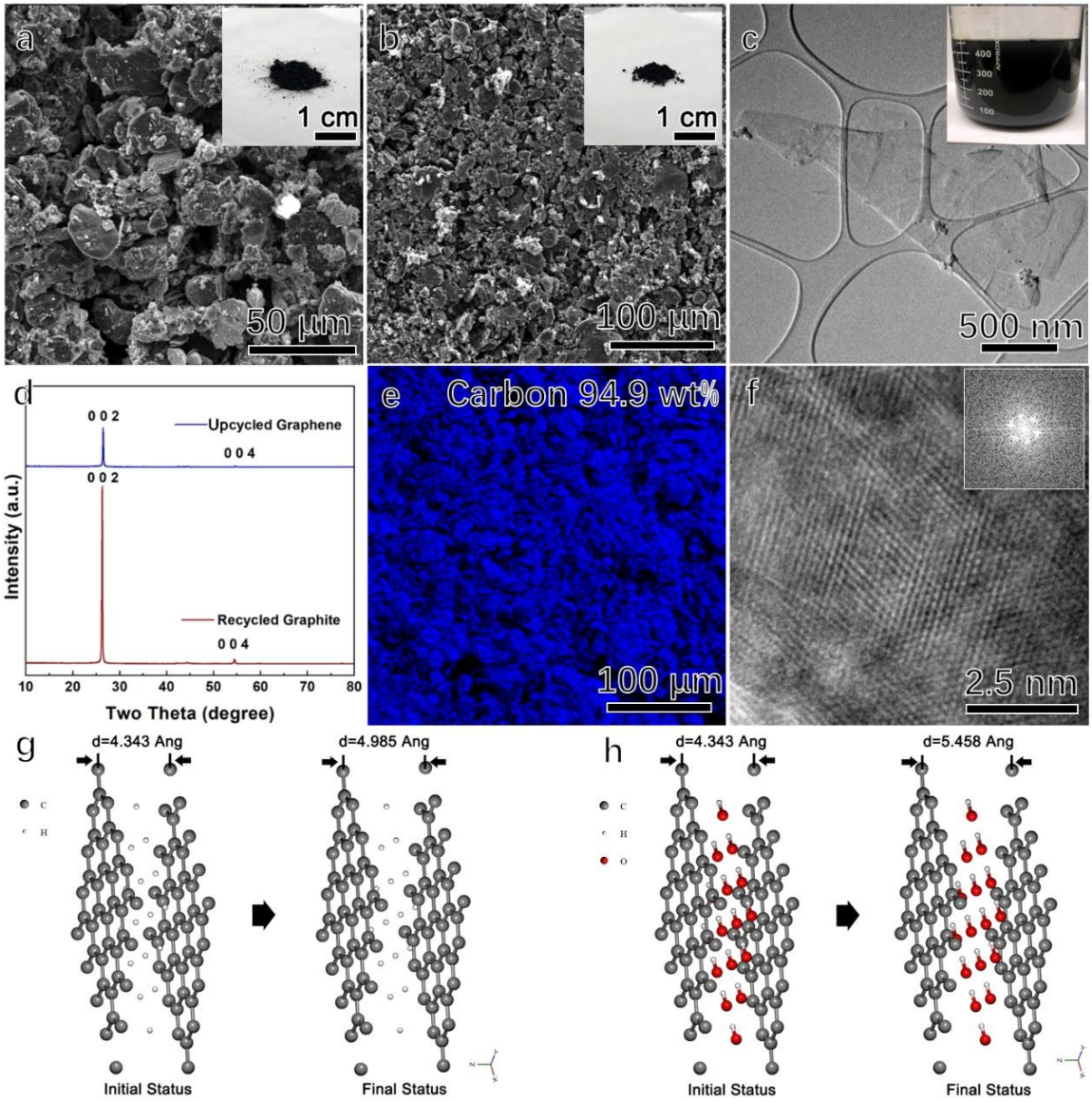

Figure 5.3. Characterization and modeling of upcycling graphite into graphene. (a) SEM image of recycled graphite (inset: optical image of recycled graphite) before purification. (b) SEM image of recycled graphite (inset: optical image of recycled graphite) after purification. (c) Low-resolution TEM image of an upcycled graphene sheet (inset: corresponding graphene dispersed in DI water). (d) XRD spectra of recycled graphite and upcycled graphene. (e) Carbon EDS map of recycled graphite after purification. (f) High-resolution TEM image of an upcycled graphene sheet (inset: corresponding FFT image). (g) DFT calculated H^+-induced spacing expansion. (h) DFT calculated OH^--induced spacing expansion.

5.3.2 Greenly growing CNTs on graphene

Table 5.2. Direct carbon emission estimation of synthesizing CNT/graphene with different

techniques.

No.	Graphene source	CNT source	Carbon emission (gCO_2e)	Ref.
1	960 mL C_2H_2	1305 mL C_2H_2	2292.18	36
2	150 mL CH_4	6 mL C_2H_2	8.83	37
3	200 mL CH_4	N/A	3.68	38
4	1500 mL CH_4	250 mL C_2H_2	280.59	39
5	60 mL C_2H_2	500 mL C_2H_2	566.72	40
6	150 mL CH_4	30 mL C_2H_2	33.12	41
7	3.33 mL C_2H_2	225 mL C_2H_2	231.07	42
8	600 mL CH_4	15 mL C_2H_4	11.10	43
9	150 mL CH_4	2 mL C_2H_2	4.78	44
10	N/A	400 mL C_2H_4	1.55	45
11	8000 mL CH_4	2000 mL C_2H_4	154.95	28
12	4000 mL CH_4	N/A	73.6	46
Ours	N/A	0.3 g Cotton cloth	0.29	

Pyrolysis was employed to grow CNTs on the upcycled graphene (**Figure 5.1)**. Graphene/yeast powders were obtained by adding yeast into graphene solution and freeze-drying the solution. The powders were placed into a homemade steel box together with a roll of cotton cloth (or other biomass materials) to provide gaseous carbon during pyrolysis. Such eco-friendly approach to growing CNTs on graphene produced less carbon emission than other CNT growth methods (**Table 5.2**). SEM inspection (**Figure 5.6**a and b) revealed that graphene sheets were fully covered with CNTs. It is worth noting that without yeast or without the cotton cloth, no CNTs were observed on the graphene after pyrolysis under the same conditions, suggesting that yeast is essential for CNT growth as catalyst instead of carbon sources. In addition, if pyrolysis temperature was below 850 °C and/or pyrolysis time was less than 3 hours, CNTs were not fully developed. Tubular CNTs (**Figure 5.6**c) provide storage room for sulfur loading. HRTEM inspection unveiled that the CNTs have diameters of 20 – 60 nm and lengths of several microns with 20 – 30 wall layers. XRD inspection (**Figure 5.4**) revealed that the CNT/graphene hybrid nanostructures are of high purity without preferred orientation. TEM imaging (**Figure 5.6**d and e) revealed that the CNTs grew seamlessly on the graphene with the base of concentric carbon rings which were validated by MD simulations (**Figure 5.6**h). This CNT/graphene hybrid nanostructures provide unobstructed paths for electron and ion transportation, enabling superlative electrical conductivity.

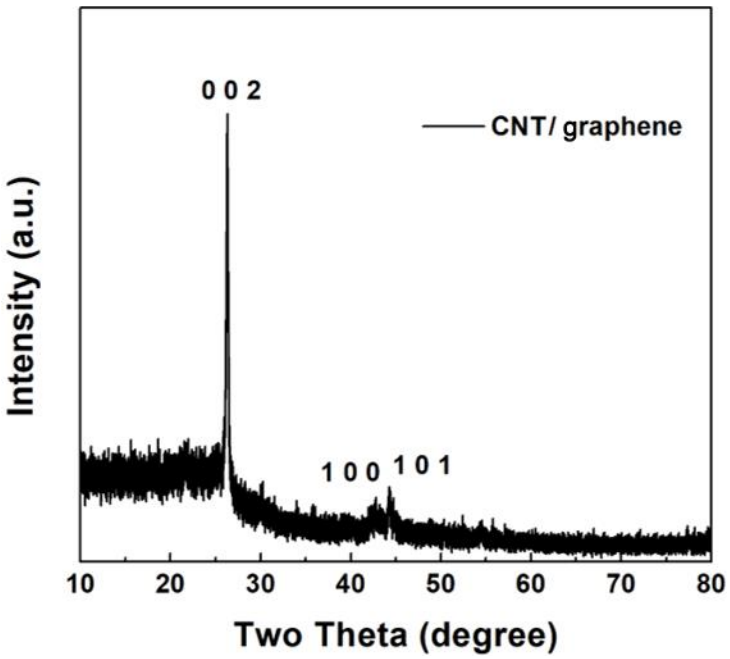

Figure 5.4. XRD pattern of the CNT/graphene material.

The CNT growth started with carbon buds where K and P were detected (**Figure 5.5**). K was thought as the main catalytic element in yeast, whereas P was suspected to be irrelevant in the catalytic process since it was homogeneously distributed [47]. To explore the function of P, point elemental detections were conducted along individual CNTs (**Figure 5.6**f). Clearly, both K and P are proportional to the distance from the tips of the CNTs, indicating that not only K but also P could have provided catalytic functions to the CNT growth. Moreover, the concentrations of K and P have a constant atomic ratio of around 1.5:1, and no other element was detected except for C and O. Therefore, it is rational to believe that the true catalyst in yeast is a mixture of K_2HPO_4 and KH_2PO_4 with K to P atomic ratio of 1.5:1, which are commonly used in yeast production [48]. Since K_2HPO_4 and KH_2PO_4 both have low melting points, during the catalytic process, they melted on the graphene sheet surface to provide beds for carbon atoms to deposit and precipitate out into tubular CNTs. A study [49] suggests that tubular CNTs are usually synthesized when catalysts are in the liquid form whereas bamboo-like CNTs are formed when catalysts are in the solid form. The obtained CNTs (**Figure 5.6**c) exhibited tubular structure, suggesting that the catalysts were in liquid form when the reaction happened, which explained why solid catalyst particles were not found in the obtained CNTs.

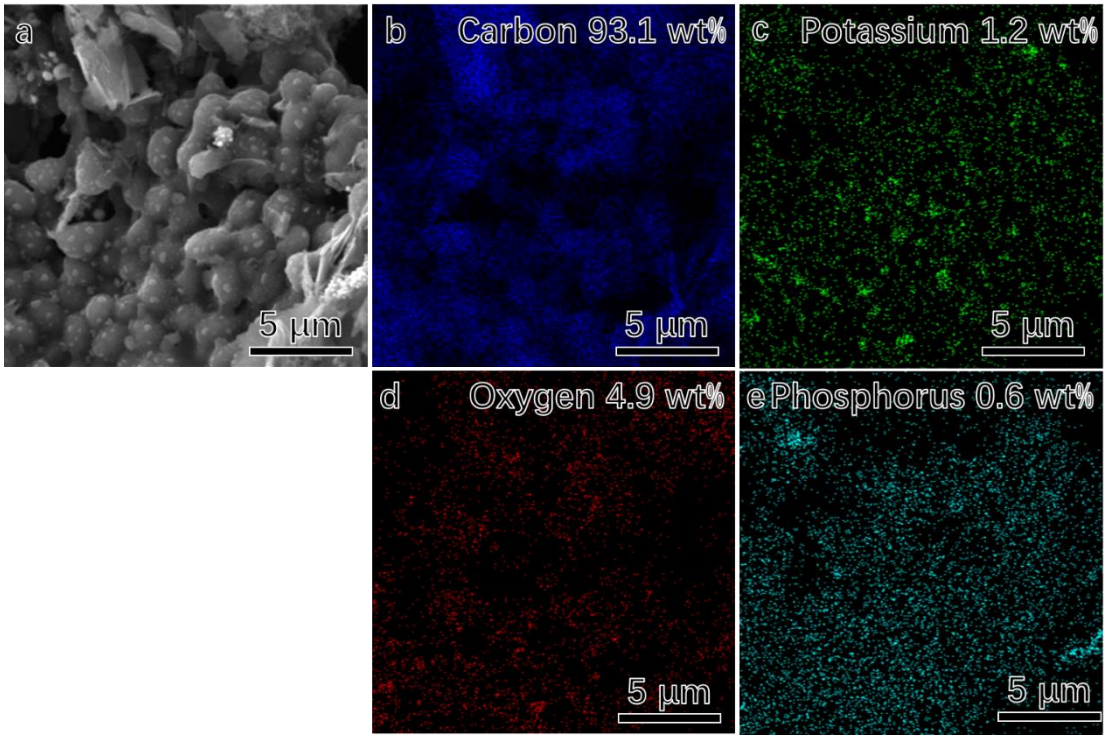

Figure 5.5. EDS maps of CNT buds on yeast/graphene. (a) SEM image of the CNT buds. (b) Carbon map of the CNT buds. (c) Potassium map of the CNT buds. (d) Oxygen map of the CNT buds. (e) Phosphorus map of the CNT buds.

MD simulations (**Figure 5.7**) unveiled that only P was able to stimulate CNT growth, suggesting that P probably provided the catalytic function whereas K could serve other functions. This conclusion is reported for the first time and different from the previous study, where K was considered the catalyst [47]. It is worth noticing that the catalytic function of P only happens when P is doped in the graphene matrix. The P doping can be evidenced by the X-ray photoelectron spectroscopy (XPS) data published elsewhere, where a peak between the C-O peak (286.2 eV) and the C-C peak (284.7 eV) was neglected by the author, which related to the C-P bond [50]. Therefore, the CNT growth can be grouped into four stages: 1) P-containing salts from yeast were deposited on graphene, 2) P-containing salts melted when temperature rose up, 3) P doped into the graphene matrix after melting, and 4) doped P atoms captured carbon atoms from the carrier gas to form CNTs. When only carbon atoms were used in the model (a control model), no CNT formed, suggesting that only P-doped graphene can stimulate CNT growth. As an example, the twelve P atoms in graphene matrix yielded a multilayer CNT (**Figure 5.6**g). Most P atoms remained at the bottom of the CNT as experimentally observed (**Figure 5.6**f**)**. Sectional

views (**Figure 5.6**g) showed a series of similar concentric rings, which were also experimentally seen under TEM (**Figure 5.6**e). The CNT walls consist mostly of C-hexagons (126) with a small number of C-pentagons (47) and C-heptagons (26) (**Figure 5.6**h). An inverse FFT (IFFT) image of the as-grown CNT (**Figure 5.8**) exhibited a similar structure that contained 239 C-hexagons and 33 C-pentagons and 27 C-heptagons (**Figure 5.6**h), which are in consistent with the simulation results.

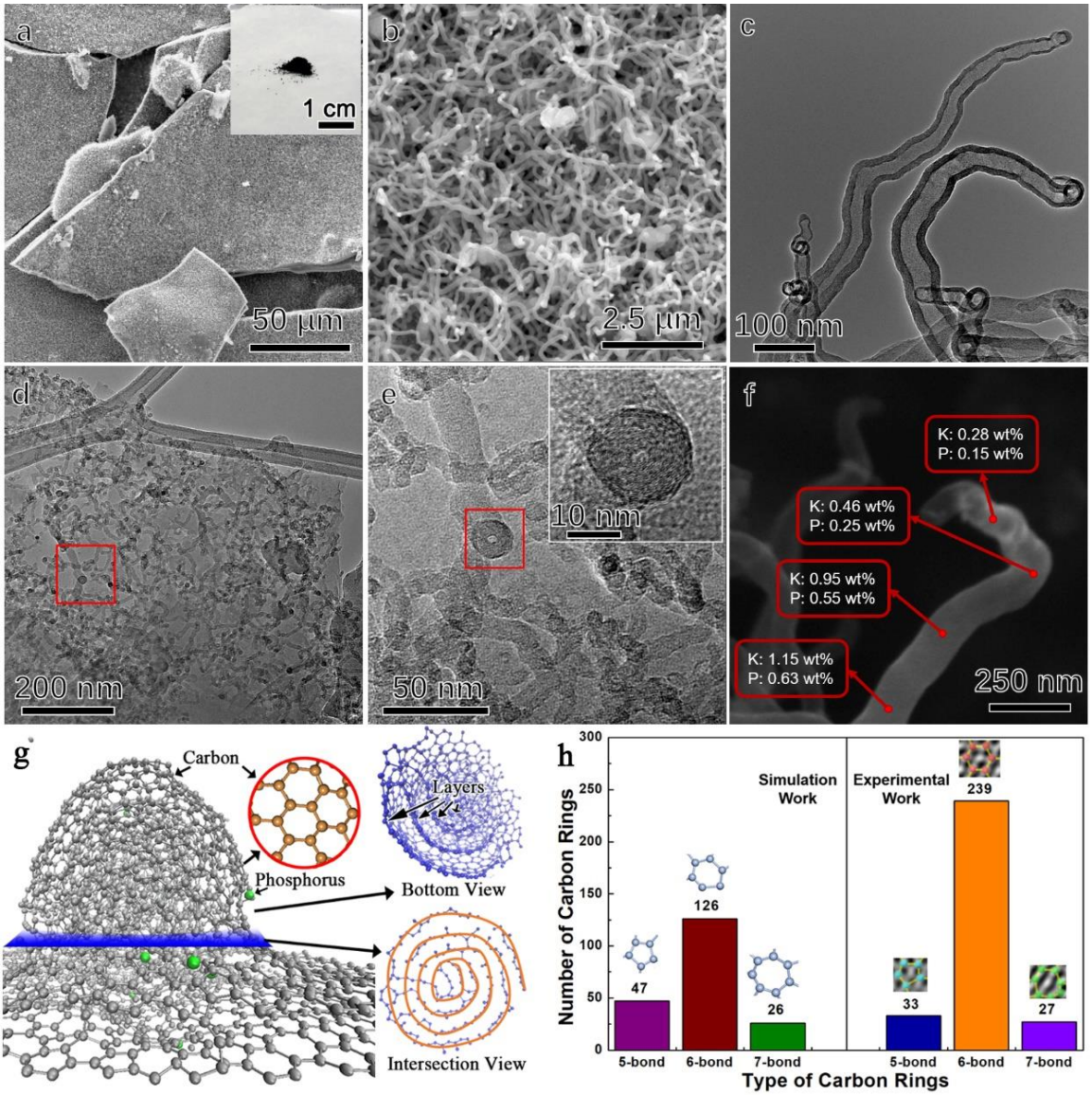

Figure 5.6. Characterization and modeling of growing CNTs on graphene. (a) SEM image of the CNT/graphene hybrid nanostructures (inset: CNT/graphene hybrid powders). (b) High-resolution SEM image of the CNT/graphene hybrid nanostructures. (c) TEM image of the as-obtained CNTs. (d) TEM image of the CNTs on graphene sheets. (e) High-resolution TEM image of the CNTs on

graphene sheets (inset: high-resolution TEM image of the joint between the CNT and graphene). (f) Point elemental detections of a CNT. (g) MD simulations showing CNT growth on graphene with P as the catalyst. (h) Number of different carbon rings of the simulated outer CNT wall layer from the MD simulations and experimentally measured carbon rings from a randomly chosen area of a CNT wall.

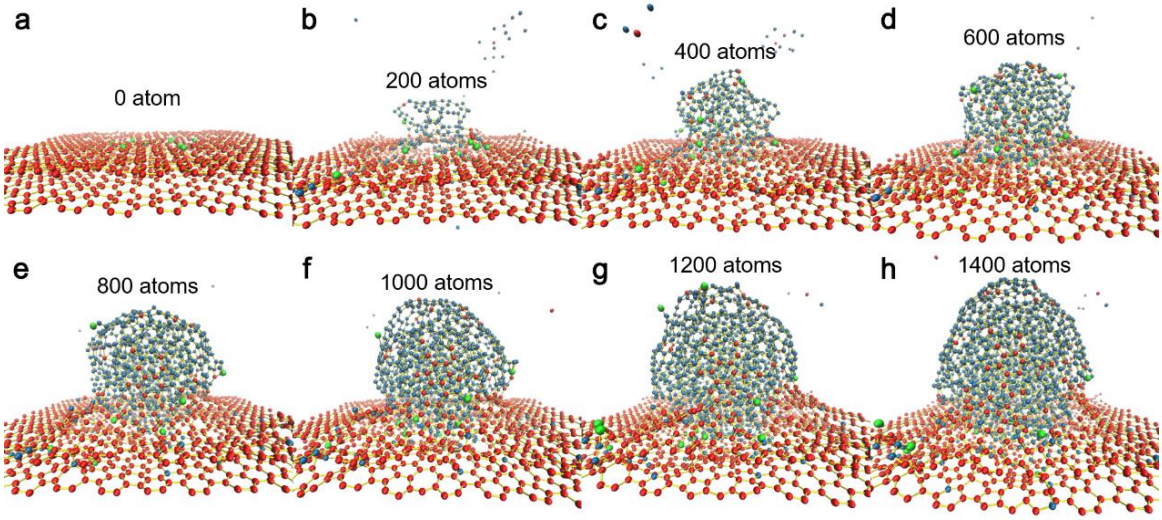

Figure 5.7. MD simulations of CNT growth with double-layer graphene as substrate and phosphorus as catalyst (Green: phosphorus, red: original carbon, blue: inserted carbon). (a) Initial model. (b) Model with 200 carbon atoms inserted. (c) Model with 400 carbon atoms inserted. (d) Model with 600 carbon atoms inserted. (e) Model with 800 carbon atoms inserted. (f) Model with 1000 carbon atoms inserted. (g) Model with 1200 carbon atoms inserted. (h) Model with 1400 carbon atoms inserted.

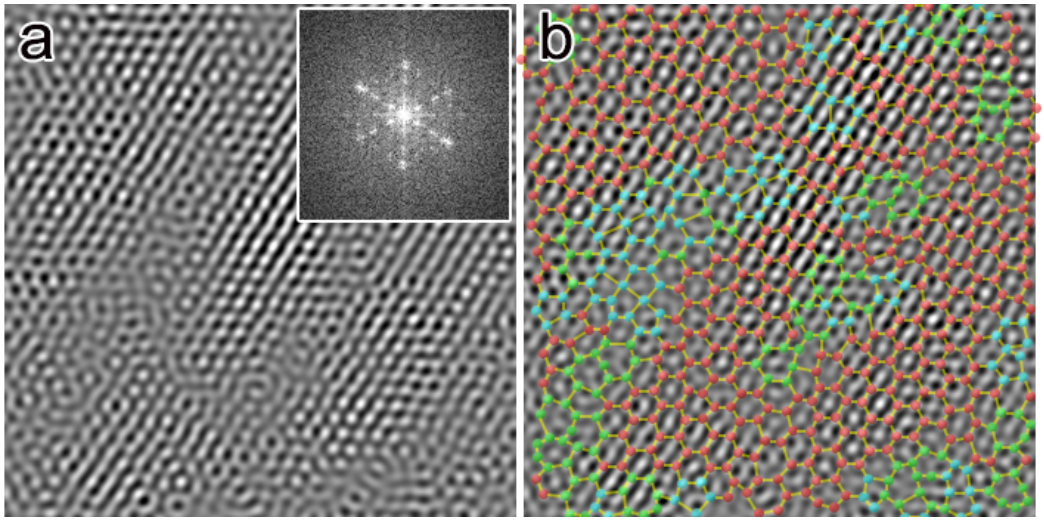

Figure 5.8. Different types of carbon rings on a randomly chosen area of a CNT wall. (a) Inverse

FFT image of a defective CNT wall (inset: FFT image). (b) Highlighted inverse FFT image of different carbon rings (Blue: C-pentagon, red: C-hexagon, green: C-heptagon).

5.3.3 Electrochemical characterization and discussion

The CNT/graphene hybrid nanostructures loaded with sulfur was used to construct the Li-S battery cathode with a piece of polypropylene separator and a piece of Li metal anode. For comparison, commercial graphite, recycled graphite, and upcycled graphene were also loaded with sulfur to construct reference Li-S battery cathodes. The CNT/graphene battery showed a typical charge/discharge cycle with obvious double stages during discharge at a current rate of 0.5 C (**Figure 5.12**a). During discharging, four stages were observed denoting I through IV to describe the transformation of solid sulfur to S_8^{2-} (stage I), S_8^{2-} to S_6^{2-} and S_4^{2-} (stage II), S_4^{2-} to Li_2S_2 (stage III), and Li_2S_2 to Li_2S (stage IV). For charging, three stages appear to occur denoting V, VI, and VII to exposit the conversion of Li_2S to low-order polysulfides (stage V), low-order to high-order polysulfides (stage VI), and high-order polysulfides to solid sulfur (stage VII). These stages can be corresponded to the peaks in the CV curves of the CNT/graphene battery (**Figure 5.12**b).

The CV tests were carried out on the CNT/graphene battery (**Figure 5.12**b) and the reference batteries (**Figure 5.9** a, b, and c) before cycling, at the 5^{th} cycle, 50^{th} cycle, and 200^{th} cycle. All CV curves possess two peaks in the cathodic curve and one peak in the anodic curve without any abnormal peaks, indicating common Li-S battery cycling behaviors without side reactions. The peaks (1) and (2) in the cathodic curve correspond respectively to the second plateau (stage III) and the first plateau (stage I) in the typical charge/discharge cycle. The peaks (3) in the anodic curve correspond to stages V and VI in the typical charge/discharge cycle. The peak intensities of the CNT/graphene battery first drastically decrease and then increase, which matches the battery cycling performance (**Figure 5.12**e). Comparing the peak positions and intensities of all the batteries, the CNT/graphene battery is comparable with the commercial graphite battery, and better than the recycled graphite battery and the upcycled graphene battery. This is probably because the structure of the CNT/graphene hybrid was restored during the high-temperature treatment, which enabled better stability than the recycled graphite and upcycled graphene. EIS testing was conducted on the CNT/graphene battery (**Figure 5.12**c) and the reference batteries (**Fig. 5.9** d, e, and f) to further study the functionality of CNT/graphene hybrid in

its Li-S battery. All EIS tests were performed when the batteries were fully charged. For each battery, the impedance data before cycling, at the 5^{th} cycle, 50^{th} cycle, and 200^{th} cycle were studied. Most EIS patterns, including the test on batteries before cycling, exhibited two semicircles at the high-frequency regime and intermediate-frequency regime and a straight line at the low-frequency regime. All newly assembled batteries were stood for 6 hours before testing, during which solid electrolyte interface (SEI) started to form. This was the reason for several fresh batteries showing the two-semicircle pattern. The intercept between the first semicircle and the x-axis can be denoted as R_{int}, which is the internal resistance contributed by the electrodes, the electrolyte, and the interfaces between them. The first semicircle at the high-frequency regime can be noted as a resistor and a capacitor, where the resistor can be written as R_{SEI}, which is the resistance of Li ions passing through the SEI. The second semicircle at the intermediate-frequency regime can also be identified as a resistor and a capacitor, of which the resistor is known as R_{ct}, which is the charge-transfer resistance. Both resistances can be obtained by calculating the diameters of the semicircles. The straight line at the low-frequency regime is the Warburg impedance, which corresponds to the ion diffusion-limited condition. All batteries exhibited big semicircles before cycling, indicating the existence of passivation layers on some of the Li metal anodes blocking Li-ions and electrons. After cycling, the semicircles largely diminished, illustrating the removal of these passivation layers. Overall, the CNT/graphene battery exhibited the surprisingly low and stable R_{SEI} comparing with the rest of the batteries, meaning that the formation of SEI on CNT/graphene cathode was efficient and of high quality. The comparable R_{int} and R_{CT} of the CNT/graphene battery with the commercial graphite battery also illustrated the good electrochemical quality of the CNT/graphene material.

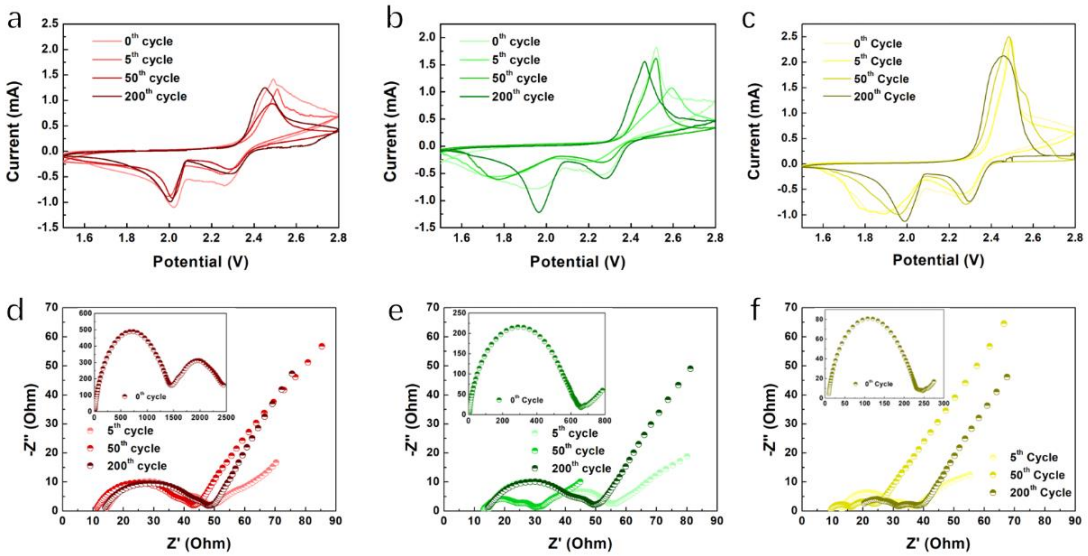

Figure 5.9. CV and EIS curves of reference batteries. (a) CV curves of the commercial graphite battery at the 0th, 5th, 50th, and 200th cycles. (b) CV curves of the recycled graphite battery at the 0th, 5th, 50th, and 200th cycles. (c) CV curves of the upcycled graphene battery at the 0th, 5th, 50th, and 200th cycles. (d) EIS plot of the commercial graphite battery at the 0th, 5th, 50th, and 200th cycles. (e) EIS plot of the recycled graphite battery at the 0th, 5th, 50th, and 200th cycles. (f) EIS plot of the upcycled graphene battery at the 0th, 5th, 50th, and 200th cycles.

Table 5.3. Curve fit data of EIS tests.

	Commercial graphite			Recycled graphite			Upcycled graphene			CNT/graphene		
	5th	50th	200th	5th	50th	200th	5th	50th	200th	5th	50th	200th
R_{int} (Ohm)	14.33	10.92	13.37	14.69	12.94	14.25	13.05	9.481	18.13	12.4	11.08	13.75
R_{SEI} (Ohm)	25.68	26.74	24.95	25.06	10.85	28.34	15.96	6.378	13.4	9.576	8.01	8.764
R_{CT} (Ohm)	5.628	5.043	8.654	13	5.196	7.425	5.343	8.054	7.307	6.71	13.99	3.625

To quantify impedance changes, curve fitting was performed to the EIS data at the 5th cycle, 50th cycle, and 200th cycle (**Figure 5.10**), and the results are summarized in **Table 5.3**. All R_{int} values are stable and similar, indicating that the CNT/graphene would not increase the internal resistance. The R_{SEI} values were calculated following [51],

$$R_{SEI} = \frac{\rho l}{S} \tag{5.2}$$

where ρ is the conductivity of the SEI layer, l is the thickness, and S is the surface area. All batteries had similar SEI conductivities and thicknesses since they all used the same electrolyte and active materials, indicating that the R_{SEI} is inversely proportional to the surface area. Compared with graphene-based batteries, the commercial graphite battery and recycled graphite battery exhibited higher R_{SEI} because graphite has smaller surface area

than graphene. Between the graphene-based batteries, the upcycled graphene battery has higher R_{SEI} than the CNT/graphene battery because the CNTs contributed extra surface areas. The recycled graphite battery and upcycled graphene battery exhibited significant R_{SEI} instability (25.06 Ω to 10.85 Ω to 28.34 Ω) and (15.96 Ω to 6.378 Ω to 13.4 Ω), respectively, which could be ascribed to that both recycled graphite and upcycled graphene were structurally damaged due to previous battery operations and recycling/upcycling process. Therefore, the SEI layers formed on the recycled graphite and upcycled graphene were unstable, leading to the observed variations. The high-temperature treatments were able to heal the damaged structure as seen in the CNT/graphene battery which did not show such variation. These conclusions can also be used to explain the Coulombic efficiency of the batteries, which will be discussed in the cycling performance section. The R_{ct} values were calculated following [52],

$$R_{ct} = \frac{RT}{F^2 A k_s x^{0.5}(1-x)^{0.5}} \tag{5.3}$$

where R is the molar gas constant, T is the absolute temperature, F is the Faraday constant, A is the total electroactive surface area, k_s is the standard exchange rate constant, and x is the intercalation level. As all the batteries were in fully charged status, they had similar x (approaching 0) and Tvalues. Therefore, the only changeable term is the total electroactive surface area A, which is related to the passivation layer thickness and potential difference. In most observed cases, the R_{ct} values slightly decreased and then slightly increased because the passivation layers on the electrodes were thinner (higher A) in the initial stabilization stage and then became thicker (lower A) in the accumulation stage. However, the upcycled graphene battery and the CNT/graphene battery showed an initial increase and then decrease in R_{ct}, which was probably ascribed to the uneven distribution of the passivation layers, resulting in an abnormally low value. The uneven distribution of the passivation layers in turn led to large polarizations in these two batteries, which were seen in their CV patterns.

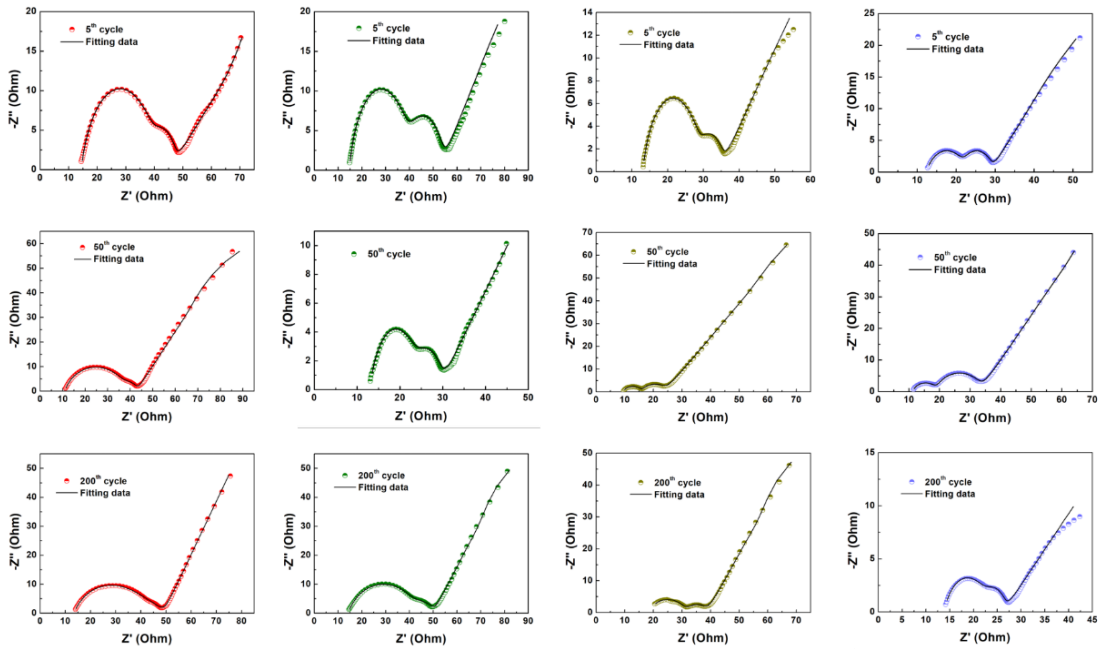

Figure 5.10. Curve fitting patterns of the EIS data of the batteries at the 5th, 50th, and 200th cycles. Red: the commercial graphite battery; Green: the recycled graphite battery; Yellow: the upcycled graphene battery; Blue: the CNT/graphene battery.

Rate abilities of all the batteries were tested after running 100 cycles for stabilization. Current rates of 0.2 C, 0.4 C, 0.8 C, and 1.6 C were used in this study (**Figure 5.12**d). Among all batteries, the recycled graphite battery exhibited the highest retention rate (64.54% from 649.836 mAh g^{-1} to 419.418 mAh g^{-1}) when the current rate was octupled from 0.2 C to 1.6 C because the layers that were previously expanded before recycling were able to tolerate large sulfur volume expansion even at a high current rate [53]. The upcycled graphene battery showed the lowest retention rate (36.12% from 701.185 mAh g^{-1} to 253.271 mAh g^{-1}) when the same current rate increment was applied. This was because graphene could not buffer sulfur volume change [23,54]. The CNT/graphene battery revealed a retention rate of 57.33% from 737.88 mAh g^{-1} to 423 mAh g^{-1}, which is higher than the commercial graphite battery (53.14% from 539.64 mAh g^{-1} to 286.752 mAh g^{-1}). This indicates that CNTs on graphene were able to accommodate sulfur volume expansion more effectively than pure graphite [55,56]. Additionally, the CNT/graphene battery exhibited higher specific capacities than other batteries since the CNTs were capable of loading more sulfur. The specific capacities of all the batteries were fully recovered when the operation rate returned to 0.8 C.

Table 5.4. Battery performance of CNT/graphene batteries using different methods and graphene types.

No.	Initial Capacity	Fading Rate	Lifespan	Sulfur Loading	Columbic Efficiency	Method	Graphene Type	Ref.
1	1121 mAh g^{-1}	0.120%	150	77 wt%	91.0%	CVD	Graphene	28
2	1048 mAh g^{-1}	0.041%	1000	50 wt%	99.0%	Mix	Graphene	57
3	1152 mAh g^{-1}	0.300%	80	1.0 mg cm^{-2}	N/A	CVD	Graphene	58
4	1299 mAh g^{-1}	0.484%	100	75 wt%	98.0%	Mix	rGO	59
5	1040 mAh g^{-1}	0.310%	100	4.5-5.5 mg cm^{-2}	96.0%	Mix	rGO	60
6	1084 mAh g^{-1}	0.055%	800	3.3 mg cm^{-2}	97.0%	Mix	Graphene	61
7	1067 mAh g^{-1}	0.240%	100	2.0 mg cm^{-2}	95.0%	Mix	Graphene	62
8	948 mAh g^{-1}	0.185%	200	4.0 mg cm^{-2}/50 wt%	94.4%	Mix	Graphene	63
9	1179.6 mAh g^{-1}	0.085%	200	80.1 wt%	91.0%	Mix	rGO	64
Ours	1151.2 mAh g^{-1}	0.042%	1500	2.18 mg cm^{-2}/64.9 wt%	97.0%	Pyrolysis	Graphene	

The CNT/graphene battery with a sulfur loading of 2.18 mg cm^{-2} (64.9 wt%) exhibited an initial discharge capacity of 1,151.2 mAh g^{-1} with a lifespan over 1,500 times at a current rate of 0.5 C (**Figure 5.12**e). For comparison, the commercial graphite battery, recycled graphite battery, and upcycled graphene battery with respective sulfur loading of 1.84 mg cm^{-2} (44.6 wt%), 1.87 mg cm^{-2} (43.2 wt%), and 2.13 mg cm^{-2} (47.7 wt%) were also tested (**Figure 5.11**). The initial capacities were found to be proportional to the sulfur contents in the electrodes (**Figure 5.13**a). It is worth noting that all the carbon-based cathode materials were mixed with the same amount of sulfur with a carbon/sulfur mass ratio of 1:2, yet only the CNT/graphene hybrid could achieve 64.9 wt% sulfur loading whereas others could only hold no more than 48 wt% sulfur. This indicates that the CNTs on graphene provided extra room to load more sulfur. As the result, the commercial graphite battery failed at the 926th cycle, which is much longer than the recycled graphite battery's 405 cycles and the upcycled graphene battery's 519 cycles, yet shorter than the CNT/graphene's 1,500 cycles. Upon growing CNTs on graphene, the graphene's defects were healed and the CNTs were able to accommodate sulfur volume change, jointly rendering the battery with a much longer lifespan. Compared with other CNT/graphene Li-S batteries, our 1,500-cycle lifespan is still the longest (**Table 5.4**). The commercial graphite battery and CNT/graphene battery were found to be more stable than the recycled graphite battery and the upcycled graphene battery. The CNT/graphene battery exhibited a capacity fading rate of only 0.042% per cycle, which is lower than the commercial graphite battery (0.047%

per cycle), the recycled graphite battery (0.188% per cycle), and the upcycled graphene battery (0.090% per cycle). This result is also better than most of the CNT/graphene Li-S batteries (**Table 5.4**). The Coulombic efficiency revealed intriguing findings. The Coulombic efficiency is largely related to the distribution of Li ions during operation, which are one of the necessary ions to form SEI layers [65]. Owing to the damaged structures of the cathodes in the recycled graphite battery and the upcycled graphene battery, the SEI layers on the cathodes were also unstable, leading to lower and more fluctuated Coulombic efficiencies than the commercial graphite battery and CNT/graphene battery, in consistent with the R_{SEI} results from the EIS section, where the R_{SEI} values of the recycled graphite battery and upcycled graphene battery were varied with cycle number. Additionally, because the CNT/graphene battery has the lowest R_{SEI}, its Coulombic efficiency was the highest and maintained above 97% during its entire lifespan.

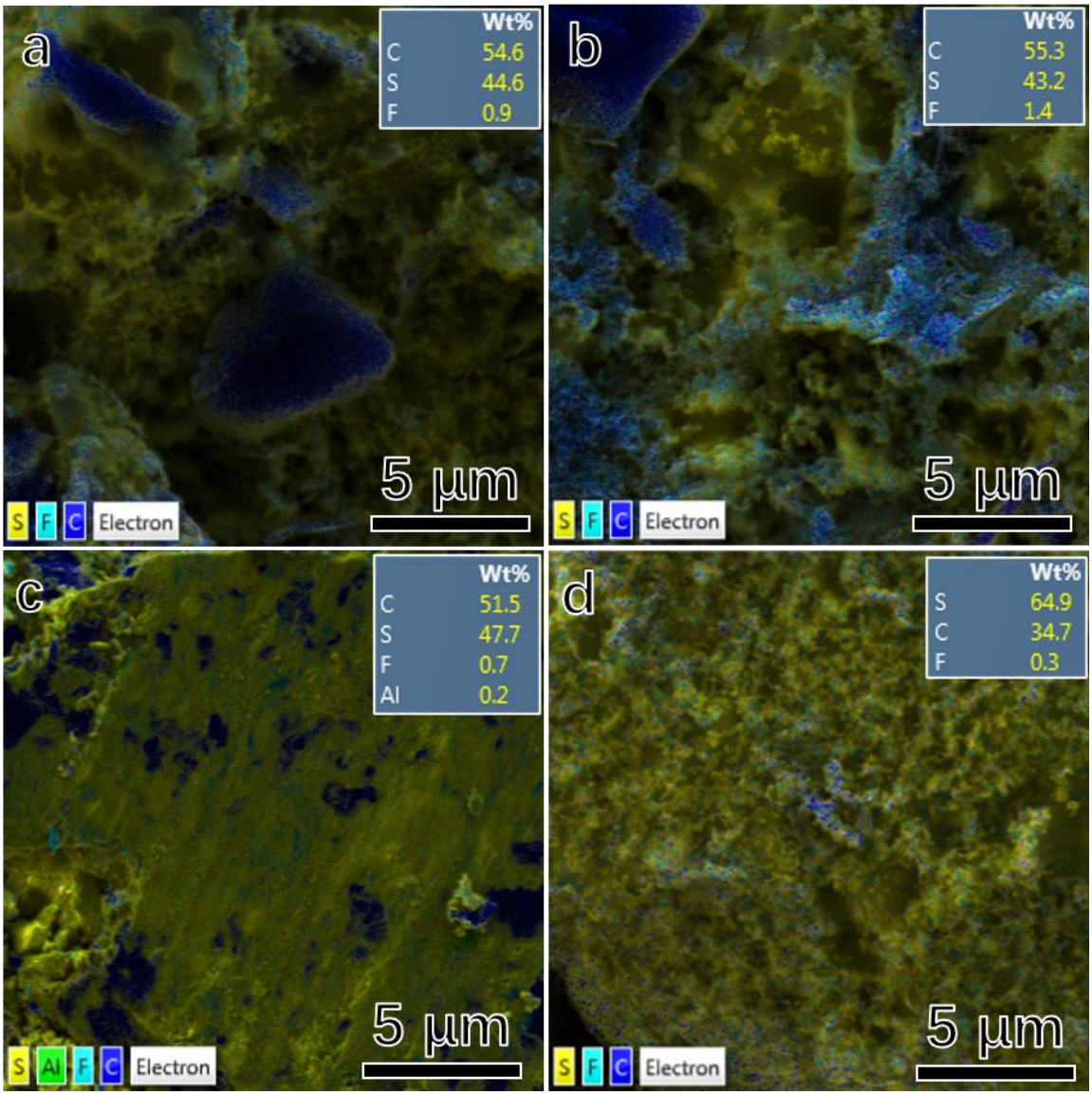

Figure 5.11. EDS maps of all cathodes. (a) EDS map of the sulfur-infiltrated commercial graphite cathode. (b) EDS map of the sulfur-infiltrated recycled graphite cathode. (c) EDS map of the sulfur-infiltrated upcycled graphene cathode. (d) EDS map of the sulfur-infiltrated CNT/graphene cathode.

Polarization potentials of the CNT/graphene battery and the commercial graphite battery were collected to evaluate the level of polarization within these batteries (**Figure 5.13**b). A large polarization of 0.64 V was detected at the first cycle of the commercial graphite battery, which is much larger than that of the CNT/graphene battery's 0.34 V. During the entire lifetime of the commercial graphite battery, the polarization was also stronger than the CNT/graphene battery, which indicated that the reaction rate and the ion diffusion rate in the electrolyte of the CNT/graphene battery were much higher than the

commercial graphite battery. This evidenced that the CNT/graphene composite possessed better interfaces to facilitate sulfur reactions and connect the sulfur and the electrolyte, agreeing well with the expected functionality of the CNT/graphene hybrid.

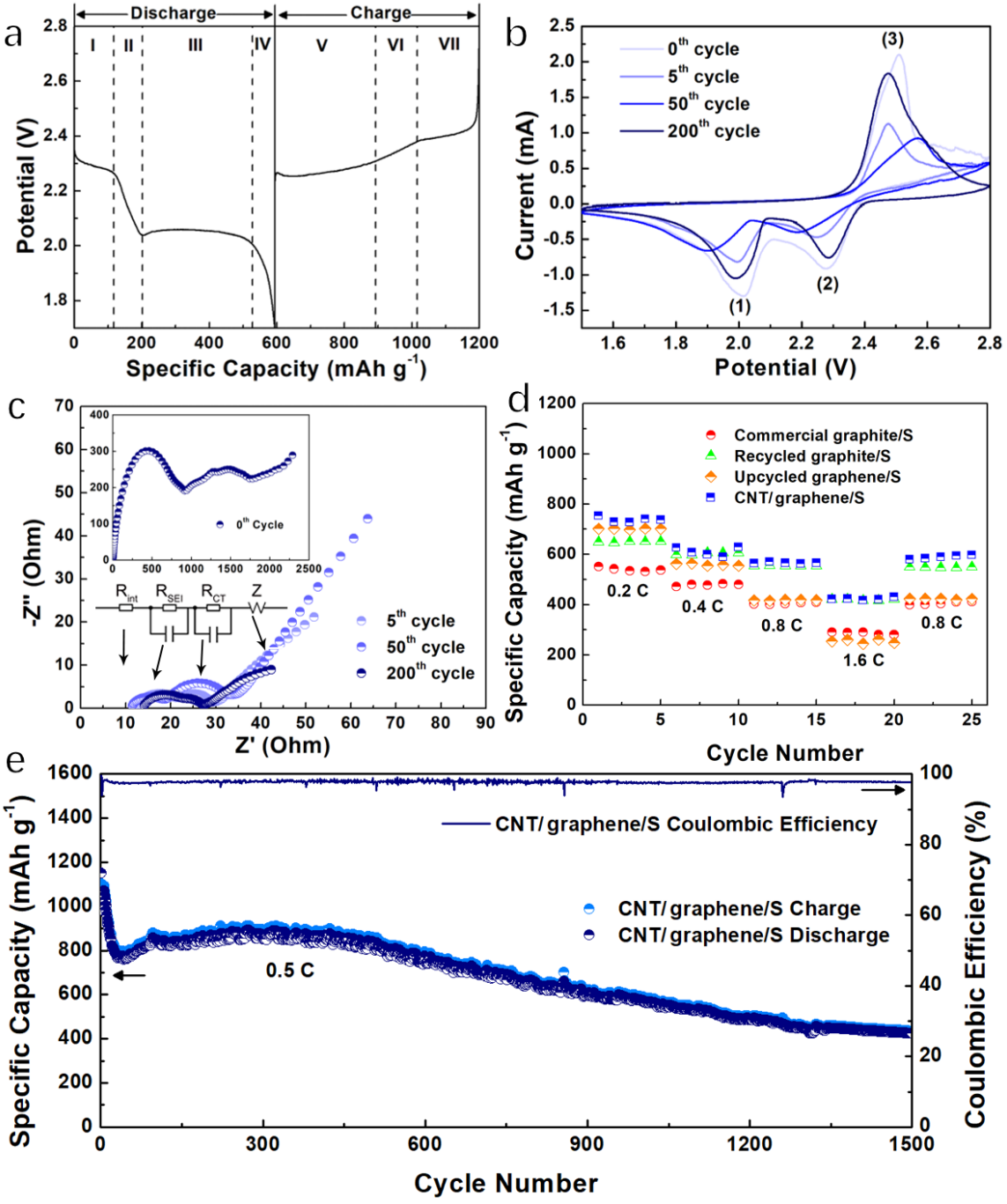

Figure 5.12. Characterization of battery performance. (a) Charge/discharge cycle of the CNT/graphene battery. (b) CV curves of the CNT/graphene battery. (c) EIS patterns of the CNT/graphene battery (inset: equivalent circuit of the patterns). (d) Rate performances of the

CNT/graphene battery and the reference batteries. (e) Cycling performance of the CNT/graphene battery.

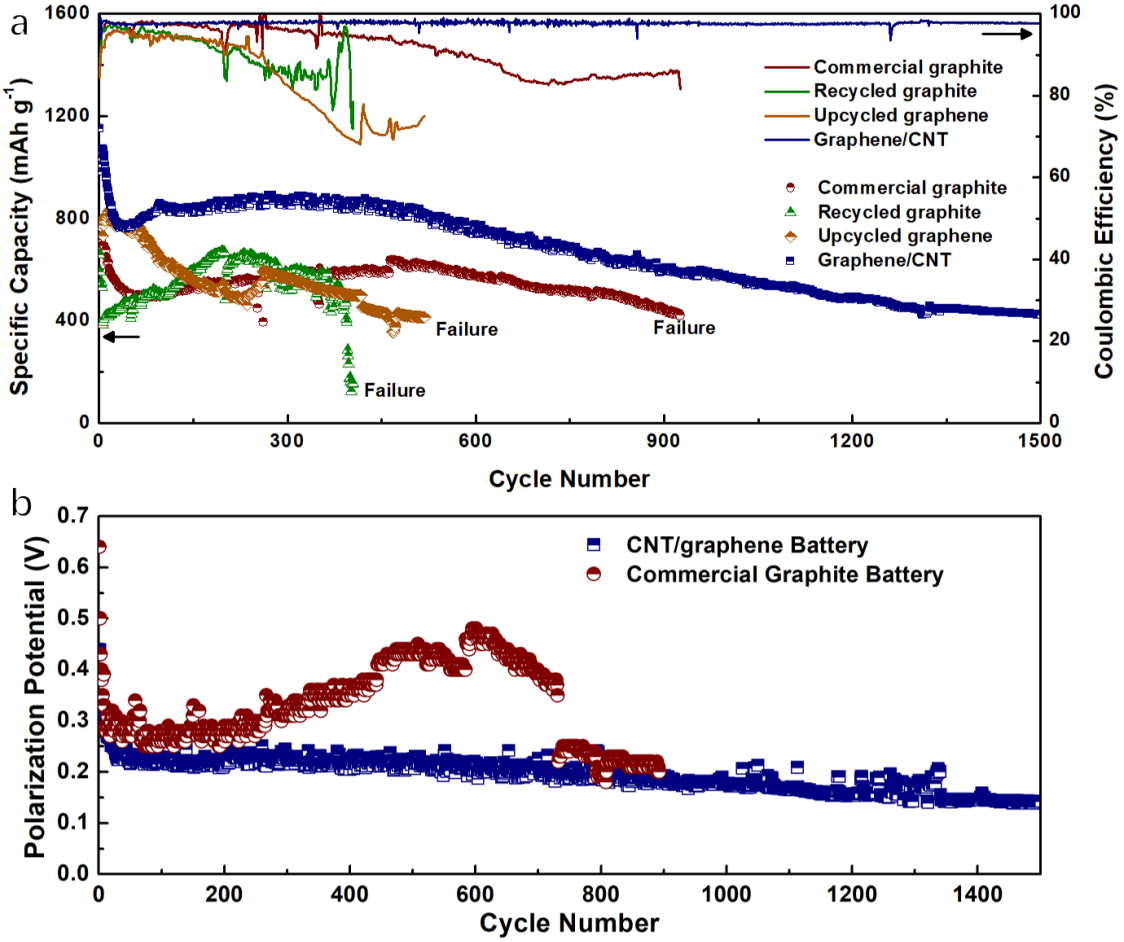

Figure 5.13. (a) Discharge cycling performances and Coulombic efficiencies of the batteries studied. (b) Polarization potential of the CNT/graphene battery and the commercial graphite battery.

5.4 Conclusions

End-of-life Li-ion battery anode graphite found its second life in Li-S battery cathodes by upcycling the anode graphite into graphene which was then used as the substrate to grow CNTs by pyrolyzing cotton as the carbon source and yeast as the catalyst to form CNT/graphene nanostructures. In the sulfur infiltrated CNT/graphene cathodes, the graphene provided a highly conductive network while the CNTs enabled high sulfur loading and volume buffering, rendering the battery with high capacity, high stability, and long lifespan. Additionally, the CNT/graphene nanostructures should find applications in an extensive range of fields such as reinforcements in composites. The all-green CNT/graphene hybrids present new pathways to circular economy.

Reference

[1] D. D. Lecce, R. Verrelli, and J. Hassoun, Lithium-Ion Batteries for Sustainable Energy Storage: Recent Advances towards New Cell Configurations, *Green Chemistry* 19 (2017) 3442-3467.

[2] C. Friebe, A. Lex-Balducci, and U. S. Schubert, Sustainable Energy Storage: Recent Trends and Developments toward Fully Organic Batteries, *ChemSusChem* 12 (2019) 4093-4115.

[3] A. R. Dehghani-Sanij, E. Tharumalingam, M. B. Dusseault, and R. Fraser, Study of Energy Storage Systems and Environmental Challenges of Batteries, *Renewable and Sustainable Energy Reviews* 109 (2019) 192-208.

[4] F. H. Gandoman, J. Jaguemont, S. Goutam, R. Gopalakrishnan, Y. Firouz, T. Kalogiannis, N. Omar, and J. V. Mierlo, Concept of Reliability and Safety Assessment of Lithium-Ion Batteries in Electric Vehicles: Basics, Progress, and Challenges, *Applied Energy* 251 (2019) 113343.

[5] A. Eftekhari, Lithium Batteries for Electric Vehicles: from Economy to Research Strategy, *ACS Sustainable Chemistry & Engineering* 7 (2019) 5602-5613.

[6] X. Zeng, M. Li, D. A. El-Hady, W. Alshitari, A. S. Al-Bogami, J. Lu, and K. Amine, Commercialization of Lithium Battery Technologies for Electric Vehicles, *Advanced Energy Materials* 9 (2019) 1900161.

[7] G. Harper, R. Sommerville, E. Kendrick, L. Driscoll, P. Slater, R. Stolkin, A. Walton, P. Christensen, O. Heidrich, S. Lambert, A. Abbott, K. Ryder, L. Gaines, and P. Anderson, Recycling Lithium-Ion Batteries from Electric Vehicles, *Nature* 575 (2019) 75-86.

[8] E. Fan, L. Li, Z. Wang, J. Lin, Y. Huang, Y. Yao, R. Chen, and F. Wu, Sustainable Recycling Technology for Li-Ion Batteries and Beyond: Challenges and Future Prospects, *Chemical Reviews* 120 (2020) 7020-7063.

[9] Y. Song, W. Cai, L. Kong, J. Cai, Q. Zhang, and J. Sun, Rationalizing Electrocatalysis of Li–S Chemistry by Mediator Design: Progress and Prospects, *Advanced Energy Materials* 10 (2020) 1901075.

[10] V. Knap, D. I. Stroe, M. Swierczynski, R. Purkayastha, K. Propp, R. Teodorescu, and E. Schaltz, A Self-Discharge Model of Lithium-Sulfur Batteries Based on Direct Shuttle Current Measurement, *Journal of Power Sources* 336 (2016) 325-331.

[11] Y. Ansari, S. Zhang, B. Wen, F. Fan, and Y. M. Chiang, Stabilizing Li–S Battery Through Multilayer Encapsulation of Sulfur, *Advanced Energy Materials* 9 (2019) 1802213.

[12] A. Fedorková, R. Oriňáková, O. Čech, and M. Sedlaříková, New Composite Cathode Materials for Li/S Batteries: a Review, *International Journal of Electrochemical Science* 8 (2013) 10308-10319.

[13] Y. Deng, J. Li, T. Li, X. Gao, and C. Yuan, Life Cycle Assessment of Lithium Sulfur Battery for Electric Vehicles, *Journal of Power Sources* 343 (2017) 284-295.

[14] M. Shaibani, M. S. Mirshekarloo, R. Singh, C. D. Easton, M. C. D. Cooray, N. Eshraghi, T. Abendroth, S. Dörfler, H. Althues, S. Kaskel, A. F. Hollenkamp, M. R. Hill, and M. Majumder, Expansion-Tolerant Architectures for Stable Cycling of Ultrahigh-Loading Sulfur Cathodes in Lithium-Sulfur Batteries, *Science Advances* 6 (2020) eaay2757.

[15] N. Nitta, F. Wu, J. T. Lee, and G. Yushin, Li-Ion Battery Materials: Present and Future, *Materials Today* 18 (2015) 252-264.

[16] E. M. S. Barbieri, E. P. C. Lima, M. F. F. Lelis, and M. B. J. G. Freitas, Recycling of Cobalt from Spent Li-Ion Batteries As β-$Co(OH)_2$ and the Application of Co_3O_4 As a Pseudocapacitor, *Journal of Power Sources* 270 (2014) 158-165.

[17] C. Lupi, M. Pasquali, and A. Dell'Era, Nickel and Cobalt Recycling from Lithium-Ion Batteries by Electrochemical Processes, *Waste Management* 25 (2005) 215-220.

[18] S. Vishvakarma and N. Dhawan, Recovery of Cobalt and Lithium Values from Discarded Li-Ion Batteries, *Journal of Sustainable Metallurgy* 5 (2019) 204-209.

[19] L. Zhang, K. Shen, W. He, Y. Liu, and S. Guo, SiO_2@Graphite Composite Generated from Sewage Sludge As Anode Material for Lithium Ion Batteries, *International Journal of Electrochemical Science* 12 (2017) 10221-10229.

[20] Y. Zhang, N. Song, J. He, R. Chen, and X. Li, Lithiation-Aided Conversion of End-of-Life Lithium-Ion Battery Anodes to High-Quality Graphene and Graphene Oxide, *Nano Letters* 19 (2019) 512-519.

[21] M. D. Stoller, S. Park, Y. Zhu, J. An, and R. S. Ruoff, Graphene-Based Ultracapacitors, *Nano Letters* 8 (2008) 3498-3502.

[22] D. G. Papageorgiou, I. A. Kinloch, and R. J. Young, Mechanical Properties of Graphene and Graphene-Based Nanocomposites, *Progress in Materials Science* 90 (2017) 75-127.

[23] J. R. Miller, R. A. Outlaw, and B. C. Holloway, Graphene Double-Layer Capacitor with Ac Line-Filtering Performance, *Science* 329 (2010) 1637-1639.

[24] Y. Zhao, W. Wu, J. Li, Z. Xu, and L. Guan, Encapsulating MWNTs into Hollow Porous Carbon Nanotubes: a Tube-in-Tube Carbon Nanostructure for High-Performance Lithium-Sulfur Batteries, *Advanced Materials* 26 (2014) 5113-5118.

[25] J. Guo, Y. Xu, and C. Wang, Sulfur-Impregnated Disordered Carbon Nanotubes Cathode for Lithium–Sulfur Batteries, *Nano Letters* 11 (2011) 4288-4294.

[26] R. Carter, L. Oakes, N. Muralidharan, A. P. Cohn, A. Douglas, and C. L. Pint, Polysulfide Anchoring Mechanism Revealed by Atomic Layer Deposition of V_2O_5 and Sulfur-Filled Carbon Nanotubes for Lithium–Sulfur Batteries, *ACS Applied Materials & Interfaces* 9 (2017) 7185-7192.

[27] M. Q. Zhao, X. F. Liu, Q. Zhang, G. L. Tian, J. Q. Huang, W. Zhu, and F. Wei, Graphene/Single-Walled Carbon Nanotube Hybrids: One-Step Catalytic Growth and Applications for High-Rate Li–S Batteries, *ACS Nano* 6 (2012) 10759-10769.

[28] H.J. Peng, J.Q. Huang, M.Q. Zhao, Q. Zhang, X.B. Cheng, X.Y. Liu, W.Z. Qian, and F. Wei, Nanoarchitectured Graphene/CNT@Porous Carbon with Extraordinary Electrical Conductivity and Interconnected Micro/Mesopores for Lithium-Sulfur Batteries, *Advanced Functional Materials* 24 (2014) 2772-2781.

[29] P. Giannozzi, S. Baroni, N. Bonini, M. Calandra, R. Car, C. Cavazzoni, D. Ceresoli, G. L. Chiarotti, M. Cococcioni, I. Dabo, A. Dal Corso, S. De Gironcoli, S. Fabris, G. Fratesi, R. Gebauer, U. Gerstmann, C. Gougoussis, A. Kokalj, M. Lazzeri, L. Martin-Samos, N. Marzari, F. Mauri, R. Mazzarello, S. Paolini, A. Pasquarello, L. Paulatto, C. Sbraccia, S. Scandolo, G. Sclauzero, A. P. Seitsonen, A. Smogunov, P. Umari, and R. M. Wentzcovitch, Quantum Espresso: a Modular and Open-Source Software Project for Quantum Simulations of Materials, *Journal of Physics: Condensed Matter* 21 (2009) 395502.

[30] Y. Yao and Y. Kanai, Plane-Wave Pseudopotential Implementation and Performance of SCAN Meta-GGA Exchange-Correlation Functional for Extended Systems, *The Journal of Chemical Physics* 146 (2017) 224105.

[31] B. G. Pfrommer, M. Cote, S. G. Louie, and M. L. Cohen, Relaxation of Crystals with the Quasi-Newton Method, *Journal of Computational Physics* 131 (1997) 233-240.

[32] S. Plimpton, Fast Parallel Algorithms for Short-Range Molecular Dynamics, *Journal of Computational Physics* 117 (1995) 1-19.

[33] K. Ganeshan, Y. K. Shin, N. C. Osti, Y. Sun, K. Prenger, M. Naguib, M. Tyagi, E. Mamontov, D. Jiang, A. C. T. Duin, Structure and Dynamics of Aqueous Electrolytes Confined in 2D-TiO_2/$Ti_3C_2T_2$ MXene Heterostructures, *ACS Applied Materials & Interfaces* 12 (2020) 58378-58389.

[34] H.J. Liang, B.H. Hou, W.H. Li, Q.L. Ning, X. Yang, Z.Y. Gu, X.J. Nie, G. Wang, and X.L. Xu, Staging Na/K-ion de-/intercalation of graphite retrieved from spent Li-ion batteries: in operando X-ray diffraction studies and an advanced anode material for Na/K-ion batteries, *Energy & Environmental Science* 12 (2019) 3575.

[35] J. Fujita, T. Hiyama, A. Hirukawa, T. Kondo, J. Nakamura, S. Ito, R. Araki, Y. Ito, M. Takeguchi, and W.W. Pai, Near room temperature chemical vapor deposition of graphene with diluted methane and molten gallium catalyst, *Scientific Reports* 7 (2017) 12371.

[36] J. H. Deng, R. N. Liu, Y. Zhang, W. X. Zhu, A. L. Han, and G. A. Cheng, Highly Improved Field Emission from Vertical Graphene–Carbon Nanotube Composites, *Journal of Alloys and Compounds* 723 (2017) 75-83.

[37] J. Jiang, Y. Li, C. Gao, N. D. Kim, X. Fan, G. Wang, Z. Peng, R. H. Hauge, and J. M. Tour, Growing Carbon Nanotubes from Both Sides of Graphene, *ACS Applied Materials & Interfaces* 8(11) (2016) 7356-7362.

[38] K. Kumar, Y. S. Kim, X. Li, J. Ding, F. T. Fisher, and E. H. Yang, Chemical Vapor Deposition of Carbon Nanotubes on Monolayer Graphene Substrates: Reduced Etching via Suppressed Catalytic Hydrogenation Using C_2H_4, *Chemistry of Materials* 25(19) (2013) 3874-3879.

[39] G. Saeed, S. Kumar, N. H. Kim, and J. H. Lee, Fabrication of 3D Graphene-CNTs/α-MoO_3 Hybrid Film As an Advance Electrode Material for Asymmetric Supercapacitor

with Excellent Energy Density and Cycling Life, *Chemical Engineering Journal* 352 (2018) 268-276.

[40] Z. Niu, Y. Zhang, Y. Zhang, X. Lu, and J. Liu, Enhanced Electrochemical Performance of Three-Dimensional Graphene/Carbon Nanotube Composite for Supercapacitor Application, *Journal of Alloys and Compounds* 820 (2020) 153114.

[41] R. V. Salvatierra, D. Zakhidov, J. Sha, N. D. Kim, S. K. Lee, A. R. O. Raji, N. Zhao, and J. M. Tour, Graphene Carbon Nanotube Carpets Grown Using Binary Catalysts for High-Performance Lithium-Ion Capacitors, *ACS Nano* 11(3) (2017) 2724-2733.

[42] S. Riyajuddin, S. Kumar, K. Soni, S. P. Gaur, D. Badhwar, and K. Ghosh, Study of Field Emission Properties of Pure Graphene-CNT Heterostructures Connected via Seamless Interface, *Nanotechnology* 30 (2019) 385702.

[43] K. Liu, Y. Yao, T. Lv, H. Li, N. Li, Z. Chen, G. Qian, and T. Chen, Textile-Like Electrodes of Seamless Graphene/Nanotubes for Wearable and Stretchable Supercapacitors, *Journal of Power Sources* 446 (2020) 227355.

[44] C. Gao, N. D. Kim, R. V. Salvatierra, S. K. Lee, L. Li, Y. Li, J. Sha, G. A. L. Silva, H. Fei, E. Xie, and J. M. Tour, Germanium on Seamless Graphene Carbon Nanotube Hybrids for Lithium Ion Anodes, *Carbon* 123 (2017) 433-439.

[45] J. Xu, Z. Han, J. Wu, K. Song, J. Wu, H. Gao, and Y. Mi, Synthesis and Electrochemical Performance of Vertical Carbon Nanotubes on Few-Layer Graphene As an Anode Material for Li-Ion Batteries, *Materials Chemistry and Physics* 205 (2018) 359-365.

[46] M.Q. Zhao, X.F. Liu, Q. Zhang, G.L. Tian, J.Q. Huang, W. Zhu, and F. Wei, Graphene/Single-Walled Carbon Nanotube Hybrids: One-Step Catalytic Growth and Applications for High-Rate Li–S Batteries, *ACS Nano* 6 (2012) 10759-10769.

[47] Z. Gao, N. Song, Y. Zhang, Y. Schwab, J. He, and X. Li, Carbon Nanotubes Derived from Yeast-Fermented Wheat Flour and Their Energy Storage Application, *ACS Sustainable Chemistry & Engineering* 6 (2018) 11386-11396.

[48] S. V. Kamzolova, I. G. Morgunov, A. Aurich, O. A. Perevoznikova, N. V. Shishkanova, U. Stottmeister, and T. V. Finogenova, Lipase Secretion and Citric Acid Production in Yarrowia Lipolytica Yeast Grown on Animal and Vegetable Fat, *Food Technology and Biotechnology* 43 (2005) 113-122.

[49] K. Bartsch, K. Biedermann, T. Gemming, and A. Leonhardt, On the Diffusion-Controlled Growth of Multiwalled Carbon Nanotubes, *Journal of Applied Physics* 97 (2005) 114301.

[50] J. He, Z. Gao, and X. Li, Yeast-Derived Carbon Nanotube-Coated Separator for High Performance Lithium-Sulfur Batteries, *JOM* 73 (2021) 2516-2524.

[51] F. Orsini, M. Dolle, and J. M. Tarascon, Impedance Study of the Li°/Electrolyte Interface Upon Cycling, *Solid State Ionics* 135 (2000) 213-221.

[52] Q. C. Zhuang, J. M. Xu, X. Y. Fan, G. Z. Wei, Q. F. Dong, Y. X. Jiang, L. Huang, and S. Sun, $LiCoO_2$ Electrode/Electrolyte Interface of Li-Ion Batteries Investigated by Electrochemical Impedance Spectroscopy, *Science in China Series B-Chemistry* 50 (2007) 776-783.

[53] R. Chen, T. Zhao, J. Lu, F. Wu, L. Li, J. Chen, G. Tan, Y. Ye, and K. Amine, Graphene-Based Three-Dimensional Hierarchical Sandwich-Type Architecture for High-Performance Li/S Batteries, *Nano Letters* 13 (2013) 4642–4649.

[54] M. Shi, S. Zhang, Y. Jiang, Z. Jiang, L. Zhang, J. Chang, T. Wei, and Z. Fan, Sandwiching Sulfur into the Dents Between N, O Co-Doped Graphene Layered Blocks with Strong Physicochemical Confinements for Stable and High-Rate Li–S Batteries, *Micro & Nano Letters* 12 (2020) 146.

[55] W. Wang, J. Zhou, Z. Wang, L. Zhao, P. Li, Y. Yang, C. Yang, H. Huang, and S. Guo, Short-Range Order in Mesoporous Carbon Boosts Potassium-Ion Battery Performance, *Advanced Energy Materials* 8 (2018) 1701648.

[56] R. Tian, S. H. Park, P. J. King, G. Cunningham, J. Coelho, V. Nicolosi, and J. N. Coleman, Quantifying the Factors Limiting Rate Performance in Battery Electrodes, *Nature Communications* 10 (2019) 1933.

[57] L. Sun, W. Kong, Y. Jiang, H. Wu, K. Jiang, J. Wang, and S. Fan, Super-aligned carbon nanotube/graphene hybrid materials as a framework for sulfur cathodes in high performance lithium sulfur batteries, *Journal of Materials Chemistry A* 3 (2015) 5305.

[58] C. Tang, Q. Zhang, M.Q. Zhao, J.Q. Huang, X.B. Cheng, G.L. Tian, H.J. Peng, and F. Wei, Nitrogen-Doped Aligned Carbon Nanotube/Graphene Sandwiches: Facile Catalytic Growth on Bifunctional Natural Catalysts and Their Applications as Scaffolds for High-Rate Lithium-Sulfur Batteries, *Advanced Materials* 26 (2014) 6100-6105.

[59] Y. Wu, C. Xu, J. Guo, Q. Su, G. Du, and J. Zhang, Enhanced electrochemical performance by wrapping graphene on carbon nanotube/sulfur composites for rechargeable lithium–sulfur batteries, *Materials Letters* 137 (2014) 277-280.

[60] X. Yan, H. Zhang, M. Huang, W. Jia, Y. Jiang, T. Chen, and M. Qu, Micro/nano-structure construct of carbon fibers reinforced graphene/CNT matrix composites for Li-S batteries, *Diamond and Related Materials* 123 (2022) 108888.

[61] Z. Guo, H. Nie, Z. Yang, W. Hua, C. Ruan, D. Chan, M. Ge, X. Chen, and S. Huang, 3D CNTs/Graphene-S-Al_3Ni_2 Cathodes for High-Sulfur-Loading and Long-Life Lithium–Sulfur Batteries, *Advanced Science* 5 (2018) 1800026.

[62] A. Doñoro, A. Muñoz-Mauricio, and V. Etacheri, High-Performance Lithium Sulfur Batteries Based on Multidimensional Graphene-CNT-Nanosulfur Hybrid Cathodes, *Batteries* 7 (2021) 26.

[63] M. Wei, H. Zhu, P. Zhai, L. An, H. Geng, S. Xu, and T. Zhang, Nano-sulfur confined in a 3D carbon nanotube/graphene network as a free-standing cathode for high-performance Li–S batteries, *Nanoscale Advances* 4 (2022) 4809-4818.

[64] J. He, Y. Chen, P. Li, F. Fu, Z. Wang, and W. Zhang, Three-dimensional CNT/graphene–sulfur hybrid sponges with high sulfur loading as superior-capacity cathodes for lithium–sulfur batteries, *Journal of Materials Chemistry A* 36 (2015) 18605-18610.

[65] A. Wang, S. Kadam, H. Li, S. Shi, and Y. Qi, Review on Modeling of the Anode Solid Electrolyte Interphase (SEI) for Lithium-Ion Batteries, *npj Computational Materials* 4 (2018) 15.

Chapter 6. Summary and Future Work

In this dissertation, two types of waste carbon-based materials, paper waste and spent Li-ion battery anodes, were recycled and/or upcycled into high value-added carbon materials for energy storage and decarbonization. Based on the chosen waste materials and the depth of the study, the research thrusts of this dissertation were placed on the following aspects: (1) recycled cellulose fibers (CFs) from paper waste for energy storage; (2) mechanism study of recycled CFs in Li-S batteries; (3) use of recycled CFs for carbon dioxide adsorption; (4) upcycled CNT/graphene hybrid from end-of-life batteries for energy storage. The completion of these research activities brought insights into deriving valuable carbon materials from waste and explored possible applications for energy storage and carbon neutrality, paving the way towards a waste-to-wealth society.

6.1 Summary of Contribution and Significance

Paper waste as one of the most commonly seen carbon waste is usually recycled for a second life, yet the CFs within the paper waste may hold the key to addressing both energy and environmental issues. In Chapters 2, 3, and 4, CFs from paper waste played a major role in energy storage and potentially in decarbonization. The working mechanism of the CFs in Li-S batteries was investigated to further provide guidance on using CFs in energy storage. Another impending challenge is the expanding Li-ion battery market-induced end-of-life battery disposal problem. In Chapter 5, spent Li-ion battery anodes were chosen as another carbon waste to be recycled and upcycled into graphene for energy storage use.

Specifically, in Chapter 2, CFs were successfully extracted from paper waste experimentally via a simple alkaline treatment. The CFs were carefully washed and then coated on commercial polypropylene (PP) separators. The separators were inserted to replace the commercial separators in Li-S batteries as the functional groups on CFs were expected to lose their H-ion during battery operation to prevent the polysulfide shuttle effect and improve Li-ion's even distribution when traveling. By comparing with the battery without CFs, as expected, the CF-enabled battery performance and the post-failure analysis jointly evidenced the positive functions of CFs in Li-S batteries. As a result, the Li-S battery with the recycled paper CF-coated separator exhibited a lifespan of over 800 cycles with a capacity retention rate of 71.69 % and nearly no capacity decay after the

initial formation cycles, which is much better than the battery without the CF-coated separator. The finding demonstrates that renewably-produced, cellulose fiber-coated polypropylene separators can simultaneously reduce the shuttle effect and degradation of lithium, paving the way towards commercially viable and environmentally-friendly lithium-sulfur batteries.

To further study the working mechanism of CFs in Li-S batteries, in Chapter 3, a series of computational studies was conducted. The CF function towards Li ions distribution and polysulfides' repulsion was separately discussed. Molecular dynamic (MD) simulation unveiled that CF could slow the polysulfides down by generating a repulsive force to them, whereas PP did not show such behavior. The simulation also revealed that CF could efficiently redirect Li ions such that the distribution of the Li ions was more even, which prevented the fast growth of dendritic Li. The CF losing H-ion during battery operation was also proven by the MD study. More specifically, it was found in the MD simulations that CF lost a couple of H^+ when an electric field was applied to the simulation box. Lastly, a series of density functional theory calculations were performed to estimate the interacting energy between the ions and the CF, which was much larger than that between the ions and the PP. The findings in this chapter exhibited the working mechanism of the CF in the Li-S battery, shedding light to the following research that uses CF in energy storage.

The previous two chapters have evidenced that the CF from paper waste possesses a large potential in the energy field, which brought curiosity if this material had other potential. In Chapter 4, the potential of the CF in decarbonization was explored using computational approaches. It was revealed by a series of MD simulations that the CF was able to adsorb CO_2 in a mixed gas condition. The CO_2/N_2 selectivity of the CF was predicted to be much higher than activated carbon (AC), one of the most commonly used CO_2 adsorbents. Meanwhile, the most effective working temperature and a tolerable velocity of gas flow were also estimated by the simulation. The findings added more possibilities of using the CF from paper waste and the guidance of the most promising working conditions.

Apart from paper waste recycling, many other carbon-based waste materials also are worth studying. Due to the expanding Li-ion battery market, end-of-life Li-ion batteries make a perfect target to recycle and the carbon material in it is graphite in their anodes. In

Chapter 5, a novel recycling process was designed and performed for graphite anodes. To further upgrade the material, the recycled graphite was used to produce graphene via shear mixing. Graphene is usually not able to be directly used in Li-S batteries, therefore, a green approach to grow CNTs on graphene was successfully conducted to prepare a CNT/graphene hybrid for Li-S batteries. When being used in a Li-S battery cathode, the graphene provided a highly conductive network while the CNTs enabled high sulfur loading and volume buffering, rendering the battery with high capacity, high stability, and long lifespan. The CNT/graphene constructed battery exhibited longevity of over 1,500 cycles with a capacity fading rate of 0.042% per cycle and a steady Coulombic efficiency of over 97%. The all-green CNT/graphene hybrids present new pathways to upcycling batteries to second life.

6.2 Recommendations for Future Research

While this dissertation has investigated the two carbon-based waste material recycling and their applications in energy storage and potentially decarbonization, it also brings questions and opportunities for future research. Here, I will summarize several potential research opportunities following the research after this dissertation.

For material-based research, paper waste and spent battery anodes are worth further exploration. Like other biomass materials, paper waste should also be able to be converted into more valuable carbon materials. Nowadays, the graphene market is growing yet most graphene production lines use non-renewable sources. Biomass, including paper waste, can be a promising feedstock for graphene manufacturing, which can be a future research goal to accomplish. The spent battery anodes originally use battery-grade graphite, which has the highest quality. Studying the failure reason of this material in Li-ion batteries for better recycling in the future can serve as a viable topic and is already slowly ongoing. Most studies on recycling anode graphite focus on purification, yet some applications can take advantage of the impurities within the battery anodes, which are also worth investigating. Moreover, searching for more recyclable carbon waste is tedious but meaningful for a sustainable and high-tech society in the future. Following the discovery of recyclable carbon waste categories, a universal recycling method should also be proposed in the future.

For application-based research, although an improved Li-S energy storage performance was achieved by inserting CFs or applying CNT/graphene hybrid to the

batteries, it remains challenging to accelerate Li-S batteries to the market mostly due to the challenges this dissertation was trying to address. Inserting CFs in Li-S batteries can prevent both polysulfide shuttling and dendritic Li growth to some degree, yet it adds weight and thickness to the system, which is not favorable for commercialization. A lighter and thinner form of the CFs from paper waste can be explored in the future, such as cellulose nanofibrils. On the other hand, the CNT/graphene hybrid was able to accommodate sulfur expansion while providing high electric conductivity, however, it did not provide much help with the polysulfide shuttling and dendritic Li growth. The functionalization of the CNT/graphene hybrid is a promising route in the future to further improving the Li-S battery performance by providing extra functions onto polysulfides and Li-ions while keeping current advantages. Refining the preparation method of the CNT/graphene can be another research goal in the future to push up the production rate of this material, such as a roll-to-roll method. As for the decarbonization application of the CFs, preliminary guidance is given in this dissertation, therefore, finding a way to realize it can be a viable study in the future.